Universidade de Aveiro Departamento de Eletrónica, Telecomunicações e Informática
2015

João Carlos de Melo Ferreira

Amplificadores de Fibra em Redes Óticas Transparentes e Dinâmicas

Fiber Amplifiers in Transparent and Dynamic Optical Networks

Universidade de Aveiro Departamento de Eletrónica, Telecomunicações e Informática
2015

João Carlos de Melo Ferreira

Amplificadores de Fibra em Redes Óticas Transparentes e Dinâmicas

Fiber Amplifiers in Transparent and Dynamic Optical Networks

Tese apresentada à Universidade de Aveiro para cumprimento dos requisitos necessários à obtenção do grau de Doutor em Engenharia Eletrotécnica, realizada sob a orientação científica do Doutor Armando Humberto Moreira Nolasco Pinto, Professor Associado do Departamento de Eletrónica, Telecomunicações e Informática da Universidade de Aveiro, coorientação científica do Doutor Paulo Miguel Nepomuceno Pereira Monteiro, Professor Associado do Departamento de Eletrónica, Telecomunicações e Informática da Universidade de Aveiro e coorientação empresarial do Doutor Daniel Diogo Trindade Fonseca, Doutor em Engenharia Eletrotécnica e de Computadores pelo Instituto Superior Técnico e arquiteto de sistemas na Coriant Portugal.

Apoio financeiro da Fundação para a Ciência e a Tecnologia - FCT através da bolsa de investigação com a referência: SFRH / BDE / 51095 / 2010, comparticipada pelo Fundo Social Europeu - FSE no âmbito do Programa Operacional Potencial Humano - POPH do QREN, e por fundos nacionais do Ministério da Educação e Ciência - MEC.

o júri / the jury

presidente / president

Doutor Luís Filipe Pinheiro de Castro,
Professor Catedrático do Departamento de Matemática da Universidade de Aveiro

vogais / examiners committee

Doutor Henrique José Almeida da Silva,
Professor Associado da Faculdade de Ciências e Tecnologia da Universidade de Coimbra

Doutor Adolfo da Visitação Tregeira Cartaxo,
Professor Associado do Instituto Superior Técnico da Universidade de Lisboa

Doutor Henrique Manuel de Castro Faria Salgado,
Professor Associado da Faculdade de Engenharia da Universidade do Porto

Doutor António Luís Jesus Teixeira,
Professor Associado do Departamento de Eletrónica, Telecomunicações e Informática da Universidade de Aveiro

Doutor Armando Humberto Moreira Nolasco Pinto
Professor Associado do Departamento de Eletrónica, Telecomunicações e Informática da Universidade de Aveiro (Orientador)

agradecimentos / acknowledgements

O trabalho apresentado nesta tese foi levado a bom porto devido ao apoio e contributo de várias pessoas e entidades a quem gostaria de agradecer:

Ao Professor Doutor Armando Humberto Moreira Nolasco Pinto o facto de ter aceitado orientar-me cientificamente neste Doutoramento. Agradeço o apoio dado na análise, discussão e interpretação dos vários resultados obtidos ao longo deste doutoramento e pelo apoio dado na elaboração desta tese.

Ao Professor Doutor Paulo Monteiro e ao Doutor Daniel Fonseca que, nas posições de coorientador científico e coorientador empresarial, respetivamente, sempre garantiram as condições necessárias para que o trabalho fosse efetuado com sucesso, sem nunca descurar o apoio científico. Queria também agradecer ao Doutor Lutz Rapp pela sua disponibilidade e pelas inúmeras discussões científicas realizadas.

Aos meus colegas e amigos do grupo de comunicações óticas do Instituto de Telecomunicações de Aveiro e da Coriant Portugal, que sempre promoveram um ambiente de trabalho salutar e de amizade.

À Fundação para a Ciência e a Tecnologia e à Coriant Portugal pelo fundamental suporte financeiro através da bolsa de doutoramento em empresa SFRH / BDE / 51095 / 2010, e pela oportunidade de trabalhar em ambiente empresarial.

Quero terminar agradecendo à minha família e amigos por todo o apoio e paciência que tiveram para comigo.

Nós temos cinco sentidos:
são dois pares e meio de asas.

- Como quereis o equilíbrio?

David Mourão-Ferreira

palavras-chave

Redes óticas transparentes, Multiplexação por divisão de comprimento de onda, Amplificador de Raman, Espalhamento de Raman, Efeito transiente, Amplificador de fibra dopada com érbio, *Spectal hole burning* (SHB), *Site dependent pumping* (SDP).

resumo

Nesta tese é feito um estudo sobre amplificadores de fibra ótica no contexto de redes óticas transparentes e dinâmicas.

Propomos e validamos um modelo simplificado para estimar o perfil do ganho e do ruído de emissão espontânea amplificada (ASE), para amplificadores de Raman (RFAs) contra propagantes. O modelo proposto requer baixos recursos computacionais e é adequado para ser usado em ferramentas de planeamento da rede. Com base no modelo proposto, apresentamos também um algoritmo com requisitos computacionais baixos para desenhar RFAs contra propagantes com ganho constante para a banda C estendida.

Verificamos experimentalmente que um RFA contra propagante com reflexo da potência da bomba devido à adição/remoção de canais apresenta uma resposta transiente mais elevada, quando comparado com um RFA contra propagante convencional. Isto torna esta configuração inadequada para redes óticas transparentes e dinâmicas. Para mitigar a resposta transitória devido à adição/remoção de canais, um sistema de controlo do ganho baseado na monitorização da potência da bomba refletida é proposto e validado numérica e experimentalmente. Seguindo esta abordagem, um RFA contra propagante eficiente e de baixo custo adequado para redes óticas dinâmicas é proposto.

A dependência da resposta dinâmica dos amplificadores de fibra dopada com érbio (EDFAs) em função do comprimento de onda da bomba, da potência da bomba e da temperatura devido ao *spectral hole burning* (SHB) e *site dependent pumping* (SDP) é investigada experimentalmente. Nos resultados obtidos é mostrada a dependência da resposta dinâmica em função do comprimento de onda da bomba, para amplificadores bombeados em torno de 1480 nm. Para explicar esta dependência, o impacto do SDP no desempenho de EDFAs bombeados em comprimentos de onda em torno de 1480 nm é investigado, tanto experimental como numericamente. Como resultado, um modelo mais completo, incorporando o efeito SDP para EDFAs de dois níveis é derivado e validado experimentalmente.

keywords Transparent optical networks, Wavelength division multiplexing (WDM), Raman fiber amplifiers (RFAs), Raman scattering, Transient effect, Erbium-doped fiber amplifiers (EDFAs), Spectral hole burning (SHB), Site dependent pumping (SDP).

abstract

In this thesis a study of optical fiber amplifiers in the context of transparent and dynamic optical networks is performed.

We propose and validate a simplified model to estimate the gain profile and amplified spontaneous emission (ASE) noise of broadband counter-pumped Raman fiber amplifiers (RFAs). The proposed model requires very low computational resources and it is suitable to be used in network planning tools. Based on the proposed model, we also present an algorithm to design flat gain counter-pumped RFAs for the extended C-band with low computational requirements.

We experimentally verify that the pump-reflecting RFA presents a higher transient response due to channels add/drop, when compared to the conventional counter-pumped RFA. This makes this amplifier configuration unsuitable for transparent and dynamic optical networks. To mitigate the transient response due to channel add/drop, a pump-controlled gain-locked system based on the monitorization of the reflected pump power is proposed and validated numerically and experimentally. Following this approach, an efficient low-cost RFA suitable for dynamic optical networks is proposed.

The dependence of the dynamical response of erbium-doped fiber amplifiers (EDFAs) on the pump wavelength, pump power, and temperature due to spectral hole burning (SHB) and site dependent pumping (SDP) is experimentally investigated. A dependence of the dynamic response on the pump wavelength, for amplifiers pumped around 1480 nm, is shown. In order to explain this dependence, the impact of SDP on the performance of EDFAs pumped at wavelengths around 1480 nm is investigated, both experimentally and numerically. As a result, an improved model incorporating the SDP effect for two-level EDFAs is derived and experimentally validated.
.

Contents

List of Acronyms

AOGC	All–Optical–Gain–Clamped
APA	Average Power Analysis
ASE	Amplified Spontaneous Emission
AWG	Arrayed Waveguide Grating
CapEx	Capital Expenditures
CUPM	Customized Undepleted Pump Model
CW	Continuous Wave
DCF	Dispersion Compensating Fiber
DNM	Detailed Numerical Model
DSF	Dispersion Shifted Fiber
DWDM	Dense Wavelength–Division Multiplexing
EDF	Erbium–Doped Fiber
EDFA	Erbium–Doped Fiber Amplifier
ESA	Excited–State Absorption
FBG	Fiber–Bragg Grating
FMR	Fiber–Mirror Reflector
GA	Genetic Algorithm
ICT	Information and Communication Technology
ISO	Optical Isolator
LEAF	Large Effective Area Fiber

MAE	Mean Absolute Error
MUX	Optical Multiplexer
MSE	Mean Squared Error
OEO	Optical–Electrical–Optical
OpEx	Operational Expenditures
OSA	Optical Spectrum Analyzer
OSC	Oscilloscope
OSNR	Optical Signal–to–Noise Ratio
PD	Proportional–Derivative
PHB	Polarization Hole Burning
RFA	Raman Fiber Amplifier
RIN	Relative Intensity Noise
RK4	Fourth-Order Runge-Kutta
ROADM	Reconfigurable Optical Add/Drop Multiplexer
ROPA	Remote Optically Pumped Amplifier
SDN	Software Defined Networks
SDP	Site Dependent Pumping
SHB	Spectral Hole Burning
SRS	Stimulated Raman Scattering
SSMF	Standard Single Mode Fiber
UPM	Undepleted Pump Model
VOA	Variable Optical Attenuator
WAE	Weighted–By Analytic Expression
WBC	Weighted–By Comparison
WDM	Wavelength–Division Multiplexing

List of Symbols

Roman

A_{eff}	Effective area of the fiber
c	Speed of light in vacuum
d	Section index
E_1, E_2, E_3	Energy of levels one, two and three
g_R	Raman gain efficiency of the fiber
g_r	Raman gain coefficient
G_s	On/Off gain of the signal s
h	Planck's constant
$\bar{I}$	Average photon flux divided by the saturation parameter
$\bar{I}_l^{980}$	Average photon flux divided by the saturation parameter of the pump centered at 980 nm
i	Ions sub–ensemble index
k, j, s	Signal index
k_B	Boltzmann's constant
K_{eff}	Polarization factor between pumps and Stokes signals
L	Fiber length
L_{eff}	Effective length
M	Total number of signals
m	Polarization degrees of freedom
N_1, N_2, N_3	Atomic population densities of laser system levels one, two, and three
n_3	Variations on the third–level
n_2	Variations on the second–level
$\bar{N_3}$	Average population probability of the third–level
$N_{3,i}$	Population probability for the third–level for the ion sub–ensemble i
$\bar{N_2}$	Average population probability of the second–level
$N_{2,i}$	Population probability for the second–level for the ion sub–ensemble i
N_{tot}	Total number of wavelengths in the amplifiers
n	Time index
$n_{sp}^{\pm}$	Noise generation
N_p	Total number of pump wavelengths
N_s	Total number of signal wavelengths
N_{ASE}	Total number of ASE noise wavelengths
P^+, P^-	Optical power in the forward or backward direction
$P_{in}^{\pm}$	Input power
$P_{out}^{\pm}$	Output power

P_p	Pump power
P_s	Signal power
$P_{s,OFF}$	Signal output power without amplification
$P_{s,ON}$	Signal output power with amplification
S	Total number of fiber sections
S_1	Continuous wave signal
S_2	Modulated signal
T	Absolute temperature
t	Time instant
u_k	Propagation direction
v_g	Group velocity
z	Coordinate along the amplifier

Greek

α	Attenuation coefficient
α_s	Fiber attenuation at the signal wavelength s
Γ_{14xx}	Correlation matrix between the pump wavelengths around 1480 nm and signals wavelengths
Γ_{9xx}	Correlation matrix between the pump wavelengths around 980 nm and signals wavelengths
Γ_s	Correlation matrix between signals
γ	Rayleigh backscattering coefficient
$\Delta\nu$	Effective noise bandwidth
Δt	Time interval
Δz	Length of the fiber section
$\Delta N_{3,i}$	Variation of the population probability of the third–level
$\Delta N_{2,i}$	Variation of the population probability of the second–level
ν, ς	Optical channels frequencies
σ_i^a	Giles parameters for the absorption of ion sub–ensemble i
$\bar{\sigma}^a$	Average Giles parameters for the absorption of the fiber
σ_i^e	Giles parameters for the emission of ion sub–ensemble i
$\bar{\sigma}^e$	Average Giles parameters for the emission of the fiber
$\bar{\sigma}^{\mathrm{ESA}}$	ESA absorption
τ_2	Lifetime of the second energy level
τ_3	Lifetime of the third energy level
ξ	Deviation function
ζ	Saturation parameter

List of Figures

List of Tables

Chapter 1

Introduction

Fiber optic communication networks revolutionized the telecommunications industry. The use of optical fiber cables enhances the transmission distance between optical–electrical–optical (OEO) regenerators and enables much higher data rates compared to copper or wireless based networks, due to the useful transmission bandwidth of the optical fiber. The transmission bandwidth of the fiber is usually located between 1520 nm and 1570 nm, due to a reduced fiber attenuation at these wavelengths. Optical fiber amplifiers, such as erbium–doped fiber amplifiers (EDFAs) and Raman fiber amplifiers (RFAs) [1, 2], are a key technology to enable long transmission distances without OEO regeneration [3, 4]. However, due to the fact that signals may have to travel distances up to a few thousands of kilometers and through several cascaded amplifiers, optical fiber amplifiers have to be carefully designed, in order to provide low noise [5]. Optical fiber amplifiers are independent of the modulation format and allow the simultaneous amplification of several optical signals [6]. In a transparent optical network, these optical signals are transported entirely in the optical domain, via all–optical channels called lightpaths, thus avoiding some disadvantages commonly attributed to OEO regenerators, such as high cost, and limited upgradeability and scalability of the network [7–9]. With the development and implementation of reconfigurable optical add/drop multiplexers (ROADMs), optical networks became dynamic networks, allowing the add/drop of channels at the network node. Despite the advantages in terms of network management, this feature raises new challenges on the amplifier design and construction.

This chapter is organized as follows. In Section 1.1, it is given an overview of key concepts regarding transparent and dynamic optical networks. In Section 1.2, the motivation for this thesis is explained. Following, in Section 1.3, the objectives of this thesis are presented. In Section 1.4, the thesis outline is described. The main achievements of this thesis are presented in Section 1.5. In Section 1.6, the publications in the context of this thesis are listed.

1.1 Transparent and Dynamic Optical Networks

Comparing the different fiber optic communication technologies available, transparent networks based on wavelength–division multiplexing (WDM) are considered to be the most promising solution to support the exponential growth of required bandwidth at relatively low cost [9, 10]. A transparent optical network is composed by optical fiber links carrying a large number of WDM channels. Each channel can be modulated at a very high data rate [11], and the amplification of WDM channels is done using optical fiber amplifiers. In a transparent optical network, the network nodes do not need to process every channel. Therefore, the node can be transparent to the content of the channel, thus allowing the coexistence of different technologies, such as modulation formats [9]. For this reason, an increase in the number of channels, or in the channel data rate, will not have a significant impact on the cost of the network, which improves the scalability and upgradeability of the network [8]. On the other hand, due to the reduction of the OEO devices for optical channels regeneration at the network nodes, the reach of the system is limited by the signal quality [12, 13].

The combination of reconfigurable systems such as ROADM [8], tunable lasers and receivers, and automatic processes, such as software defined Networks (SDN) [14], allows the optical network to become dynamic, improving the capacity to respond to the variation of traffic demands for emerging services. The inclusion of these systems in optical networks implies the introduction of additional or more sophisticated devices to manage the optical layer and the lightpath routing. Nevertheless, it was shown that transparency can lead to a reduction of the capital expenditures (CapEx) [10]. As an example, it is possible to decrease the network cost by sharing expensive resources of the optical network, such as optical regenerators. In a transparent and dynamic optical network, it is possible to automatically assure the survivability of the network if one or more failures occur on the optical layer. In a near future, it will be possible to change the network configuration without any human interventions and, consequently, reduce its operational expenditures (OpEx) [10].

Enabled by the all–optical transmission and the development and implementation of ROADMs at the network nodes, transparent and dynamic optical networks can remotely reroute optical lightpaths. As a result of this feature, frequent channels add/drop occur at the network nodes, changing the number of lightpaths at a given transmission link over time. Due to these add/drop events and to the non–ideal dynamic properties of optical fiber amplifiers, gain variations can be transfered to other wavelengths that are not directly affected by the switching operations [15, 16]. Thus, even surviving channels, i.e. channels not involved directly in the switching operations, can suffer from gain fluctuations, also known as transient effects, at the output of the amplifier stage. This fact can lead to a degradation of the signal quality at the receiver side [17]. In addition, gain fluctuations can accumulate and become critical in a cascade of amplifiers [18]. Therefore, even a small gain variation can result in significant power changes at the receivers [19], which can have influence on the system performance [20]. The impact of the transient on signal quality has resulted in the development of several mitigation techniques [21–24].

1.2 Motivation

The main motivation of this thesis is to analyze and improve models for optical fiber amplifiers in optical transmission systems in terms of accuracy and computational speed. This is an interesting topic from a scientific and a commercial point of view, since optical amplification is one of the key enablers of long haul transmission. In fact, this thesis was done in collaboration with a hosting company focused on the development of optical communication systems.

Transparent and dynamic optical networks require accurate planning tools to optimize network resources and routing of the lightpaths in real time. In order to provide accurate results, the network planning tool needs to correctly describe the signal degradation [25]. However, system modeling is not an easy task since an accurate description of the system can imply a huge computational effort. This is not compatible with a planning tool that needs to provide results in a short time. For this reason, simplified models, which trade off accuracy for computation speed, need to be developed and implemented. In one of the official planning tools for the physical layer from the hosting company, when considering the use of RFAs in the transmission system, the models to estimate the gain and noise figure are based on lookup tables for each fiber type, which were created based on experimental validation. However, the output signal power and optical signal–to–noise ratio (OSNR) obtained with this method may present some inaccuracies due to the fact that the gain of the amplifier is not entirely flat, and depends on several parameters, like pump and signal powers and fiber type. Moreover, connectors and splices also change the input pump power, which can affect the gain of the amplifier. Therefore, as the number of transmission links with RFAs increases, it is necessary to develop and implement high accuracy models requiring low computational effort for the gain and amplified spontaneous emission (ASE) noise, in order to provide reliable results in a short time interval.

Given the extensively growing demand for capacity, the amount of electrical power required to operate optical networks cannot be overlooked. For this reason, future communication networks should have the ability to support an enormous amount of bandwidth in an energy efficient way. The information and communication technology (ICT) sector already consumes around 8% of the total worldwide electrical power [26]. Considering that optical networks play an important role in the ICT, it is understandable that their power consumption cannot be ignored. The reduction of power consumption in optical networks can be addressed at different levels such as network, applications, transmission, and components [26, 27]. When considering RFAs, there are some solutions to increase the power consumption efficiency, such as reflecting the pump power back into the amplifier [28, 29] or hybrid amplification. However, those solutions have to be compatible with dynamic networks, meaning that the dynamic response due to channel add/drop has to be similar or smaller than the conventional configuration. Therefore, a thorough understanding of the transient effects and efficient mitigation techniques is required, in order to minimize the transient response of an amplifier or an amplifier stage in an add/drop event.

In a WDM transmission link amplified with EDFAs, power fluctuations of the surviving channels due to channel add/drops will occur at the output of the EDFAs. These power fluctuations arise due to total input power variation [30, 31] and are enhanced due to the presence of spectral hole burning (SHB) [32] and site dependent pumping (SDP) [33, 34]. The SHB and SDP are rather small effects in a single EDFA, however, they can produce a significant signal power fluctuation at the end of the transmission link, when cascaded in several EDFAs. In fact, some tests performed at the hosting company showed that this effect is quite complex and difficult to predict. Moreover, these dynamic effects cannot be easily mitigated by the control systems currently implemented in amplifiers or in the network. Thus, in order to predict and optimize the overall system performance under different operational scenarios, numerical models used to describe the EDFAs need to include even second order effects, such as the SHB and SDP effects.

1.3 Objectives

The work will be carried out targeting the following objectives:

1. To analyze and develop computational efficient models to describe long haul WDM transmission systems with counter–pumped RFAs. The simplified models should be able to estimate the gain and the ASE noise when considering transmission on the extended C–band with up to, at least, four pumps;

2. To investigate and propose a solution to increase the efficiency of RFAs suitable for use on transparent and dynamic optical networks. To study designs that allow reducing the pump power, while still achieving the same gain as the conventional configurations. In addition, to evaluate the transient response when a power variation occurs, as well as to study and propose low cost solutions to mitigate and control the transient response of the RFA;

3. To infer and identify the possible sources of gain fluctuations in EDFAs when channel add/drop occurs. Moreover, to evaluate the impact of input channel spectrum allocation on the dynamic response of the EDFA. To propose new designs to mitigate the gain fluctuations due to SHB and SDP.

1.4 Thesis Outline

The thesis is divided into six Chapters, organized as follows:

- Chapter 2 introduces the RFA and the EDFA, and presents the amplifier models used in this thesis. First, the main advantages and disadvantages of the RFA and EDFA, as well as the configurations commonly used, are presented and discussed. Afterwards, regarding the RFA, the principle of operation and propagation equations, as well as the numerical models implemented for the steady–state and for the dynamic regime are presented. Following, experimental validations of the implemented models for the steady–state and dynamic regime models are presented and discussed. Regarding the EDFA, the principle of operation and the inhomogeneous gain broadening effect is discussed. The mathematical models for the two–level system and three–level system derived from the fundamental equations considering statistical variations are presented. The implemented mathematical model for the three–level amplifier is validated using an experimental setup specifically designed to isolate the SHB and the SDP effects. Finally, the dynamic response of an EDFA pumped around 980 nm as function of the pump wavelength and input channel spectrum allocation is assessed.

- Chapter 3 presents a simplified model for the gain and ASE noise of the RFA, suitable for use with multiple pumps. To achieve this, the undepleted pump model (UPM) is customized with the introduction of two new parameters, that account for the pump–to–pump interactions. These parameters can be adjusted based on experimental measurements, simulation results, as well as on analytical expressions. The model is validated with experimental results for different number of pumps. Using these two parameters, an accurate black–box model for the gain and ASE noise profile is obtained without increasing the computational effort of the UPM. Furthermore, it is also discussed and numerically validated the usability of the proposed model for estimating the OSNR in a transmission link with WDM signals, for different distances and fiber types. Finally, an efficient algorithm to design RFAs with low computational requirements is presented. In the proposed algorithm, the developed simplified model is used for estimating the amplifier gain, instead of a detailed numerical model (DNM). A genetic algorithm (GA) is implemented to search for the quasi–optimum solution that minimizes the gain ripple.

- Chapter 4 proposes an energy efficient counter–pumped RFA suitable for use in transparent and dynamic optical networks, based on the reflection of the unused pump power back into the transmission fiber. It is experimentally demonstrated that reflecting the pump power back into the transmission fiber increases the amplifier efficiency. However, it also increases the dynamic response of the amplifier. Afterwards, the impact of the pump power fluctuations on the surviving channels transient response is analyzed, considering different pumping configurations, pumping powers, and fiber lengths. Finally, in order to mitigate and control the transient response, a new pump–controlled gain–locked system that takes advantage of the amplifier configuration is proposed and validated both numerically and experimentally.

- Chapter 5 analyzes the impact of changing the input signal spectrum at the input of the EDFA. Initially, experimental measurements are performed to understand the dependence of the dynamic response with the pump wavelength, power and temperature, in the context of input signal spectrum variation. It is shown that, when pumping within the 1480 nm range, the dynamic response of the amplifier is sensitive to pump wavelength variations. Afterwards, a model incorporating the SDP effect in a two–level model of an EDFA is derived and experimentally validated. With the proposed model, the dependence of the gain on the pump wavelength for wavelengths around 1480 nm is described. Finally, the behavior of SHB and SDP in an EDFA with ideal gain control for different pump wavelengths around 980 nm and different spectral allocation of input channels is investigated numerically.

- Chapter 6 summarizes the main results obtained in this thesis, and presents suggestions for future work.

This thesis comprises also a List of Acronyms, a List of Symbols, a List of Figures, and a List of Tables.

1.5 Main Contributions

In the author's opinion, the main achievements reported in this thesis are:

- Proposal and validation of a new simplified model that estimates the gain and ASE noise at the end of the transmission link, when using a counter–pumped RFA with several pumps. Since this model increases the accuracy of the estimation when compared to the traditional look up tables, it allows a better optimization of the optical network without a significant increase of the processing time of the tools or routing algorithms. This work was presented to the scientific community essentially through a publication in the IEEE/OSA Journal of Optical Communications and Networking [35]. In addition to the above mentioned publication, the proposed model was incorporated in a network planning software tool supported by the hosting company.

- Investigation of the dynamic response of an energy efficient RFA configuration. This work shows that the pump–reflecting RFA configuration has a worse response to channel add/drop compared to the conventional counter–pumped RFA. Additionally, it is proposed and validated numerically and experimentally a low cost mitigation technique to control the dynamic response due to channel add/drop. With the proposed control system it is possible to increase the efficiency of the RFA without compromising the dynamic regime, thus allowing the implementation of an efficient low cost RFA suitable for use in dynamic optical networks. This work was published in an article in the Journal of Fiber and Integrated Optics [36] and a patent was granted for the mitigation technique [37].

- Experimental assessment of the EDFA dynamic response dependence on pump wavelength, pump power, and temperature for amplifiers pumped around 1480 nm and 980 nm. These results show that even when mitigating the gain fluctuations caused by input power variations, a gain fluctuation will occur due to the variation of spectral allocation of input signals. It is also shown that gain deviations on EDFAs pumped around 1480 nm depend on the pump wavelength. Following, a model which is able to explain the gain deviations dependence on the pump wavelength around 1480 nm by incorporating the SDP effect in a two–level model of an EDFA is derived and proposed. This work was published in two letters in IEEE Photonics Technology Letters [38, 39] and in an article in IEEE/OSA Journal of Lightwave Technology [40].

1.6 List of Publications and Other Achievements

1.6.1 Journal Articles

- **J. Ferreira**, D. Fonseca, P. Monteiro, A. Pinto, L. Rapp, "Site dependent pumping effect on two–level EDFAs," *IEEE/OSA Journal of Ligthwave Technology*, vol. 33, No. 2, pp. 285–292, Jan. 2015.
- **J. Ferreira**, R. Nogueira, P. Monteiro, A. Pinto, "Weighted undepleted pump model for broadband counter–pumped Raman fiber amplifiers," *IEEE/OSA Journal of Optical Communications and Networking*, Vol. 4, No. 8, pp. 595 – 602, Aug. 2012.
- **J. Ferreira** and L. Rapp, "Dynamics of spectral hole burning in EDFAs: dependence on temperature," *IEEE Photonics Technology Letters*, Vol. 24, No. 1, pp. 67 – 69, Jan. 2012.
- L. Rapp and **J. Ferreira**, "Dynamics of spectral hole burning in EDFAs: dependency on pump wavelength and pump power," *IEEE Photonics Technology Letters*, vol. 22, no.6, pp. 1256–1258, Aug. 2010.
- **J. Ferreira**, M. Fugihara and A. Pinto, "Transient response and control of pump–reflecting Raman fiber amplifiers," *Fiber and Integrated Optics*, vol. 29, no. 1, pp. 44–61, Jan. 2010.
- B. Neto, **J. Ferreira**, N. Wada, A. Pinto and P. André, "Evaluation of the effect of channel add/drop impact on power transients on the performance of a

10 GB/s DWDM transmission system with hybrid EDFA/Raman amplification," *Microwave and Optical Technology Letters*, vol. 52, no. 6, pp. 1225–1228, Jun. 2010.

- B. Neto, C. Reis, R. P. Dionísio, **J. Ferreira**, J. A. Lazaro, G. Tosi–Belef, A. N. Pinto, R. Nogueira, A. Teixeira, J. Prata and P. André, "Assessment and mitigation of Erbium–doped fibre amplifiers (EDFA) gain transients in hybrid wavelength division multiplexing/time division multiplexing passive optical network (WDM/TDM PON) in the presence of packet–based traffic," *IET Optoelectronics*, vol. 4, no. 6, pp. 219–225, Jun. 2010.

1.6.2 Conferences

- **J. Ferreira**, D. Fonseca, P. Monteiro, A. Pinto and L. Rapp, "Dynamics of SHB and SDP on 9XX EDFAs: dependence on spectral allocation of input channels," in *Proc. Inter. Conf. on Transparent Optical Networks - ICTON*, Cartagena, Spain, Vol. Th.A2.3, pp. 1 – 4, Jun. 2013.
- **J. Ferreira**, D. Fonseca, P. Monteiro and A. Pinto, "Efficient algorithm for designing broadband Raman fiber amplifiers," in *Proc. Conf. on Telecommunications - ConfTele*, Castelo Branco, Portugal, Vol. 1, pp. 1 – 4, May 2013.
- **J. Ferreira**, R. Nogueira, P. Monteiro, A. Pinto, "A Simplified gain model for counter–pumped Raman fiber amplifiers," in *Proc. Symp. on Enabling Optical Networks - SEON*, Aveiro, Portugal, Jul. 2011.
- **J. Ferreira**, R. Nogueira, P. Monteiro, A. Pinto, "Raman amplifier undepleted pump model customization to include pump–to–pump interactions," in *Proc. EUROCON and Conf. on Telecommunications - ConfTele*, Lisboa, Portugal, Vol. 1, pp. 1 - 4, Jun. 2011.
- **J. Ferreira**, M. Fugihara and A. Pinto, "Energy efficient Raman fiber amplifiers suitable for dynamic optical networks," in *Proc. European Conference on Networks and Optical Communications - NOC*, Faro, Portugal, Jun. 2010.

1.6.3 Patents

- **J. Ferreira**, A. Pinto and P. Mão–Cheia, "Método e mecanismo para controlo e mitigação do efeito transitório em amplificadores ópticos de Raman com reflexão das bombas," 104930, Dec. 2009.

1.6.4 Other Contributions

- Inclusion of the simplified model for the gain and ASE noise estimation, presented in Chapter 3, in a network planning tool used by the hosting company.
- Inclusion of the model for the two–level and three–level EDFA considering the SHB and SDP effects, presented in Chapter 5 and in Chapter 2, respectively, in a EDFA simulation tool of the hosting company.

References

[1] J. Lee, Y. Chang, and Y. Han, "A detailed experimental study on single-pump Raman/EDFA hybrid amplifiers: static, dynamic, and system performance comparison," *IEEE/OSA Journal of Lightwave Technology*, vol. 23, no. 11, pp. 3484–3493, Nov. 2005.

[2] H. Kawakami, "Suppression of the cross-gain modulation in remotely-pumped EDF/DRA hybrid inline amplifier systems with online otdr for gain monitoring," *IEICE Transactions on Communications*, vol. E88-B, no. 5, pp. 1986–1993, May 2005.

[3] C. Headley and G. Agrawal, *Raman amplification in fiber optical communication systems.* Academic press, 2005.

[4] E. Desurvire, *Erbium-doped fiber amplifiers: principles and applications.* Wiley, 1994.

[5] E. Rouzic, "Physical impairment awareness in the context of an operator infrastructure," in *Proc. International Conference on Photonics in Switching*, Sep. 2009, pp. 1–4.

[6] G. Agrawal, *Lightwave technology: telecommunication systems.* John Wiley and Sons, 2005, vol. 2.

[7] G. Ellinas and J. Labourdette, "Network control and management challenges in opaque networks utilizing transparent optical switches," *IEEE Communications Magazine*, vol. 42, no. 2, pp. 16–24, Feb. 2004.

[8] A. Morea, F. Leplingard, and T. Zami, "New transmission systems enabling transparent network perspectives," *Comptes Rendus Physique*, vol. 9, no. 9, pp. 985–1001, Nov. 2008.

[9] T. Zami, A. Morea, F. Leplingard, N. Brogard, D. Bayart, S. Bigo, and J. Faure, "Driving technologies addressing the future dynamic transparent core networks," in *Proc. International Conference on Transparent Optical Networks (ICTON)*, vol. 2, Jun. 2008, pp. 194–197.

[10] A. Morea and J. Poirrier, “A critical analysis of the possible cost savings of translucent networks,” in *Proc. Design of Reliable Communication Networks*, vol. 3, Oct. 2005, pp. 707–708.

[11] G. Charlet and J. Renaudier, “Transmission of 16.4 bit/s capacity over 2550 km using PDM QPSK modulation format and coherent receiver,” *IEEE/OSA Journal of Lightwave Technology*, vol. 27, no. 3, pp. 153–157, Feb. 2009.

[12] Y. Huang, J. Heritage, and B. Mukherjee, “Connection provisioning with transmission impairment consideration in optical WDM networks with high-speed channels,” *IEEE/OSA Journal of Lightwave Technology*, vol. 23, no. 3, pp. 982–993, Mar. 2005.

[13] S. Azodolmolky, M. Klinkowski, and E. Marin, “A survey on physical layer impairments aware routing and wavelength assignment algorithms in optical networks,” *Elsevier Computer Networks*, vol. 53, no. 7, pp. 926–944, May 2009.

[14] A. Iselt, “Redefining optical networks with software defined networking intelligence,” in *Proc. ITG Symposium of Photonic Networks*, May 2014, pp. 1–4.

[15] C. Chen and W. Wong, “Transient effects in saturated Raman amplifiers,” *IET Electronics Letters*, vol. 37, no. 6, pp. 371–373, Jan. 2001.

[16] K. Motoshima, L. Leba, D. Chen, M. Downs, T. Li, and E. Desurvire, “Dynamic compensation of transient gain saturation in erbium-doped fiber amplifiers by pump feedback control,” *IEEE Photonics Technology Letters*, vol. 5, no. 12, pp. 1423–1426, Dec. 1993.

[17] A. Srivastava and J. Zyskind, “Fast-link control protection of surviving channels in multiwavelength optical networks,” *IEEE Photonics Technology Letters*, vol. 9, no. 12, pp. 1667–1669, Dec. 1997.

[18] Y. Sun, A. Srivastava, J. Zyskind, and J. Sulhoff, “Fast power transients in WDM optical networks with cascaded EDFAs,” *IET Electronics Letters*, vol. 33, no. 4, pp. 313–314, Feb. 1997.

[19] Y. Sun, J. Zyskind, and A. Srivastava, “Average inversion level, modeling, and physics of erbium-doped fiber amplifiers,” *IEEE Journal of Selected Topics in Quantum Electronics*, vol. 3, no. 4, pp. 991–1007, Aug. 1997.

[20] M. Karásek and M. Menif, “Channel addition/removal response in Raman fiber amplifiers: modeling and experimentation,” *IEEE/OSA Journal of Lightwave Technology*, vol. 20, no. 9, pp. 1680–1687, Sep. 2002.

[21] T. Zambelis, N. Gryspolakis, and L. Chen, “Design of all-optical gain-clamped discrete fiber Raman amplifiers,” in *Proc. Lasers and Electro-Optics Society (LEOS)*, Oct. 2003, p. ThFF1.

[22] C. Chen, J. Ye, W. Wong, Y. Lu, M. Ho, Y. Cao, M. Gassner, J. Pease, H. Tsai, H. Lee, W. Lu, S. Cabot, and Y. Sun, “Control of transient effects in distributed and lumped Raman amplifiers,” *IET Electronics Letters*, vol. 37, no. 21, pp. 1304–1305, Oct. 2001.

[23] M. Karásek and M. Menif, “Protection of surviving channels in pump-controlled gain-locked Raman fibre amplifier,” *Optics Communications*, vol. 210, no. 1, pp. 57–65, Sep. 2002.

[24] H. Feng and E. Patzak, “Methods for stabilizing the gain of EDFAs in burst switching optical networks,” *Photonic Network Communications*, vol. 4, no. 2, pp. 151–166, May 2002.

[25] T. Zami, A. Morea, F. Leplingard, and N. Brogard, “The relevant impact of the physical parameters uncertainties when dimensioning an optical core transparent network,” in *Proc. European Conference on Optical Communication (ECOC)*, vol. 3, Sep. 2008, p. We.3.D.2.

[26] Y. Zhang and P. Chowdhury, “Energy efficiency in telecom optical networks,” *IEEE Communications Surveys and Tutorials*, vol. 12, no. 4, pp. 441–458, Jul. 2010.

[27] L. Chiaraviglio, M. Mellia, and F. Neri, “Reducing power consumption in backbone networks,” in *Proc. International Conference on Communications (ICC)*, Jun. 2009, pp. 1–6.

[28] J. Nicholson, “Dispersion compensating Raman amplifiers with pump reflectors for increased efficiency,” *IEEE/OSA Journal of Lightwave Technology*, vol. 21, no. 8, pp. 1758–1762, Aug. 2003.

[29] J. Nicholson, “Discrete Raman amplifiers with pump reflectors for increased gain and efficiency,” in *Proc. European Conference on Optical Communication (ECOC)*, Sep. 2002, pp. 1–2.

[30] K. Ennser, T. Rogowski, G. Sacchi, M. Ibsen, O. Quargnolo, J. Shmulovich, G. Della Valle, and S. Taccheo, “Power transients control in transparent WDM networks,” in *Proc. International Conference on Transparent Optical Networks (ICTON)*, Jul. 2005, p. Tu.B2.5.

[31] L. Rapp, “Transient behavior of EDFA stages using pump power splitting or pump bypass technique,” *IEEE/OSA Journal of Lightwave Technology*, vol. 25, no. 3, pp. 726–732, Mar. 2007.

[32] D. Kovsh, S. Abbott, E. Golovchenko, and A. Pilipetskii, “Gain reshaping caused by spectral hole burning in long EDFA-based transmission links,” in *Proc. Optical Fiber Communication Conference (OFC)*, Mar. 2006, p. OTuK7.

[33] M. Yadlowsky, “Pump wavelength dependent spectral hole burning in EDFAs,” *IEEE/OSA Journal of Lightwave Technology*, vol. 17, no. 9, pp. 1643–1648, Sep. 1999.

[34] M. Bolshtyansky, N. King, and G. Cowle, “Characterization of site dependent pumping in EDFA,” in *Proc. Optical Amplifiers and Their Applications (OAA)*, Aug. 2005, p. WB5.

[35] J. Ferreira, R. Nogueira, P. Monteiro, and A. Pinto, “Weighted undepleted pump model for broadband counter-pumped Raman fiber amplifiers,” *IEEE/OSA Journal of Optical Communications and Networking*, vol. 4, no. 8, pp. 595–602, Aug. 2012.

[36] J. Ferreira, M. Fugihara, and A. Pinto, “Transient response and control of pump-reflecting Raman fiber amplifiers,” *Fiber and Integrated Optics*, vol. 29, no. 1, pp. 44–61, Dec. 2009.

[37] J. Ferreira, A. Pinto, and P. Mão Cheia, “Método e mecanismo para controlo e mitigação do efeito transitório em amplificadores ópticos de Raman com reflexão das bombas,” Patent: 104930, Dec. 2009.

[38] L. Rapp and J. Ferreira, “Dynamics of spectral hole burning in EDFAs: dependency on pump wavelength and pump power,” *IEEE Photonics Technology Letters*, vol. 22, no. 16, pp. 1256–1258, Aug. 2010.

[39] J. Ferreira and L. Rapp, “Dynamics of spectral hole burning in EDFAs: dependence on temperature,” *IEEE Photonics Technology Letters*, vol. 1, no. 24, pp. 67 – 69, Jan. 2011.

[40] J. Ferreira, D. Fonseca, P. Monteiro, A. Pinto, and L. Rapp, “Site Dependent Pumping Effect on Two-level EDFAs,” *IEEE/OSA Journal of Lightwave Technology*, vol. 33, no. 2, pp. 285–292, Jan. 2015.

Chapter 2

Models for Optical Fiber Amplifiers

An optical fiber amplifier is a term commonly attributed to a fiber component that increases the optical signal power, without performing any optical–electrical–optical (OEO) conversion. Optical fiber amplifiers can be considered an enabling technology for dense wavelength–division multiplexing (DWDM) and transparent and dynamic optical networks, due to the possibility of amplifying several wavelength–division multiplexing (WDM) channels simultaneously. Nowadays, the most common optical fiber amplifiers are Raman fiber amplifiers (RFAs) [1] and erbium–doped fiber amplifiers (EDFAs) [2]. In order to design and operate an optical fiber amplifier to be used on transparent and dynamic optical networks there are some fundamental parameters that need to be considered, such as bandwidth, gain, and output power [2]. Also, system and technological parameters such as noise, signal distortion, packaging, bulkiness and consumption, need to be addressed. Finally, other extra functionalities, such as transient mitigation, have to be included to ensure the gain stabilization of the amplifier [3]. Since optical fiber amplifiers are a key component of optical networks, their characteristics and the models usually used to simulate their behavior will be discussed.

In this chapter, we present the RFAs and EDFAs principle of operation, configurations and models, which will be used in the following chapters of this thesis. The experimental validation of the implemented models is also presented in this Chapter. The models implemented and validated for the RFA, in Section 2.3, were published in [4, 5], and for the EDFA, presented in Section 2.4, was published in [6].

2.1 Introduction

RFAs provide a simple and unique technology for the long and ultra–long distances [7, 8]. In a RFA, the gain medium is the optical fiber itself [9]. Therefore, the gain of the RFA can be distributed over the transmission length. In a RFA, one or more optical pumps are coupled to the transmission fiber and provide gain to the signals. The energy of the pumps is transferred to the signals by a nonlinear optical process known as stimulated Raman scattering (SRS) [1]. In silica fibers, the wavelength subject to the highest gain is around 13.2 THz afar from each pump wavelength [1]. Therefore, by a proper selection of pump wavelengths, the RFA may be adjusted to amplify any given optical wavelength [10]. RFAs have some key advantages, such as the presence of the Raman gain in every fiber [11], which provides an economical mean of upgrading the transmission systems, only by changing the transmission link interfaces. Also, the gain is available over the entire region of the transmission bandwidth. Another advantage is the fact that the gain ripple can be optimized by adjusting the number, wavelengths, and power of the pumps [12, 13]. Despite these advantages, a number of challenges delayed the early adoption of RFAs. RFAs have a relatively low pumping efficiency and require longer fibers when compared with EDFAs. This disadvantage can be mitigated using a dispersion compensating fiber (DCF) as amplification medium, since the DCF has a higher Raman gain than the standard single mode fiber (SSMF). Another disadvantage is the fast response time of the amplifier, which can be a source of signal degradation [14]. When compared to EDFAs, RFAs require the use of higher input pump powers. Finally, some concerns about the laser safety in RFAs can be raised, due to the need to inject a high pump power into the transmission fiber.

Doped fiber amplifiers use a fiber that is doped with rare earth ions as gain medium [2]. The pump laser excites the dopant ions of the fiber to a higher energy level, and these can decay back to a lower energy level by stimulated emission of a photon at the wavelength of the signal. The fibers can be doped by any small amount of rare earth element such as erbium, neodymium, ytterbium, thulium [15, 16] and praseodymium. When the fiber is doped with erbium, the gain region covers the 1550 nm communication window [17, 18], with a relatively flat gain [19, 20]. By using the proper rare earth ion, doped fiber amplifiers have been designed to operate in the S–Band (1480-1520 nm), C–Band (1521–1560 nm), and L–Band (1561–1620 nm). It is possible to increase the pump efficiency or the amplification bandwidth by combining two or more dopants, such as ytterbium doped fiber combined with aluminum [21, 22]. Solutions for extended C–band with hybrid amplification, where an EDFA and a RFA are combined, were also proposed [16, 23, 24]. Doped fiber amplifiers are also insensitive to polarization and have negligible inter–channel cross–talk [2]. Moreover, they present a high power transfer efficiency from pump to signal wavelength, a high saturation output power, and a low noise figure. Another reason for the success of EDFAs is the low cost of the pump laser.

One of the problems affecting the RFAs and EDFAs is the generation and amplification of amplified spontaneous emission (ASE) noise. The excited medium can also decay spontaneously, this effect is also known as spontaneous emission. This spontaneous emission will compete with the stimulated emission and reduce the amplification efficiency [2]. For this reason, there is always some output power due to the ASE noise, even without input signals. Typically, the RFA has less noise generation when compared with the EDFA.

This chapter is organized as follows. In Section 2.2, we describe a typical optical transmission link, and highlight the amplifier configurations commonly used to extend the signal reach. In Section 2.3, we discuss the SRS effect and present the RFA propagation equations for the steady–state and for the dynamic–regime. Afterwards, we introduce the average power analysis (APA) numerical model, which is implemented to solve the propagation equations for the steady–state and for the dynamic–regime. A validation of the implemented numerical model and the discussion of its accuracy is also presented. In Section 2.4, we examine in detail the principle of operation of the EDFA, focusing on the impact of the inhomogeneous gain broadening. Considering that the inhomogeneous gain broadening can be described by the statistical variations of the absorption and emission parameters, we derive and implement the two–level and the three–level models for the EDFA. An experimental validation of the implemented model for the three–level model is presented. The dependence of the three–level EDFA model on the pump wavelength and on channel spacing is also experimentally evaluated and discussed. Finally, conclusions are summarized in Section 2.5.

2.2 Amplification in an Optical Transmission Link

There are three basic elements in every transmission link: the transmitter, the communication channel, and the receiver. Fig. 2.1 shows a schematic diagram of an optical transmission link with the basic elements and with the amplifier elements highlighted. The transmitter and the receiver are located at the network nodes and the communication channel connects these two points. Several signals in the transmitter are coupled with an arrayed waveguide grating (AWG) and injected into the transmission fiber. At the receiver side, the signals are de–multiplexed with an AWG and detected with a photodiode. The complexity of both the transmitter and the receiver depends mostly on the modulation format, number of channels and other requirements [10, 25–27]. Other components, such as couplers, multiplexers, optical fiber amplifiers, and optical switches, provide the building blocks for more complex transmission links. For instance, long distance fiber optic transmission may require signal regenerators, signal repeaters, or optical amplifiers (such as EDFAs and RFAs), dispersion management equipment, remote monitoring interfaces, and error–correction components. The possibility of adding or dropping channels in the optical network node is achieved by incorporating reconfigurable optical add/drop multiplexer (ROADM), and couplers/splitters in the network node [27–30].

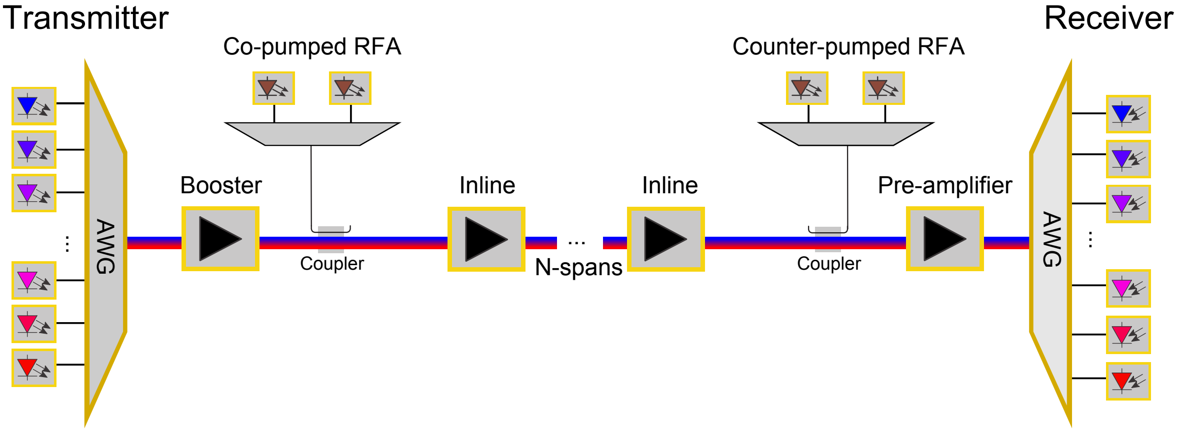

Figure 2.1: Schematic diagram of an optical transmission link with amplification elements.

Optical fiber amplifiers are extensively used in long distance fiber optic transmission systems [10, 31, 32]. In Fig. 2.1, we highlight five different solutions in which optical fiber amplifiers can be used to enhance the performance of optical signals. First, the output signal power of the transmitter can be increased with a high output power amplifier, called a booster, before entering a long transmission fiber [3, 33]. An optical fiber amplifier can also be used as a pre–amplifier, prior to a data receiver, if the incoming signal is below the minimum/optimum receiver input power. The aim of the pre–amplifier is to allow the detection of the signal by providing a high gain to the signals (while still adding a reduced ASE noise), instead of a high launch power, as is the case of boosters [31, 33]. Inline amplifiers are often used between long spans of transmission fiber. The use of multiple inline amplifiers in a long optic fiber link has the advantage of compensating the transmission losses without dropping the optical signal power to very low levels, which would degrade the optical signal–to–noise ratio (OSNR). Moreover, it avoids the use of high input signal powers at the input of the transmission fiber, which would cause the degradation of signals due to nonlinear effects [34]. These inline amplifiers are sometimes operated under difficult conditions, where there is high thermal amplitude [35], or where it is virtually impossible to perform any kind of maintenance, as in the deep ocean. Moreover, as shown in Fig. 2.1, it is also possible to use RFAs in a co–pumped or counter–pumped configuration to extend the signal reach. From all amplification choices, the link/network planner has to select the proper amplification technologies to ensure that the signals reach the receiver with enough quality and that all the requirements for the transmission link are addressed at the lowest possible cost [9].

2.2.1 Pump Configurations for the RFA

RFAs can be distributed or lumped [13, 31, 36]. The first case applies when the transmission fiber is the gain medium. On the other hand, when the gain fiber is a special fiber, like a DCF, the amplifier is lumped. Several pumping schemes have been proposed to enhance the performance of RFAs [9]. Fig. 2.2 shows three RFA pumping schemes, where one or more pumps are coupled with the transmission fiber. In the co–pumped configuration, Fig. 2.2(a), the pumps have the same direction of the signals propagating in the transmission fiber. Here, an optical isolator (ISO) is usually used to avoid damaging the components of the transmitter due to pump power reflections. In the counter–pumped configuration, Fig. 2.2(b), the signal and the pumps are propagated in opposite ways. An ISO is also used to avoid damaging the components of the transmitter. A third pumping scheme can be obtained when pumping in both directions, called the bidirectional configuration, Fig. 2.2(c). In this configuration the pumps are located at the beginning and at the end of the transmission fiber [8]. The pumping scheme usually implemented is the counter–pumped scheme [7]. One of the reasons for using this configuration is based on the fact that the pump lasers tend to have a large relative intensity noise (RIN) [14], which severally degrades the signal quality in a co–pumped scheme [37, 38]. Another disadvantage is the fact that amplifying the signals in a co–pumped scheme can increase the signal power to levels where the nonlinear effects degrade the signal quality [39]. The bidirectional pumping scheme has advantages, such as gain flatness and higher gain [40]. However, it has the disadvantage of using forward and backward independent pumps, increasing the amplifier cost.

A typical RFA can have more than two pumps in order to obtain an improved flattened gain. In some configurations, amplification bandwidths of up to 100 nm have been demonstrated [12, 35], and the transmission bandwidth can fall anywhere from

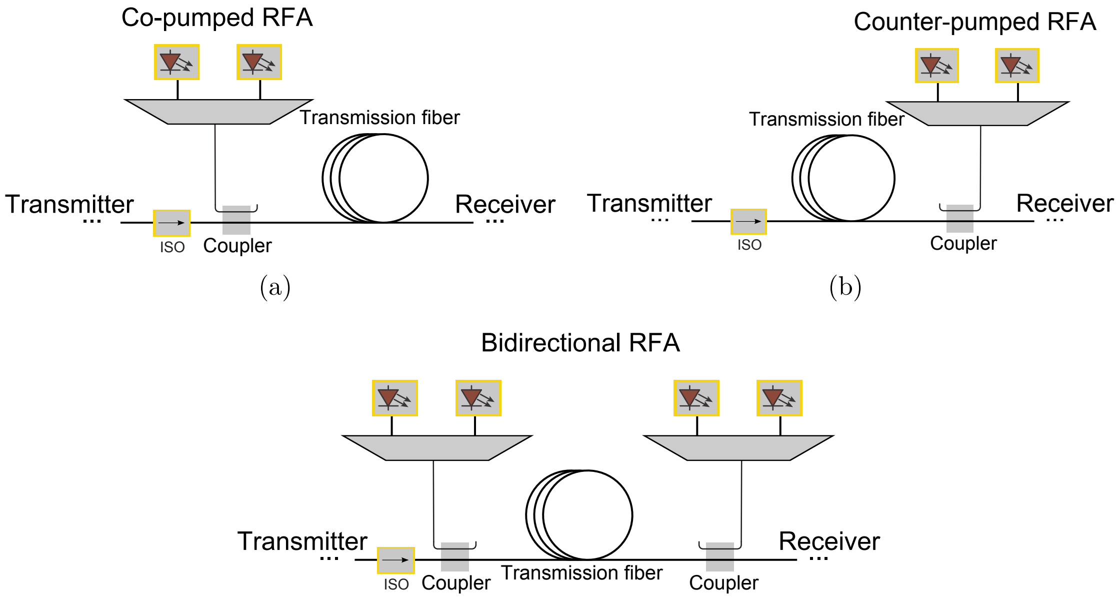

(a) (b) (c)

Figure 2.2: RFA pump configurations: a) co–pumped; b) counter–pumped; c) bidirectional.

1300 nm to 1650 nm. Recently, a Raman amplifier with a bandwidth of 136 nm was demonstrated, using a pump and signal interleaved scheme [13], where the higher pump wavelengths are within the signal band. Some alternative configurations have a high–order Raman amplification [7], where a pump with a high input power and shorter wavelength (e.g. 1350 nm) provides gain to a pump or a seed with a lower power and with a longer wavelength (e.g. 1450 nm), which in turn provides gain to the signals. The improvement of the performance comes from the fact that in a counter–pumped RFA, the pump close to the signals is amplified, which can result in an increase of the OSNR and in the flattening of the gain spectral characteristic [41]. In other configurations the amplification and the dispersion compensation may be combined in a DCF [31].

2.2.2 Pump Configurations for the EDFA

In the transmission link shown in Fig. 2.1, we can see the presence of a booster, a pre–amplifier and inline amplifiers. Typically, these amplifiers are either different configurations of EDFAs or the same configuration at different operating points. The simplest configuration of an EDFA is the single–stage. Fig. 2.3 shows three amplifier configurations for the single stage EDFA. This configuration comprises a single coil of erbium–doped fiber (EDF) with a length L and a pump [42]. The optical pump is combined with the optical signal in an EDF by a WDM coupler. If the pump is co–propagating with the signal, Fig. 2.3(a), it is called a co–pumped EDFA; if it is counter–propagating, Fig. 2.3(b), it is a counter–pumped EDFA. When the pumps are injected in both directions, it is a bidirectional EDFA, Fig. 2.3(c). The single stage design has several advantages, such as lower cost and easier design when compared to more complex EDFA configurations. However, due to its simplicity, it lacks several features which are important for the achievement of a controlled output power and a flatter gain over the C–band.

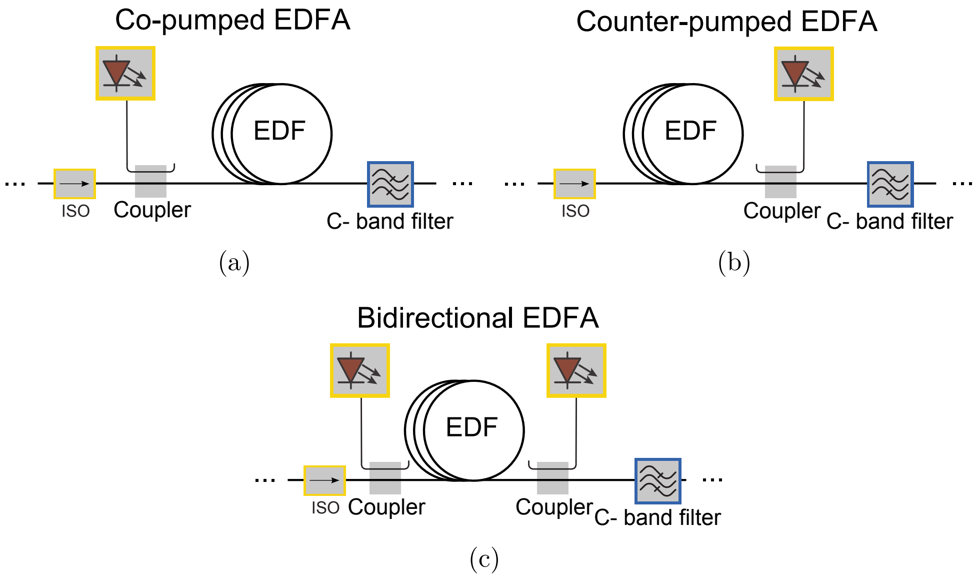

Figure 2.3: EDFA single stage configurations: a) co–pumped; b) counter–pumped; c) bidirectional.

An evolution of the single stage EDFA configuration is the dual–stage EDFA, as shown in Fig. 2.4. Here, two coils of EDF are cascaded and between them several devices can be included, such as an ISO, a variable optical attenuator (VOA), and a gain flattening filter. The ISO is used to prevent the reflected light from entering into first stage. The gain flattening filter can be designed based on a simple VOA or based on more complex filters, with the objective of flattening the gain of the amplifier. The number of pumps depends on the required output gain. In the example of Fig. 2.4, the pump power is split between the two coils. Several other components may be contained in a commercial fiber amplifier, such as fiber couplers and photodetectors for monitoring of optical power levels, and laser diodes with electronic pump control to control and mitigate transient effects.

Another EDFA configuration is the remote optically pumped amplifier (ROPA), where the pump power is injected further away from the EDF. Typically, the EDF is inserted in the middle of the transmission link and a pump centered around 1480 nm is injected at the beginning or at the end of the transmission fiber. Due to the low attenuation of the silica fiber around 1480 nm when compared with 980 nm region, the pump power will propagate through the fiber reaching the EDF, where the signals will be amplified. This configuration can be used in some systems to avoid the inclusion of active components, such as conventional EDFAs, in the middle of the link [43].

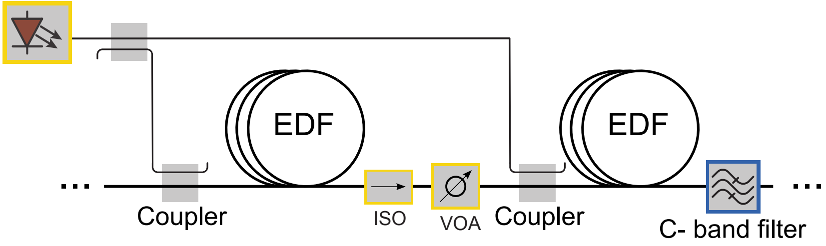

Figure 2.4: EDFA double stage configuration.

2.3 Model for RFAs

Raman scattering can be understood as an inelastic scattering process, in which the incident light on a medium is converted to a lower or higher frequency photon. The process can be described by an excitation of a vibrational mode up to a virtual level, induced by an incident photon, followed by a de–excitation and emission of a lower frequency photon [1]. If the medium is already excited it is possible to occur also the emission of higher frequency photons. The emitted photons can be called Stokes photons, if they are shifted to lower frequencies, or anti–Stokes photons, if they are shifted to higher frequencies. Other scattering processes can occur when the light interacts with a medium, such as Rayleigh scattering, which is an elastic process in which the photon energy is conserved.

Figure. 2.5 shows a schematic diagram of the vibrational energy levels representing the Raman scattering process. When considering the emission of a Stokes photon, one incident photon with the energy $E_i = h\nu_i$, where h is the Planck constant and ν_i the photon frequency, excites a vibrational mode from the ground state to a virtual energy level. After some time, typically 10^{-12}s [1], a photon of energy $E_e = E_i - E_v$ is emitted and the vibrational mode returns the first excited vibrational state, E_v. When the material already has some vibrational modes at the first excited vibrational state, an incident photon with energy of E_i can excite the vibrational mode to a virtual energy level, and consequently, a photon is emitted and the vibrational mode returns to ground level. The emitted photon, called anti–Stokes photon, has the energy of the incident photon plus the energy of the phonon present in the material. Since the anti–Stokes process occurs with a lower probability than the Stokes process, usually it is not considered in the processes of signal amplification [1].

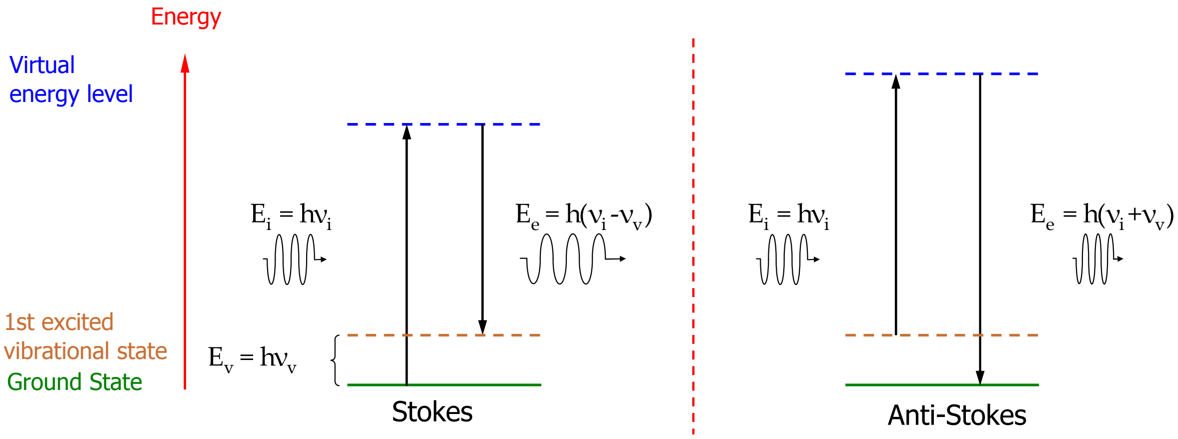

Figure 2.5: Schematic diagram of the energy levels representing the Raman scattering resulting on the emission of a Stokes photon and an anti–Stokes photon.

When considering an optical fiber, the Raman emission process can also be stimulated by a signal photon. In this process, a pump photon is converted into a second signal photon, which is a replica of the first, and the remaining energy produces an optical phonon. This process is the gain mechanism behind Raman amplification. The most important parameter characterizing Raman amplifiers is the gain coefficient, g_r, since it describes how the signal power grows due to SRS. Due to the amorphous nature of silica, which allows a continuum of molecular vibrational frequencies, the Raman gain curve is fairly broad. In silica fibers, a peak is observable for a frequency shift equal to 13.2 THz [1]. An important quantity, the Raman gain efficiency of the fiber, g_R, relates Raman gain coefficient with the effective area of the fiber, A_{eff},

$$g_R(\nu - \varsigma) = \frac{g_r(\nu - \varsigma)}{A_{eff}}, \tag{2.1}$$

where $g_r(\nu - \varsigma)$ is the Raman gain coefficient of the fiber between the frequencies ν and ς. The small effective area of a DCF ($15\,\mu\text{m}^2$) is the main reason for its higher Raman gain efficiency, when compared to a SSMF ($80\,\mu m^2$), or with a dispersion shifted fiber (DSF) ($50\ \mu\text{m}^2$).

Also, larger gain coefficients are obtained when the pump polarization state and the incident light are parallel, with smaller values obtained for perpendicular polarizations [1]. The copolarized gain is almost one order of magnitude larger than the orthogonal polarization gain near the peak of the Raman curve. Nevertheless, a polarization independent Raman amplifier can be designed by using one pump for each polarization, to avoid this dependence.

2.3.1 Propagation Equations for RFAs

A mathematical model that describes the time evolution of pumps, signals, and ASE noise powers (in forward and backward directions) along the fiber is given by the following set of coupled differential equations [44]

$$\begin{aligned}
\frac{\partial P^{\pm}(z,\nu,t)}{\partial z} \mp \frac{1}{v_g(\nu)}\frac{\partial P^{\pm}(z,\nu,t)}{\partial t} &= \mp\alpha(\nu)P^{\pm}(z,\nu,t) \pm \gamma(\nu)P^{\mp}(z,\nu,t) \\
&\pm \sum_{\varsigma>\nu}\left\{\frac{g_r(\nu-\varsigma)}{K_{eff}A_{eff}}[P^{\pm}(z,\varsigma,t)+P^{\mp}(z,\varsigma,t)]P^{\pm}(z,\nu,t)\right. \\
&\left.\pm\, h\nu\frac{g_r(\nu-\varsigma)}{A_{eff}}[P^{\pm}(z,\varsigma,t)+P^{\mp}(z,\varsigma,t)]E_{\varsigma\nu}\Delta\nu\right\} \\
&\mp \sum_{\varsigma<\nu}\left\{\frac{\nu}{\varsigma}\frac{g_r(\nu-\varsigma)}{K_{eff}A_{eff}}[P^{\pm}(z,\varsigma,t)+P^{\mp}(z,\varsigma,t)]P^{\pm}(z,\nu,t)\right. \\
&\left.\mp\, 2h\varsigma\frac{g_r(\nu-\varsigma)}{A_{eff}}[P^{\pm}(z,\varsigma,t)+P^{\mp}(z,\varsigma,t)]E_{\nu\varsigma}\Delta\varsigma\right\},
\end{aligned} \tag{2.2}$$

and

$$E_{\varsigma\nu} = 1 + \frac{1}{\exp\left(\frac{h(\varsigma-\nu)}{k_BT}\right)-1}, \tag{2.3}$$

$$E_{\nu\varsigma} = 1 + \frac{1}{\exp\left(\frac{h(\nu-\varsigma)}{k_BT}\right)-1}, \tag{2.4}$$

where $P^{+}(z,\nu,t)$ and $P^{-}(z,\nu,t)$ are the optical powers of co–propagating and counter–propagating pumps and signals, respectively, ν and ς are the pumps or signals frequencies, $\alpha(\nu)$ is the attenuation coefficient of the fiber, $\gamma(\nu)$ is the Rayleigh backscattering coefficient, K_{eff} is the polarization factor between signals and pumps, k_B is the Boltzmann's constant, $v_g(\nu)$ is the group velocity, h is the Planck's constant, $\Delta\nu$ and $\Delta\varsigma$ are effective noise bandwidths, and T the absolute temperature of the fiber. For a total number of pumps, N_p, a total number of signals, N_s, and a total number of spectral components for ASE noise for each direction, $\Delta\nu$, N_{ASE}, the system is formed by $N_p + N_s + 2N_{ASE}$ equations.

In eq. (2.2), the first two terms on the right hand side refer to the attenuation of the fiber and Rayleigh backscattering. The third term refers to the gain, and the fifth term refers to losses due to the SRS. The fourth and sixth terms represent the ASE noise generation and its dependency on the temperature and amplifier gain.

2.3.2 Average Power Analysis Model: Steady–State Regime

To obtain a steady–state power distribution, the time derivative in eq. (2.2) can be settled to zero. To solve the propagation equation numerically we can use several methods, such as the shooting method [45], the iterative fourth-order Runge-Kutta (RK4) routine, or APA [46], among others. Since the propagation equations need to be solved for a counter–pumped RFA with several pumps and several signals, the convergence of the shooting method for some cases is not assured [47]. Therefore, we implemented the APA method [48], which presents a similar accuracy and is computationally more efficient than the RK4 [46]. In order to implement this method, the length of the amplifier fiber is divided in S sections, each with a length of Δz. For small values of Δz, a stationary distribution inside each section can be assumed [48]. Therefore, the output pump/signal power at each section end and ASE noise is given by [48]

$$P^{\pm}_{out} = P^{\pm}_{in} G(z,\nu), \tag{2.5}$$

$$\Delta P^{\pm}_{ASE} = 2h\nu n^{\pm}_{sp}(z,\nu)\Delta\nu(G(z,\nu)-1), \tag{2.6}$$

with $n^{\pm}_{sp}(z,\nu)$ given by

$$n^{\pm}_{sp}(z,\nu) = \frac{C(z,\nu)+\gamma(\nu)P^{\mp}(z,\nu)/2h\nu\Delta\nu}{A(z,\nu)-B(z,\nu)-D(z,\nu)-\alpha(\nu)}, \tag{2.7}$$

where $P^{\pm}_{out}$ is the output power, $P^{\pm}_{in}$ is the input power, Δz is the length of the fiber section, and $G(z,\nu)$ is the the section gain. $G(z,\nu)$ is given by [48]

$$G(z,\nu) = \exp[\{A(z,\nu)-B(z,\nu)-D(z,\nu)-\alpha(\nu)\}z]. \tag{2.8}$$

Since the amplifier fiber is divided in several small sections, $A(z,\nu)$, $B(z,\nu)$, $C(z,\nu)$ and $D(z,\nu)$, are given by

$$A(z,\nu) = \sum_{\varsigma>\nu} \frac{g_r(\nu-\varsigma)}{K_{eff}A_{eff}}[P^{\pm}(z,\varsigma)+P^{\mp}(z,\varsigma)], \tag{2.9}$$

$$B(z,\nu) = \sum_{\varsigma<\nu} \frac{\nu}{\varsigma}\frac{g_r(\nu-\varsigma)}{K_{eff}A_{eff}}[P^{\pm}(z,\varsigma)+P^{\mp}(z,\varsigma)], \tag{2.10}$$

$$C(z,\nu) = \sum_{\varsigma>\nu} \frac{g_r(\nu-\varsigma)}{2A_{eff}}[P^{\pm}(z,\varsigma)+P^{\mp}(z,\varsigma)]\left(1+\frac{1}{\exp\left(\frac{h(\varsigma-\nu)}{k_BT}\right)-1}\right), \tag{2.11}$$

$$D(z,\nu) = \sum_{\varsigma<\nu} \frac{g_r(\nu-\varsigma)}{A_{eff}}2h\varsigma\Delta\varsigma\left(1+\frac{1}{\exp\left(\frac{h(\nu-\varsigma)}{k_BT}\right)-1}\right). \tag{2.12}$$

With the objective of minimizing the error factor, the optical power term in each section can be replaced by its average at each section, using [48]

$$\langle P(\nu)\rangle = P_{in}^{\pm}(\nu)\frac{G(\nu)-1}{\ln G(\nu)}, \tag{2.13}$$

and, for the ASE noise

$$\langle \Delta P_{ASE}(\nu)\rangle = 2h\nu n_{sp}^{\pm}\Delta\nu\left\{\frac{G(\nu)-1}{\ln G(\nu)}-1\right\}. \tag{2.14}$$

To determine the output powers of the amplifier we need to calculate the power in each amplifier section for every signal, pump and ASE noise wavelengths. Therefore,

$$\begin{aligned} P_k^{+}(z_{d+1}) &= P_k^{+}(z_d)G_k(z_d), \\ P_k^{-}(z_{d+1}) &= P_k^{-}(z_d)/G_k(z_d), \end{aligned} \tag{2.15}$$

where subscript d denotes the sections and $G_k(z_d)$ is the gain within $]z_d, z_{d+1}]$, for the signal, ASE noise, and pumps with the index k. In the case of existing backward propagating pumps, an iterative process is used, solving the equation for the forward signals and then for the backward signals. In our implementation, the iteration process is stopped when the changes between two successive iterations, for all the optical signal powers, are smaller than 0.001 %.

Experimental Validation of the Gain Estimation

The experimental setup implemented used to validate the numerical model is presented in Fig. 2.6. The optical fiber is a SSMF with 40 km and 0.2 dB/km of attenuation around 1550 nm. The pumps P_1, P_2, P_3, and P_4 are coupled to the fiber using an optical multiplexer (MUX), followed by an optical WDM coupler (backward coupler). The pumps P_1, P_2, P_3, P_4 are centered at 1426 nm, 1444 nm, 1462 nm, and 1487 nm, with optical powers of 167.5 mW, 106.7 mW, 48.9 mW, and 134 mW, respectively. The attenuation of the fiber for these wavelengths is 0.25 dB/km, 0.25 dB/km, 0.22 dB/km, and 0.22 dB/km, respectively. The tunable laser is used as the signal to be amplified, with -4 dBm of input optical power. The Raman gain coefficient as function of the frequency spacing between the two waves is obtained using the technique presented in [49]. This technique is based on fitting measured Raman On/Off gain results with Gaussian curves. The signal output power is measured with an optical spectrum analyzer (OSA). Assuming fully scrambled polarization states, the K_{eff} is considered to be two [50], and the wavelength dependent Rayleigh scattering coefficient $\gamma(\nu) = 2.3510^{-25}/\lambda^3$ [12].

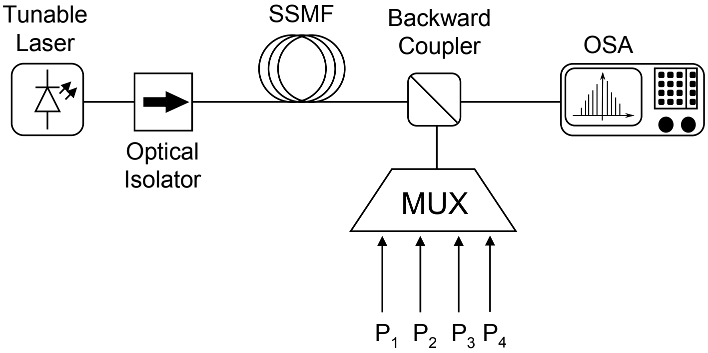

Figure 2.6: Experimental setup used to measure the amplifier On/Off gain.

The On/Off gain of the RFA amplifier for a wavelength s, G_s, in decibels, is given by

$$G_s = 10\log_{10}\left(\frac{P_{s,ON}(L)}{P_{s,OFF}(L)}\right), \tag{2.16}$$

where $P_{s,ON}(L)$ is the signal output power with amplification (when the pumps are ON) and $P_{s,OFF}(L)$ the signal output power without amplification (when the pumps are OFF).

We measure the On/Off gain with a probe signal from 1515 nm to 1600 nm, and simulate the setup with the implemented model. Fig. 2.7 shows the On/Off gain for the considered setup, obtained with experimental measurements and with the implemented numerical model. The comparison between the results obtained experimentally and numerically shows good agreement, with a maximum deviation of 0.3 dB in a window of 85 nm. These results indicate that the numerical model describes accurately the proposed system in the steady–state regime.

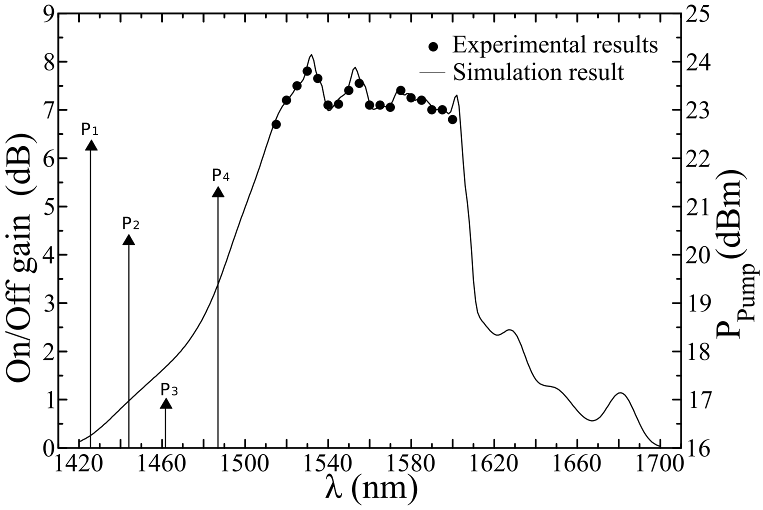

Figure 2.7: On/Off gain measured for the system presented in Fig. 2.6. The symbols represent the measured On/Off gain; the line represents the simulation results; the arrows represent the pumps power.

Experimental Validation of the ASE Noise Estimation

To evaluate the results of the numerical model with ASE noise, we experimentally measured the ASE noise of a counter–pumped RFA with 2 pumps. Fig. 2.8 shows a schematic diagram of the experimental setup implemented. The pumps P_1 and P_2 are centered at 1426 nm and 1444 nm, with 355.4 mW and 256.8 mW of input pump power, respectively, and are coupled to the fiber using an MUX, followed by an optical WDM coupler (backward coupler). A SSMF with 80 km is used with an attenuation coefficient of 0.25 dB/km and 0.24 dB/km for each pump, respectively, and with 0.20 dB/km for the signals. The ASE noise power is measured with an OSA, with the resolution bandwidth of 2.5 GHz, and without signals.

Figure 2.9 shows the output ASE noise power obtained both with experimental measurements and with the implemented numerical model. Inspection of the figure shows a difference between the experimental and numerical results in wavelengths ranging from 1510 nm to 1520 nm. From other experimental measurements, we verify that this difference is due to the attenuation of the WDM coupler between the pumps and

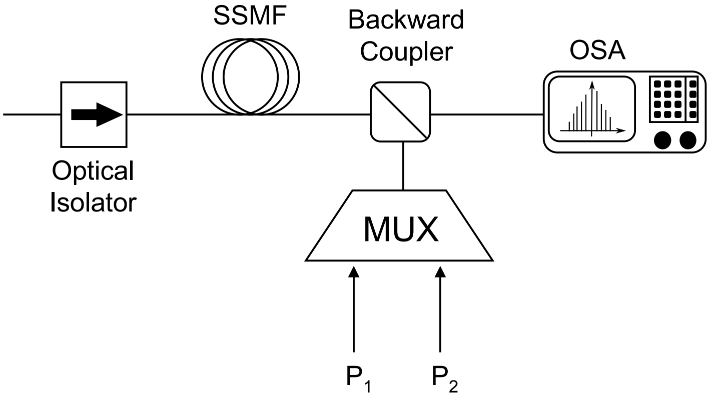

Figure 2.8: Experimental setup used to measure the amplifier ASE noise.

the fiber at the end of the transmission fiber. By comparing the results from 1520 nm to 1570 nm, we show that the numerical model describes with good accuracy the generation and amplification of noise in the amplifier.

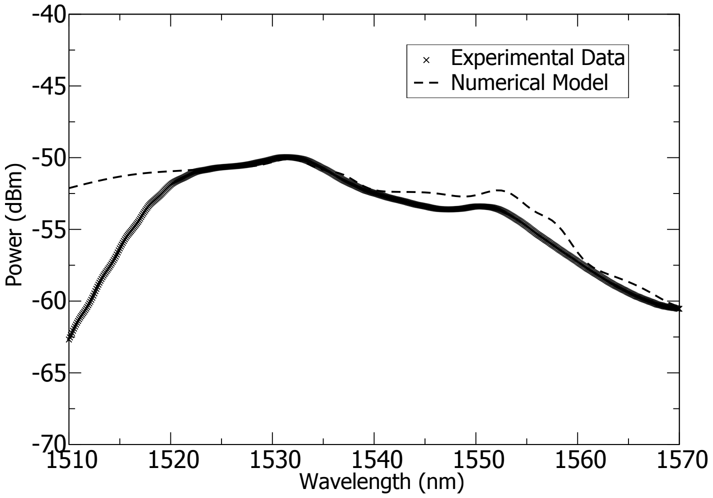

Figure 2.9: Output ASE noise power measured for the system presented in Fig. 2.8. The crosses represent the measured ASE noise power; the dashed line represents the simulation results.

2.3.3 Average Power Analysis Model: Dynamic Regime

When considering the time derivative on eq. (2.2), we obtain the time evolution of signals and pumps in a RFA. Since we are interested in measuring the power variation of the surviving channels when compared with the output signal powers, the terms that contribute to the creation of optical noise and Rayleigh backscattering can be neglected [51]. Thus, the propagation equations for the RFA can be expressed by

$$\begin{aligned}\frac{\partial P^{\pm}(z,\nu,t)}{\partial z} \mp \frac{1}{v_g(\nu)}\frac{\partial P^{\pm}(z,\nu,t)}{\partial t} &= \mp\alpha(\nu)P^{\pm}(z,\nu,t)\\ &\pm \sum_{\varsigma>\nu}\left\{\frac{g_r(\nu-\varsigma)}{K_{eff}A_{eff}}[P^{\pm}(z,\varsigma,t)+P^{\mp}(z,\varsigma,t)]P^{\pm}(z,\nu,t)\right\} \qquad (2.17)\\ &\mp \sum_{\varsigma<\nu}\left\{\frac{\nu}{\varsigma}\frac{g_r(\nu-\varsigma)}{K_{eff}A_{eff}}[P^{\pm}(z,\varsigma,t)+P^{\mp}(z,\varsigma,t)]P^{\pm}(z,\nu,t)\right\}.\end{aligned}$$

To numerically solve the time dependent equations of the amplifier, eq. (2.17), we customized the APA method according to [51]. In the proposed model, the signals and pumps are assumed to propagate at the same velocity from section to section, meaning that the group velocity of the different wavelengths are not included in the model. This is not a severe limitation for most of the contexts in which it is used, as the signals propagation time can be assumed to be equal when compared with the transient time. The length of the amplifier fiber is divided in S sections with a length of Δz. Knowing that $\tau = L/v_g$ is the propagation time of the light in the fiber, dividing τ by S sections of Δz, we obtain Δt, which defines the time taken by the light to transverse each section Δz. Δt and Δz are related by the equation $\Delta z = v_g \Delta t$. Using Δt, we can divide the total time of the simulation into N sections. For small values of Δz and Δt, a stationary distribution can be assumed in Δz, as well as in Δt [52]. Therefore we obtain

$$P_k^{+}(z_{d+1},t_{n+1}) = P_k^{+}(z_d,t_n)G_k(z_d,t_n), \qquad (2.18)$$

$$P_k^{-}(z_{d+1},t_{n+1}) = P_k^{-}(z_d,t_n)/G_k(z_d,t_n), \qquad (2.19)$$

where the subscripts d and n denote sections of distance and time, respectively, and $G_k(z_d,t_n)$ is the gain within $]z_d,z_{d+1}]$ at the time instant n, for the signal k.

Using the steady–state power distributions as initial conditions for the system, when $t = 0$, we calculate the time and space evolution of the optical powers inside the amplifier. For each increment in time, Δt, we redefine the boundary conditions of the amplifier. Thus, by changing the channels input powers, we reproduce the channel add/drop. In the case of existing backward propagating pumps, an iterative process is used, solving the eq. (2.18) for forward signals and eq. (2.19) for backward signals. Similarly to the numerical model implemented for the steady–state regime, the iteration process is stopped when the changes between two successive iterations, for all the optical signal powers, are smaller than 0.001 %.

Experimental Validation

To perform experimental measurements of the dynamic response of the amplifier presented in Section 2.3.2, we co–propagate a continuous wave signal, S_1, and a modulated signal, S_2. Fig. 2.10 shows a schematic diagram of the experimental setup implemented to measure the gain deviation of the surviving channel S_1 due to the add/drop of the signal S_2. The signal S_2 is turned ON and OFF with a frequency of 250 Hz to emulate the addition and removal of the signal. This signal is centered at 1600 nm with 4.8 dBm of optical power when the signal is ON. The signal S_1 is centered at 1551 nm, with 1.4 dBm of optical power. The pump wavelengths and powers are the same as the ones described in Section 2.3.2. An optical filter is used to select the surviving channel wavelength, in this case, the signal S_1. A digital oscilloscope (OSC) is used to detect the power evolution of the surviving channel.

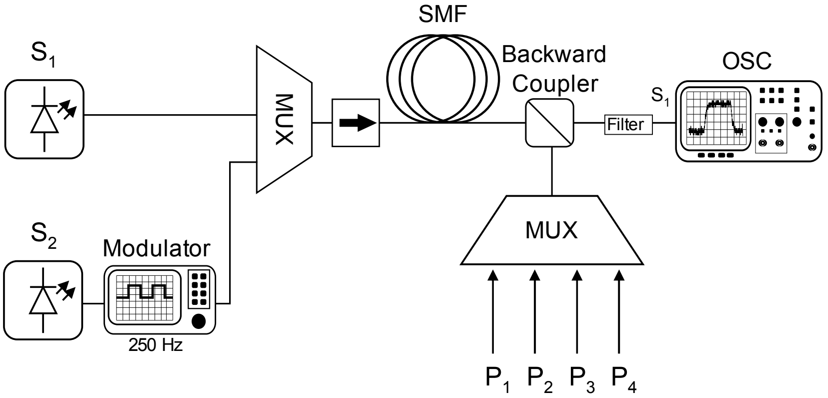

Figure 2.10: Experimental setup used to measure the transient effect of a counter–pumped RFA.

Figure. 2.11 shows the gain deviation of the surviving channel S_1 at the end of the amplifier, which is the difference between the time evolution of the optical power of the surviving channel and the optical power of the surviving channel on the steady state regime, when the signal S_2 is dropped and added. The results are obtained by experimental measurements and by numerical simulations. The removal of the 1600 nm signal occurs at 2 ms, which leads to an increase in power on the continuous signal after a delay of 193 μs, due to the signal propagation in the fiber. After the rising time, a new steady–state regime is obtained with only one signal, S_1, present in the system. At 4 ms the signal S_2 is turned ON and, after the propagation delay, we can observe that the continuous channel falls back to the initial optical power. As shown in Fig. 2.11, the transient response is accurately described by the simulation results.

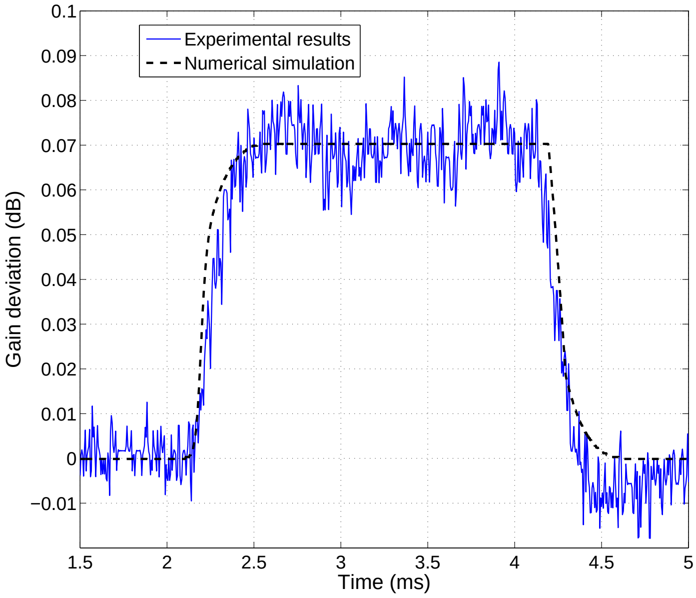

Figure 2.11: Gain deviation of the channel centered at 1551 nm as function of time when one channel is added/dropped: experimental (line) and simulation (dashed line) results.

2.4 Model for EDFAs

The inclusion of a dopant in a silica fiber, such as erbium (Er^{3+}), originates a local electric field called ligand field [2]. As a consequence, the Stark effect is induced and a splitting of the energy levels of the erbium ions occurs [53]. Each energy level has a total orbital momentum J that splits into a manifold of energy sublevels $g = J + 1/2$, where g is the total level degeneracy [2]. However, due to thermalization (Boltzmann distribution), the population distribution within the manifold is maintained constant, making possible to consider them as a single energy level [2].

Figure 2.12 shows a simplified diagram of Er^{3+} energy levels in silica glass. The ground level is the lowest energy level, E_1 ($^4I_{15/2}$). The second level, also known as the metastable level, E_2 ($^4I_{13/2}$), is quite stable and the average lifetime of an electron at this level is about 10 ms. The third and upper energy level, E_3 ($^4I_{11/2}$), is unstable and an electron pumped into this level will transit very quickly to the metastable level, E_2, without emitting any photon. This is known as a non–radioactive decay. It is also possible for an electron on the E_2 energy level to absorb energy from a pump photon and be excited to upper energy levels, and then decay to the E_3 level and after to the metastable energy level [2]. This effect is called excited–state absorption (ESA) and leads to a lower metastable population and, consequently, to a lower gain.

To achieve the population inversion, it is necessary to optically pump the doped

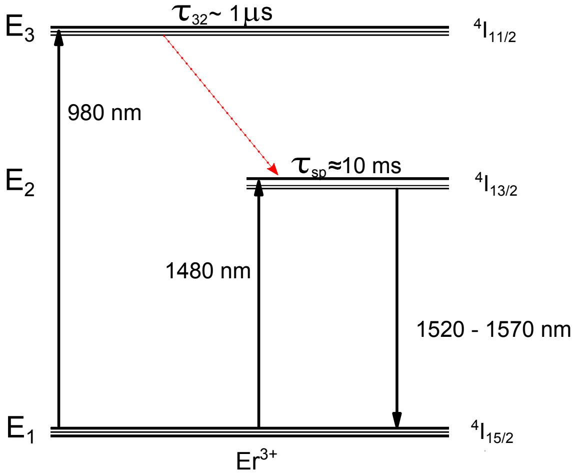

Figure 2.12: Energy level structure of Er^{3+} in glass fiber host. EDF can be pumped either at 980 nm or at 1480 nm.

fiber at a wavelength region corresponding to the energy level transitions. Fig. 2.13 shows the average Giles parameters for the emission, $\bar{\sigma}^e$, and absorption, $\bar{\sigma}^a$, as function of the signal wavelengths for the EDF MP980 produced by OFS [54]. At the typical pump wavelengths around 1480 nm, the Giles parameter for the absorption is higher than for the emission and, therefore, the pumping to the energy level E_2 will be efficient [53]. On the other hand, at the typical signal wavelengths, around 1550 nm, the emission parameter is higher than the absorption and, consequently, the signals will be amplified if pumping exists. The Stark splitting of E_1 and E_2 levels makes the signal emission band as broad as 40 nm, extending from 1525 nm to 1565 nm. Another region where the pumping of the EDFAs is efficient is around 980 nm. The high energy of the pumped photons allows the erbium ions in the ground state to be excited to the upper energy level, E_3, as shown in Fig. 2.12. The higher the population inversion, the lower the noise figure of the amplifier. Thus, 980 nm pumping wavelength is preferred to design low–noise amplifiers. Despite this, higher power lasers are available at 1480 nm and, therefore, 1480 nm pumps find applications in amplifiers designed to produce high gain. Another advantage of the 1480 nm pump is that its power can also propagate with low loss in silica fiber. The inversion level of a EDFA is mainly set by the pump power and wavelength. However, as the input signal power increases, or the pump power decreases, the inversion level will diminish. This effect is known as gain saturation, where as the input signal power increases, the amplifier saturates and cannot produce any more output power, reducing the gain of the amplifier. The saturation is also commonly known as gain compression.

The gain spectrum due to the Stark split of the energy levels can be considered to

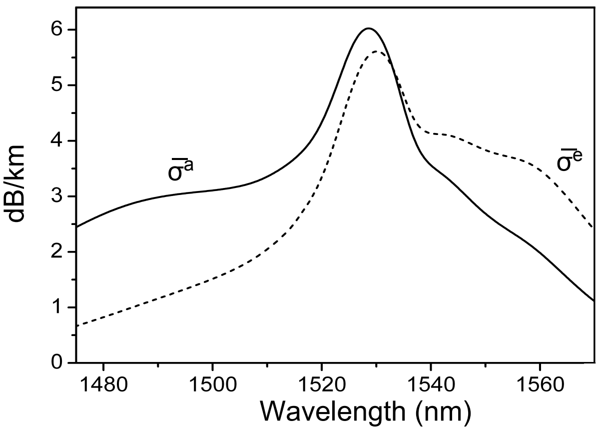

Figure 2.13: Giles parameters for the absorption and emission for the EDF MP980 [54] measured by the hosting company.

be homogeneously broadened [53, 55, 56]. This has been considered as a good approximation for both erbium–doped silica fibers and erbium–doped fluoride fibers at room temperature [53, 57, 58], and has been used in almost all the models of EDFAs [53]. However, when placed in a glass host, the spectra of erbium ions are influenced both by the silica and by any other dopant. This can result in inhomogeneous broadening contributions, which manifests as spectral hole burning (SHB) and site dependent pumping (SDP). Recent studies have shown that SHB and SDP effects are small, but might be important in specific wavelength regions for some applications [59, 60].

Several attempts have been made to describe SHB in EDFA theoretically and numerically. However, it is still not completely clear the physical interpretation of the effect. When considering the steady–state regime, the hole shape in EDFAs is not Lorentzian [60], like in a gas laser. This might suggest that there are additional or different mechanisms of SHB in EDFA, when compared with the mechanisms in gas lasers. In [57], SHB is assumed to be due to the wavelength shift of the emission and absorption spectrum for the different erbium ions. Other works, such as [61], include the mechanisms of the excitation transfer from one ion to another, assuming that the shapes of the individual ions are identical, but shifted in wavelength. Others suggest that there might be a strong dependence of the ion spectrum on the ion orientation [62]. In [63], the authors concluded that the most important contribution is due to the “standard” SHB mechanism, similar to the gas laser SHB. The hole in the gain spectrum is the result of differences in the spectral shapes of the different ions and these ions do not interact between them. According to [63], even for a high concentration of Er^{3+} ions in silica, the only mechanism that can be responsible for SHB is the “standard” SHB mechanism. One important consequence of this theory is the particular dependence of spectral hole burning depth on amplifier compression.

SHB was modeled and described for the steady–state regime in [63]. The two–level model incorporating SHB proposed in [63] is based on the assumption of statistical variations of the optical properties among ion sub–ensembles, leading to gain variation, at a given wavelength, induced by other signals. Mathematically, the gain variation induced by other signals at a given wavelength can be characterized by a correlation matrix between the signals. The authors use a technique called modified spectral subtraction to determine the correlation matrix and verified that the proposed model presents good accuracy when compared with experimental results. In [64], the authors extended the steady–state model to the dynamic regime for the two–level EDFA and obtained reasonable simulation results.

Another manifestation of the inhomogeneous gain broadening is the SDP effect. When considering the SDP effect, which is also named as “pump mediated inhomogeneity” [65], it is assumed that the erbium ions are in different “sites” within the glass matrix. The local electric field of these sites shifts the energy levels of the erbium ions, thus modifying the emission and absorption properties of the ions. The manifestation of the effect is the dependence of the gain spectral shape on the pump wavelength. In [66], the authors showed that the SDP effect is strongly affected by pump wavelengths around 980 nm and needs to be considered together with SHB, in order to develop a useful model for estimating the EDFA performance. Moreover, in [67], the authors measured the SDP spectrum for several pump wavelengths around 980 nm and concluded that the SDP effect has a maximum ripple of several decibels, with dependence on the amplifier compression. In the same study, the authors concluded that the SDP effect can be described in a similar way to SHB and proposed a method to determine the correlation matrix between the pumps and the signals. When considering pumps centered around 1480 nm, the SDP effect is assumed to be negligible by some authors [67].

In [68], the authors extended the model [64] to the third level. The validation of this approach is presented in [68, 69]. However, due to the fact that the authors mitigate the power transients with a gain control method, the results are not clear and some deviations between simulation and experimental results were not explained.

2.4.1 Two–level System Considering Statistical Variations

Having the advantages of low loss and not exhibiting ESA at the pump wavelength, the 1460–1500 nm pumping band is an appropriate bandwidth to pump the EDF. When considering these wavelengths, the highest difference between the absorption and emission of the erbium ion is centered close to 1480 nm and, thus, these amplifiers usually operate at 1480 nm. This fact allows us to consider a two–level model [24] for the EDFA.

We can describe the propagation of light in the EDF as a number of optical beams of frequency bandwidth $\Delta\nu_k$ centered at the optical wavelength $\lambda_k = c/\nu_k$, where k is the signal index. This notation describes both narrow line beams, such as pump and signal sources, when it is assumed that $\Delta\nu_k = 0$, and broadband ASE noise, where it is assumed that $\Delta\nu$ defines the frequency steps used in the simulation to resolve the ASE noise spectrum. Then, the integration over the optical frequency is approximated by a summation over k and the total number of wavelengths is N_{tot}.

Let us consider that an EDF is composed of several erbium ion sub–ensembles. For each ion sub–ensemble, i, we can define $\sigma^a_{k,i}$, and $\sigma^e_{k,i}$, which are the Giles parameters for absorption and emission, respectively, at a wavelength indexed by k. Considering no statistical variations of the optical properties of ion sub–ensembles, these parameters correspond to the average Giles parameters $\bar{\sigma^e}_k$ and $\bar{\sigma^a}_k$ for emission and absorption, respectively (see Fig. 2.13). Based on this assumption, the distribution of the photon flux $\bar{I_k}$ for the signals, pumps, ASE noise, and the population probability of the metastable level, $\bar{N_2}(z,t)$ in a two–level system, are described by the Giles model [53]

$$\frac{\partial \bar{I_k}}{\partial z} = \left\{ u_k(\bar{\sigma^a}_k + \bar{\sigma^e}_k)\bar{N_2} - \bar{\sigma^a}_k \right\} \bar{I_k} + u_k m \bar{\sigma^e}_k \bar{N_2} \Delta\nu_k/\zeta, \tag{2.20}$$

$$\frac{\partial \bar{N_2}}{\partial t} = -\bar{N_2} \sum_{k=1}^{N_{\text{tot}}} \bar{\sigma^e}_k \frac{\bar{I_k}}{\tau_2} + \left(1 - \bar{N_2}\right) \sum_{k=1}^{N_{\text{tot}}} \bar{\sigma^a}_k \frac{\bar{I_k}}{\tau_2} - \frac{\bar{N_2}}{\tau_2}, \tag{2.21}$$

where u_k indicates propagation direction, $+1$ for propagation in positive z–direction, and -1 for propagation on the negative z–direction, $\bar{I_k}(z,t) = p_k(z,t)/(h\nu_k\zeta)$ denotes the photon flux divided by the saturation parameter, ζ, and p_k denotes the optical power at wavelength k. N_{tot} is the total number of signals, ASE noise channels, and pump wavelengths propagating in the amplifier, ν_k is the frequency of the lightwave with the index k, τ_2 is the lifetime of the metastable level, m denotes the degrees of freedom (2, due to the 2 polarization directions), and $\Delta\nu_k$ is the effective noise bandwidth considered. For signals, this last parameter vanishes ($\Delta\nu_k = 0$).

The solutions to eqs. (2.20) and (2.21) are obtained by standard numerical integration techniques. If ASE noise is small and not included, then coupled propagation equations for the pump and signal beams are integrated with the noise source terms set to zero. Employing an effective noise bandwidth $\Delta\nu$, propagation equations for the forward and backward ASE noise can be added. Typical values of $\Delta\nu$ are 200–2000 GHz, depending on the fiber composition and operating conditions. This model was implemented by the hosting company and the simulation tool has been verified in a large series of measurements during the last years.

Now let us consider that the different ion sub–ensembles undergo a statistical variation of their optical properties. The statistical variation of emission and absorption spectra can be taken into account introducing a deviation function $\xi_{k,i}$, which is identical for both Giles parameters, due to the McCumber relation [2]. When introducing statistical variations of $\sigma^e_{k,i}$, $\sigma^a_{k,i}$ for a sub–ensemble i, we have [63]

$$\begin{aligned} \sigma^a_{k,i} &= \bar{\sigma^a}_k \left[1+\xi_{k,i}\right], & (2.22)\\ \sigma^e_{k,i} &= \bar{\sigma^e}_k \left[1+\xi_{k,i}\right]. & (2.23) \end{aligned}$$

In eq. (2.22) and (2.23) it is assumed that $\xi_{k,i} \ll 1$ and $\left\langle \xi_{k,i} \right\rangle = 0$, where the angular brackets stand for averaging over all erbium ions.

The statistical variations of the emission and absorption characteristics will create excited subpopulations with different population probabilities. Thus, the population probability $N_{2,i}$ of the metastable level, often called inversion, for a sub–ensemble is also a random variable and is given by

$$N_{2,i}(z,t) = \bar{N_2}(z,t) + \Delta N_{2,i}(z,t). \tag{2.24}$$

In eq. (2.24), $\bar{N_2}(z,t)$ is the average inversion of the EDFA for a given longitudinal section z and $\Delta N_{2,i}(z,t)$ denotes the variation of the population probability on the metastable level for a given ion sub–ensemble. The average value of the variation will be approximately zero, thus $\langle \Delta N_{2,i}(z,t) \rangle = 0$ [63].

Considering the statistical variations of the ion sub–ensemble, eq. (2.20) and eq. (2.21) can be written as

$$\frac{\partial I_{k,i}}{\partial z} = \left\{ u_k \left(\sigma^a_{k,i} + \sigma^e_{k,i} \right) N_{2,i} - \sigma^a_{k,i} \right\} I_{k,i} + u_k m \sigma^e_{k,i} N_{2,i} \Delta\nu_k / \zeta, \tag{2.25}$$

$$\frac{\partial N_{2,i}}{\partial t} = - N_{2,i} \sum_{k=1}^{N_{\mathrm{tot}}} \sigma^e_{k,i} \frac{I_{k,i}}{\tau_2} + (1 - N_{2,i}) \sum_{k=1}^{N_{\mathrm{tot}}} \sigma^a_{k,i} \frac{I_{k,i}}{\tau_2} - \frac{N_{2,i}}{\tau_2}. \tag{2.26}$$

To describe the distribution of signals, ASE noise and pump powers inside the EDF, we need to average the propagation and the population probability equations over all the ion sub–ensembles of the EDF. Thus we can write

$$\left\langle \frac{\partial I_{k,i}}{\partial z} \right\rangle_i = \left\langle \left\{ u_k \left(\sigma^a_{k,i} + \sigma^e_{k,i} \right) N_{2,i} - \sigma^a_{k,i} \right\} I_{k,i} + u_k m \sigma^e_{k,i} N_{2,i} \Delta\nu_k / \zeta \right\rangle_i, \tag{2.27}$$

$$\left\langle \frac{\partial N_{2,i}}{\partial t} \right\rangle_i = \left\langle - N_{2,i} \sum_{k=1}^{N_{\mathrm{tot}}} \sigma^e_{k,i} \frac{I_{k,i}}{\tau_2} + (1 - N_{2,i}) \sum_{k=1}^{N_{\mathrm{tot}}} \sigma^a_{k,i} \frac{I_{k,i}}{\tau_2} - \frac{N_{2,i}}{\tau_2} \right\rangle_i. \tag{2.28}$$

Introducing eqs. (2.22), (2.23), and (2.24) in eqs. (2.27) and (2.28), we obtain

$$\begin{aligned} \left\langle \frac{\partial I_{k,i}}{\partial z} \right\rangle_i = \; & \Bigg\langle \Bigg\{ u_k \left(\bar{\sigma}^a{}_k + \bar{\sigma}^e{}_k \right) \left(1 + \xi_{k,i} \right) (\bar{N}_2 + \Delta N_{2,i}) \\ & - \bar{\sigma}^a{}_k \left(1 + \xi_{k,i} \right) \Bigg\} I_{k,i} \\ & + u_k m \bar{\sigma}^e{}_k (1 + \xi_{k,i}) (\bar{N}_2 + \Delta N_{2,i}) \Delta\nu_k / \zeta \Bigg\rangle_i, \end{aligned} \tag{2.29}$$

$$\begin{aligned} \left\langle \frac{\partial \bar{N}_2 + \Delta N_{2,i}}{\partial t} \right\rangle_i = & \Bigg\langle - (\bar{N}_2 + \Delta N_{2,i}) \sum_{k=1}^{N_{\mathrm{tot}}} \bar{\sigma}^e \left(1 + \xi_{k,i} \right) \frac{I_{k,i}}{\tau_2} \\ & + \left(1 - \bar{N}_2 - \Delta N_{2,i} \right) \sum_{k=1}^{N_{\mathrm{tot}}} \bar{\sigma}^a \left(1 + \xi_{k,i} \right) \frac{I_{k,i}}{\tau_2} \\ & - \frac{\bar{N}_2 - \Delta N_{2,i}}{\tau_2} \Bigg\rangle_i. \end{aligned} \tag{2.30}$$

Performing the mathematical calculations, averaging over the entire set of erbium ion sub–ensembles, and applying $\left\langle \xi_{k,i} \right\rangle = 0$ and $\langle \Delta N_{2,i} \rangle = 0$, we obtain

$$
\begin{aligned}
\frac{\partial \bar{I}_k}{\partial z} &= u_k \Big\{ \left(\bar{\sigma}^a_k + \bar{\sigma}^e_k\right) \left(\bar{N}_2 + n_2^k\right) - \bar{\sigma}^a_k \Big\} \bar{I}_k + u_k m \bar{\sigma}^e_k (\bar{N}_2 + n_2^k) \Delta\nu_k / \zeta, && (2.31)\\
\tau_2 \frac{\partial \bar{N}_2}{\partial t} &= -\bar{N}_2 \Big(\sum_k^{N_{\text{tot}}} \bar{\sigma}^e_k \bar{I}_k + \sum_k^{N_{\text{tot}}} \bar{\sigma}^a_k \bar{I}_k + 1 \Big) + \sum_k^{N_{\text{tot}}} \bar{\sigma}^a_k \bar{I}_k - \sum_k^{N_{\text{tot}}} \left(\bar{\sigma}^a_k + \bar{\sigma}^e_k\right) n_2^k \bar{I}_k, && (2.32)
\end{aligned}
$$

where,

$$
n_2^k = \langle \Delta N_{2,i} \xi_{k,i} \rangle_i. \tag{2.33}
$$

From these calculations, a new mathematical entity arises, n_2^k, which accounts for the small variations of the population probability $\Delta N_{2,i}$ for a given wavelength. An equation for the time evolution of n_2^k can be derived by multiplying eq. (2.28) by $\xi_{k,i}$ and then averaging over all the ion sub–ensembles. Thus,

$$
\left\langle \xi_{k,i} \frac{\partial N_{2,i}}{\partial t} \right\rangle_i = \frac{\partial \langle \Delta N_{2,i} \xi_{k,i} \rangle_i}{\partial t} = \frac{\partial n_2^k}{\partial t}, \tag{2.34}
$$

which finally leads to

$$
\tau_2 \frac{\partial n_2^k}{\partial t} = -n_2^k \Big(\sum_{j=1}^{N_{\text{tot}}} \bar{\sigma}^e_j \bar{I}_j + \sum_{j=1}^{N_{\text{tot}}} \bar{\sigma}^a_j \bar{I}_j + 1 \Big) - \bar{N}_2 (A_k^* + B_k^*) - B_k^*), \tag{2.35}
$$

where the following quantities are defined

$$
\begin{aligned}
A_k^* &\equiv \sum_{j=1}^{N_{\text{tot}}} \bar{\sigma}^e_j \bar{I}_j \Gamma_s(k,j), && (2.36)\\
B_k^* &\equiv \sum_{j=1}^{N_{\text{tot}}} \bar{\sigma}^a_j \bar{I}_j \Gamma_s(k,j), && (2.37)\\
\Gamma_s(k,j) &= \left\langle \xi_{k,i} \xi_{j,i} \right\rangle_i. && (2.38)
\end{aligned}
$$

The term A_k^* accounts for the transitions starting from the metastable level, and the term B_k^* accounts for the transitions starting from the ground level, for all N_{tot} signals present in the system. These terms are weighted by a correlation factor, $\Gamma_s(k,j)$, for each term of the summation, where k and j are two wavelengths of N_{tot}. This factor depends on two input parameters and is represented by a matrix, named SHB correlation matrix.

Determination of the SHB Correlation Matrix

Although strongly desirable, there is currently no model available that allows the calculation of the correlation parameters from fundamental properties of the erbium ions. Nevertheless, the correlation matrix between the signals $\Gamma_s(k,j) = \langle \xi_k \xi_j \rangle$ can be obtained from experimental measurements, as shown in [63]. This technique is based on the subtraction of a measured ASE noise spectrum, which is approximately free of the SHB effect by using a signal placed at 1564 nm, from a ASE noise spectrum with a signal ranging from 1525 nm to 1560 nm. The signal is going to induce the SHB effects in the ASE noise spectrum around the signal wavelength.

Therefore, to construct the correlation matrix, a reference ASE noise spectrum approximately free of non–local SHB is generated by a signal channel at 1566 nm with a pump wavelength centered at 1480 nm. Subsequently, a signal wavelength ranging from 1525 nm to 1564 nm (2 nm steps) is injected in the amplifier and the signal power is adjusted in such a way that compression of the ASE noise spectrum is identical to the reference ASE noise spectrum. The difference between the spectra is going to reflect the change of inversion of correlated ion sub–ensembles due to SHB. Thus, the correlation matrix $\Gamma_s(k,j)$ is obtained by minimizing the difference between simulation and experimental results.

Figure 2.14 shows the SHB correlation matrix, $\Gamma_s(k,j)$, obtained by the hosting company. From the results presented we verify that the SHB effect has a higher impact in wavelengths from 1528 nm to 1533 nm. This means that when a signal centered around 1530 nm is injected in the amplifier, the gain of the other wavelengths around 1530 nm is going to diminish and a hole in the gain appears, thus the name “hole burning”. On the other hand, wavelengths above 1560 nm present a small impact on the remaining wavelengths.

2.4.2 Three–level System Considering Statistical Variations

When pumped at 980 nm, the erbium ion is excited from the ground state $^4\mathrm{I}_{15/2}$ to the $^4\mathrm{I}_{11/2}$ manifold, where there is a fast non–radiative decay to the level $^4\mathrm{I}_{13/2}$. Due to this process, high inversion levels can be achieved. Thus, when pumping around 980 nm, it is possible to achieve an increase of gain and a lower noise figure when compared with the amplifier pumped around 1480 nm [2]. However, the attenuation at the pump wavelength and the ESA effect bring some disadvantages to the 980 nm pump-

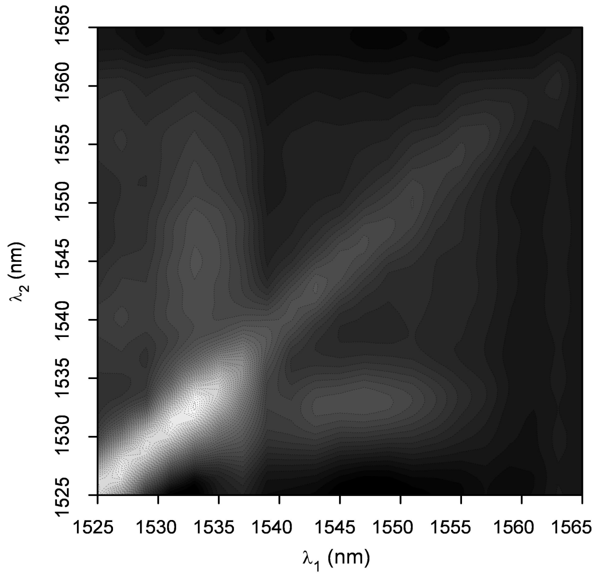

Figure 2.14: Correlation matrix between signals, $\Gamma_s(j,k)$. Max(white) = 0.304 and min(black) = -0.037.

ing scheme. When pumping around 980 nm to perform detail numerical simulations a three-level system model should be considered for the EDFA.

To model the three–level system, let us assume that there are a total of M lightwaves involved in direct ion transitions from the ground level to the metastable energy level and vice–versa. These wavelengths are found in the conventional wavelength band (C–band) and around 1480 nm. Pumps around 980 nm need to be taken into account in a different way and they are represented by the index l. The three–level system is derived from the two–level model [53], extended for the three–level according to [2], having in consideration the ESA effect. In this assumption, the distribution of the photon flux $\bar{I}_k$ for the signals, pumps, amplified ASE noise and the population probability of the metastable level, $\bar{N}_2(z,t)$, is given by

$$\frac{\partial \bar{I}_k}{\partial z} = \left\{ u_k(\bar{\sigma^a}_k + \bar{\sigma^e}_k)\bar{N}_2 - \bar{\sigma^a}_k(1-\bar{N}_3) \right\} \bar{I}_k + u_k m \bar{\sigma^e}_k \bar{N}_2 \Delta\nu_k/\zeta, \tag{2.39}$$

$$\frac{\partial \bar{I}_l^{980}}{\partial z} = \left\{ u_k \bar{\sigma^a}_l(1-\bar{N}_2-\bar{N}_3) + u_k \bar{\sigma}_l^{\mathrm{ESA}} \bar{N}_3 \right\} \bar{I}_l^{980}, \tag{2.40}$$

$$\frac{\partial \bar{N_2}}{\partial t} = -\bar{N_2}\sum_{k=1}^{M}\bar{\sigma^e}_k\frac{\bar{I_k}}{\tau_2} + \left(1-\bar{N_2}-\bar{N_3}\right)\sum_{k=1}^{M}\bar{\sigma^a}_k\frac{\bar{I_k}}{\tau_2} - \frac{\bar{N_2}}{\tau_2}+\frac{\bar{N_3}}{\tau_3}, \tag{2.41}$$

$$\frac{\partial \bar{N_3}}{\partial t} = \left(1-\bar{N_2}-\bar{N_3}\right)\sum_{l=1}^{M^{980}}\bar{\sigma^a}_l\frac{\bar{I}_l^{980}}{\tau_2} - \frac{\bar{N_3}}{\tau_3}. \tag{2.42}$$

where $\bar{I}_l^{980}$ is the photon flux of the pump centered at 980 nm divided by the saturation parameter, ζ, $\bar{\sigma}^{\mathrm{ESA}}$ is the ESA absorption, $\bar{N_3}$ is the average population probability of the third level and τ_3 is the lifetime of the third level given in [70]. This model was implemented and validated by the hosting company [71].

Again, let us consider the statistical variations of eqs. (2.22) and (2.23). The statistical variations of the emission and absorption spectra will create excited sub-populations with different population probabilities in the third energy level. Thus, the population probabilities for the sub–ensembles, $N_{3,i}$, are also random variables. As a result, we have [68]

$$N_{3,i}(z,t) \;=\; \bar{N_3}(z,t) + \Delta N_{3,i}(z,t). \tag{2.43}$$

In eq. (2.43), $\bar{N_3}(z,t)$ refers to the average inversion of the EDFA for a given longitudinal section z and $\Delta N_{3,i}(z,t)$ denotes the variation of the population probability on the metastable level for a given ion sub–ensemble. The average value of the variation will be approximately zero, thus $\langle \Delta N_{3,i}(z,t)\rangle = 0$ [68].

Introducing eqs. (2.22), (2.23), (2.24), and (2.43) in eqs. (2.39), (2.40), (2.41), and (2.42), averaging over the entire set of erbium ion sub–ensembles, and applying $\left\langle \xi_{k,i}\right\rangle = 0$, $\langle \Delta N_{2,i}\rangle = 0$ and $\langle \Delta N_{3,i}\rangle = 0$, the propagations of the photon flux for the signals, pumps around 980 nm, and ASE noise are given by

$$\begin{aligned}\frac{\partial \bar{I_k}}{\partial z} =& u_k[(\bar{\sigma^a}_k+\bar{\sigma^e}_k)(\bar{N_2}+n_2^k) - \bar{\sigma^a}(1-\bar{N_3}-n_3^l)]\bar{I_k} \qquad (2.44)\\ &+ u_k m\bar{\sigma^e}(\bar{N_2}+n_2^k)\Delta\nu_k/\zeta,\\ \frac{\partial \bar{I}_l^{980}}{\partial z} =& -[\bar{\sigma^a}_l(1-\bar{N_2}-n_2^l-\bar{N_3}+n_3^l)+\bar{\sigma^a}_l^{ESA}(\bar{N_3}-n_3^l)]\bar{I}_l^{980}. \qquad (2.45)\end{aligned}$$

where:

$$n_2^k = \langle \Delta N_2 \xi_k \rangle,$$
$$n_3^l = \langle \Delta N_3 \xi_l \rangle.$$

The rate equations and variations of the system are given by

$$\frac{\partial \bar{N}_2}{\partial t} = -\bar{N}_2\left(A+B+\frac{1}{\tau_2}\right) - \bar{N}_3\left(B-\frac{1}{\tau_3}\right) + B - \alpha - \gamma, \tag{2.46}$$

$$\frac{\partial \bar{N}_3}{\partial t} = -\bar{N}_3\left(C+\frac{1}{\tau_3}\right) + C(1-\bar{N}_2) - \delta - \beta, \tag{2.47}$$

$$\frac{\partial n_2^j}{\partial t} = -n_2^j\left(A+B\frac{1}{\tau_2}\right) - n_3^j\left(B-\frac{1}{\tau_3}\right) - \bar{N}_2(A_j^* + B_j^*) - (1-\bar{N}_3)B_j^*, \tag{2.48}$$

$$\frac{\partial n_3^j}{\partial t} = -(n_2^j + n_3^j)C + \frac{n_3}{\tau_3} + (1-\bar{N}_2-\bar{N}_3)C_j^*, \tag{2.49}$$

where,

$$A \equiv \sum_{k=1}^{M} \bar{\sigma}^{e}{}_{k}\frac{\bar{I}_k}{\tau_2},\ B \equiv \sum_{k=1}^{M} \bar{\sigma}^{a}{}_{k}\frac{\bar{I}_k}{\tau_2},\ C \equiv \sum_{l=1}^{M^{980}} \bar{\sigma}^{a}{}_{l}\frac{\bar{I}_l^{980}}{\tau_2}, \tag{2.50}$$

$$A_j^* \equiv \sum_{k=1}^{M} \bar{\sigma}^{e}{}_{k}\frac{\bar{I}_k}{\tau_2}\Gamma_s(j,k),\ B_j^* \equiv \sum_{k=1}^{M} \bar{\sigma}^{a}{}_{k}\frac{\bar{I}_k}{\tau_2}\Gamma_s(j,k),\ C_j^* \equiv \sum_{l=1}^{M^{980}} \bar{\sigma}^{a}{}_{l}\frac{\bar{I}_l^{980}}{\tau_2}\Gamma_{9xx}(j,l), \tag{2.51}$$

$$\alpha \equiv \sum_{k=1}^{M} \left(\bar{\sigma}^{a}{}_{k} + \bar{\sigma}^{e}{}_{k}\right) n_2^k \frac{\bar{I}_k}{\tau_2},\ \gamma \equiv \sum_{k=1}^{M} \bar{\sigma}^{a}{}_{k} n_3^k \frac{\bar{I}_k}{\tau_2}, \tag{2.52}$$

$$\beta \equiv \sum_{l=1}^{M^{980}} \bar{\sigma}^{a}{}_{l} n_3^l \frac{\bar{I}_l^{980}}{\tau_2},\ \delta \equiv \sum_{l=1}^{M^{980}} \bar{\sigma}^{a}{}_{l} n_2^l \frac{\bar{I}_l^{980}}{\tau_2}. \tag{2.53}$$

According to [67, 68], the completion of this model requires the measurement of two correlation matrices: one for SHB, $\Gamma_s(j,k)$, which was constructed and presented in Section 2.4.1, and a second correlation matrix for the SDP effect, $\Gamma_{9xx}(l,j) = \langle \xi_l \xi_j \rangle$, which can be measured according to [67].

Determination of the SDP Correlation Matrix

According to the literature, the correlation matrix between the pump wavelengths around 980 nm and the signals, $\Gamma_{9xx}(l,j)$, can be determined by a technique presented in [67]. This technique is based on the subtraction of an ASE noise spectrum of the pumps around 980 nm with a reference ASE noise spectrum, obtained with a 1480 nm pump. However, the ASE noise generation is different for the two and three–levels EDFA. Therefore, the authors corrected this difference numerically. From the subtraction between these two spectra and by correcting the ASE noise generation, the authors obtained the SDP spectrum for a given pump around 980 nm. From the obtained SDP spectrum for each pump around 980 nm it is possible to construct the correlation matrix between pump and signals [67]. This approach is possible if it is considered that the 1480 nm has a negligible SDP effect [67] and can be used as a reference ASE noise spectrum.

In our proposed approach [6], we use a different procedure, in order to overcome the differences in the ASE noise generation between 980 nm and 1480 nm. We measure the ASE noise profile for the pumps around 980 nm and then subtract the reference ASE noise spectrum obtained with the numerical model implemented for the three–level system considering only the SHB effect. This model already describes correctly the ASE noise generation for the three–level. Therefore, the difference between the experimental measurements and the numerical model gives us the SDP spectrum for each pump around 980 nm. Using this approach, we simplify the technique presented [67], and the assumption that the 1480 nm pump has a negligible SDP effect does not need to be considered.

To determine the correlation matrix between the pump wavelengths and the signals, first we measure the ASE noise spectrum for pump wavelengths around 980 nm. Fig. 2.15 shows the schematic diagram of the experimental setup. The reference signal is co–propagated with a pump around 980 nm, and injected in a 10 m EDF. The reference signal is used to control the amplifier gain and is centered at 1564 nm. This wavelength is chosen because it has a small SHB [63], allowing us to measure just the SDP effect. The pumps used are centered around 980 nm, 976 nm, and 974 nm. The reference signal has -10 dBm of input signal power and the pump centered at 980 nm has 10 mW of input pump power. When changing the pump wavelength, the input pump power is adjusted to maintain the same gain for the reference channel.

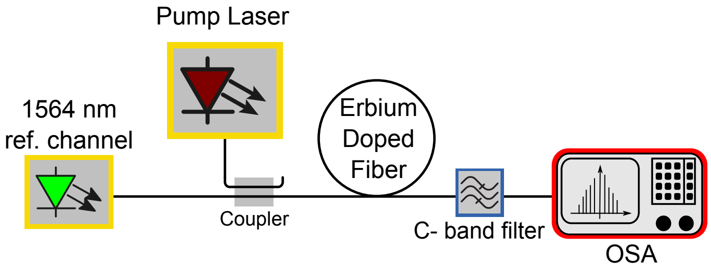

Figure 2.15: Schematic diagram of the experimental setup used to measure the ASE noise profile for different pump wavelengths and powers.

Figure 2.16 shows the subtraction of the measured ASE noise spectrum to the simulated ASE noise spectrum, for pumps centered at 980 nm, 976 nm, and 974 nm, and maintaining the same gain for the reference signal. As shown, different pump wavelengths present different spectra, with different maximum ripples and peak locations. The maximum ripple obtained is for the 980 nm pump, close to 5 dB, and the lower for the 974 nm pump, 3.8 dB. Considering the peak location, we verify that the 976 nm pump has the peak located near 1528 nm and the 980 nm pump close to 1532.5 nm. As the results show, for the same amplifier gain, the maximum ripple can have a variation above 1 dB and a peak location difference of more than 4 nm, depending on the pump considered. These results are consistent with [67].

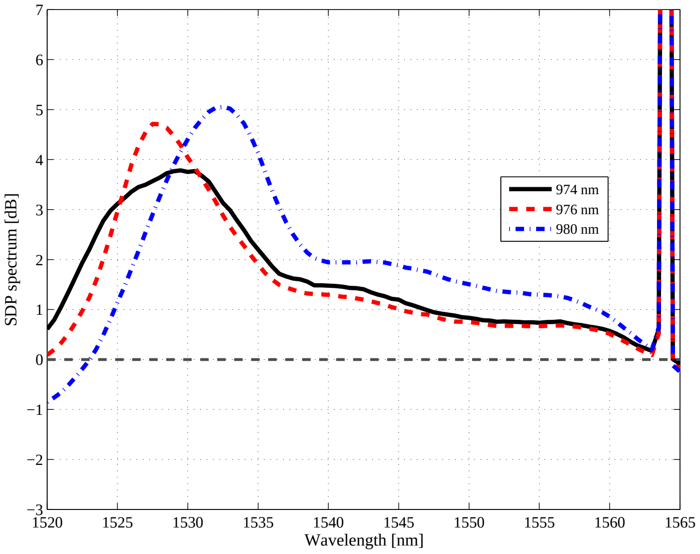

Figure 2.16: SDP spectrum of different pump wavelengths with the same gain for the reference signal, considering a spectral resolution of 0.05 nm.

The SDP spectrum is determined by the difference between the experimental ASE noise spectrum for each pump and the simulation with the SHB effect already considered. Thus, to determine the correlation matrix, we perform iterative guesses on the each pump, in order to minimize the difference between the simulation model with SHB and SDP and experimental results. By repeating this process for the different pump wavelengths considered, it is possible to determine the correlation matrix between the pump wavelengths and the signal wavelengths.

Figure 2.17 shows the correlation matrix for the SDP effect between the pump wavelengths from 974 nm to 980 nm and the signals between 1520 nm and 1565 nm. The minimum value of this matrix is 0.004 and the maximum is 0.15.

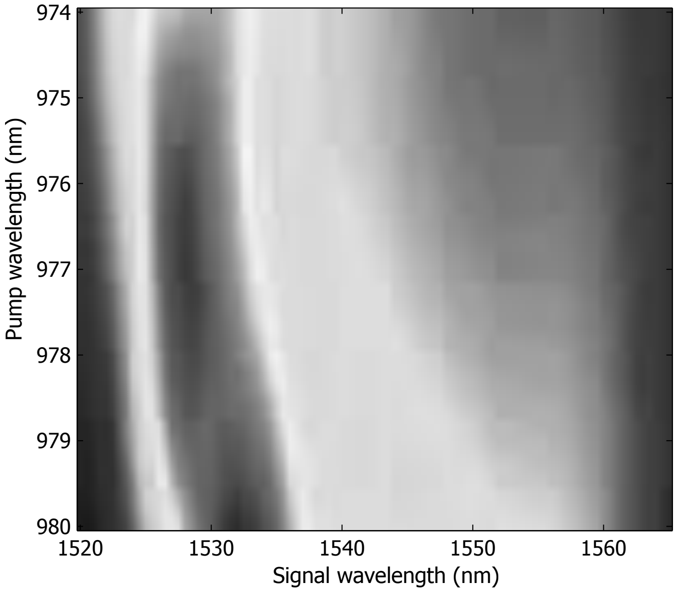

Figure 2.17: SDP correlation matrix, $\Gamma_{9xx}(l,j)$, between pump wavelengths and signal wavelengths. The $\Gamma_{9xx}(l,j)$ comprises values in between 0.004 (white) and the maximum 0.15 (black).

After constructing the correlation matrix between the pumps and the signals, the three–level model considering statistical variations of the Giles parameters is concluded.

Experimental Validation

Typically, to experimentally measure the dynamic response due to SHB and SDP, it is necessary to control and mitigate the power transients created by input channel power variation [68]. However, the control system that is added to the EDFA can be a source of inaccuracies [68]. To overcome this, we propose a setup similar to the one presented in [72], which allows us to measure the SHB and SDP behavior without the contribution of other dynamic effects [6].

To verify the model and assess the dynamic response of the EDFA due to SHB and

SDP, we implement the experimental setup presented in Fig. 2.18. In this setup, the surviving channel is tuned to 1531.2 nm, i. e. the region where the gain deviations due to SHB and SDP are maximized [63]. Multiplexed with a pump tunable from 974 nm to 980 nm, the surviving channel is launched into a 10 m EDF. Ten additional channels are added to the setup and, depending on the position of a fast 2x1 switch with switching time below 1 μs, they can be located either on the blue side (blue subband) or on the red side (red subband) of the C–band. The total power of the ten channels located on the red subband is adjusted in such a way that the surviving channel experiences equal gain independently of the switch position on steady–state conditions. At the output of the amplifier, a filter is used to separate the surviving channel from the other channels and the pump (suppression $>$ 40 dB). The time evolution of the optical power of the surviving channel is recorded with a digital oscilloscope (OSC).

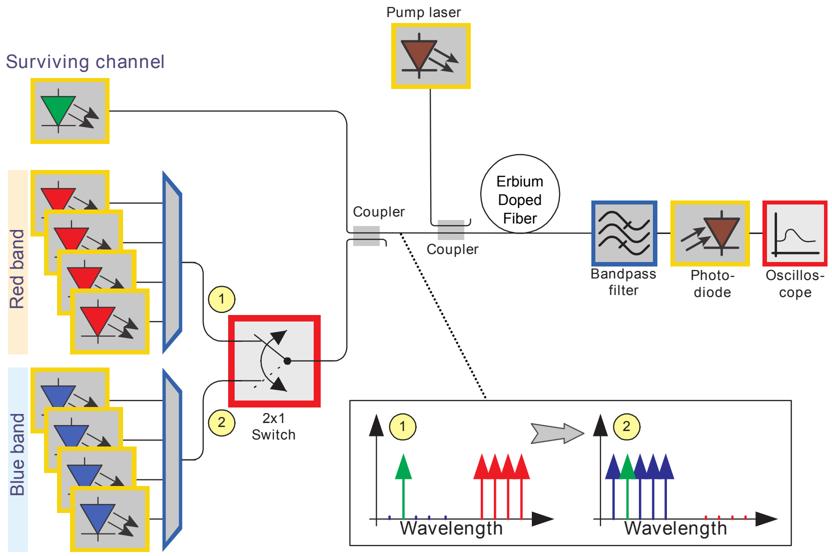

Figure 2.18: Schematic diagram of the experimental setup implemented to measure the dynamic response of the EDFA.

To verify the model, we measure the power excursion of the surviving channel, which is the difference between the time evolution of the optical power of the surviving channel and the optical power of the surviving channel on the steady state regime. We use pumps centered at 980 nm, 976 nm, and 974 nm. The blue subband channels have an equal channel spacing of 100 GHz start at 1529.6 nm, with the channel close to 1531.2 nm being skipped. On the red subband there are ten channels with 100 GHz of channel spacing and the first channel centered at 1556.7 nm. The surviving channel and the blue subband channels have an input signal power around -9.3 dBm/channel. The dynamic response of the amplifier is measured when switching from the red subband to the blue subband, and vice–versa.

Figure 2.19(a) shows the power excursion of the surviving channel at the output of the EDFA for gain values close to 0 dB. This small gain value is chosen in order to get a large compression, which allows to measure both SHB and SDP with high sensitivity [73]. For the pumps centered at 980 nm, 976 nm, and 974 nm, the results show a maximum power excursion of about -0.40 dB, -0.33 dB, and -0.30 dB respectively. Therefore, when the pump is centered at 974 nm or 976 nm, the deviations are between 23% and 20% smaller than when compared with the pump centered at 980 nm. A good agreement between the simulation result and experimental data is observed, both in terms of maximum deviation and in transition time, confirming the accuracy of the proposed simulation model.

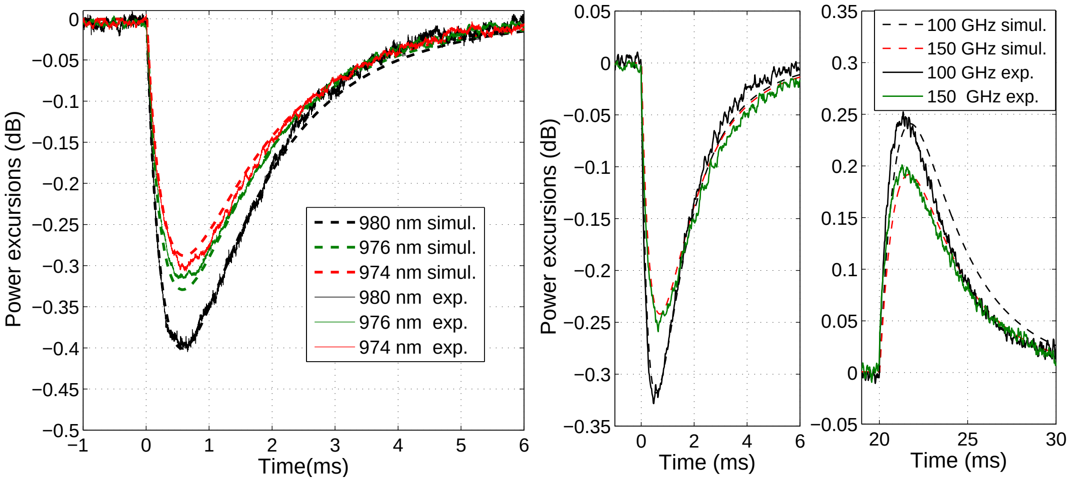

(a) (b)

Figure 2.19: a) Power excursions of the surviving channel for different pump wavelengths, when switching from the red subband to the blue subband; b) Power excursions for the surviving channel for an EDFA pumped at 976 nm with different input channel spacing, when switching from the red to the blue subband (on the left) and from the blue to the red subband (on the right).

We can use the setup to further investigate the SHB and SDP dependence on the input channel spectra allocation. We measure the amplifier dynamic response for an input signal spectrum with a channel spacing of 100 GHz and 150 GHz. We start by measuring the dynamic response for an EDF pumped at 976 nm with a gain close to zero and using a channel spacing of 100 GHz. Since changing the spectral location of the channels influences the amplifier gain, the total input signal power of the blue subband on the measurement with 150 GHz is readjusted, in order to provide the same gain for the surviving channel. Fig. 2.19(b) shows the power excursions of the surviving channel when switching from the red subband to the blue subband (on the left), and when switching from the blue subband to the red subband (on the right). As we can see, the power excursions increase by 20% when changing the channel spacing from 150 GHz to 100 GHz. Moreover, there is a good agreement between simulation and experimental data, therefore confirming the accuracy of the simulation model.

2.5 Conclusions

In this chapter, the principal characteristics of the RFAs and EDFAs were presented and discussed. An overview regarding the typical amplifier configurations used to extend the reach of the optical transmission link was also highlighted.

The physical principle of RFA was introduced, as well as the propagation equations. Furthermore, we presented and implemented the APA for the steady–state and for the dynamic regime. We experimentally validated the numerical model in the steady–state and in the dynamic regime, and verified that the implemented model has good accuracy.

Regarding the EDFA, we discussed the physical principle of the two–level and three–level system, focusing on the inhomogeneous gain broadening effect, which manifests as the SHB and SDP effects. We derived and implemented the model for the two–level EDFA and three–level EDFA considering the statistical variation of the Giles parameters. Two correlation matrices were determined based on experimental results in order to be possible to implement the model.

Using a proposed experimental setup specifically designed to isolate the SHB and SDP effects, we were able to validate the mathematical model for the three–level amplifier. Finally, we investigated the dependence of the dynamic response of the EDFA attributable to SHB and SDP on spectral allocation of input channels for three–level EDFAs. We concluded that, by selecting a pump wavelength centered at 974 nm instead of 980 nm, we could reduce the power excursions by 23 %, and that, by increasing the channel spacing from 100 GHz to 150 GHz, the power excursions decreased by more than 20 %.

References

[1] C. Headley and G. Agrawal, *Raman amplification in fiber optical communication systems.* Academic press, 2005.

[2] E. Desurvire, *Erbium-doped fiber amplifiers: principles and applications.* Wiley, 1994.

[3] D. Menashe, A. Shlifer, and U. Ghera, "Optical amplifiers for modern networks," in *Proc. International Conference on Transparent Optical Networks (ICTON)*, Jun. 2006, pp. 115 – 118.

[4] J. Ferreira, M. Fugihara, and A. Pinto, "Transient response and control of pump-reflecting Raman fiber amplifiers," *Fiber and Integrated Optics*, vol. 29, no. 1, pp. 44–61, Dec. 2009.

[5] J. Ferreira, R. Nogueira, P. Monteiro, and A. Pinto, "Weighted undepleted pump model for broadband counter-pumped Raman fiber amplifiers," *IEEE/OSA Journal of Optical Communications and Networking*, vol. 4, no. 8, pp. 595–602, Aug. 2012.

[6] J. Ferreira, D. Fonseca, P. Monteiro, and L. Rapp, "Dynamics of SHB and SDP on 9XX EDFAs: dependence on spectral allocation of input channels," in *Proc. International Conference on Transparent Optical Networks (ICTON)*, Jun. 2013, p. Th.A2.3.

[7] J. Bromage, "Raman amplification for fiber communications systems," *IEEE/OSA Journal of Lightwave Technology*, vol. 22, no. 1, pp. 79–93, Jan. 2004.

[8] S. Namiki, N. Tsukiji, and S. Shikii, "Challenges of Raman amplification," *Proceedings of the IEEE*, vol. 94, no. 5, pp. 1024–1035, May 2006.

[9] M. Islam, "Raman amplifiers for telecommunications," *IEEE Journal of Selected Topics in Quantum Electronics*, vol. 8, no. 3, pp. 548–559, May 2002.

[10] J. Cai, D. Foursa, and A. Lucero, "Long-haul 40 Gb/s RZ-DPSK transmission over 4,450 km with 150 km repeater spacing using Raman assisted EDFAs," in *Proc. Optical Fiber Communication Conference (OFC)*, Mar. 2007, p. OWM3.

[11] P. André, "Measurement of Raman gain coefficient in standard single-mode optical fibers for DWDM photonic simulation purposes," in *Proc. SPIE 5036, Photonics, Devices, and Systems II*, Jul. 2003, pp. 518–522.

[12] H. Kidorf, K. Rottwitt, M. Nissov, M. Ma, and E. Rabarijaona, "Pump interactions in a 100 nm bandwidth Raman amplifier," *IEEE Photonics Technology Letters*, vol. 11, no. 2, pp. 530–532, May 1999.

[13] T. Naito, T. Tanaka, and K. Torii, "A broadband distributed Raman amplifier for bandwidths beyond 100 nm," in *Proc. Optical Fiber Communication Conference (OFC)*, Mar. 2002, p. TuR1.

[14] C. Fludger, "Pump to signal RIN transfer in Raman fiber amplifiers," *IEEE/OSA Journal of Lightwave Technology*, vol. 19, no. 8, pp. 1140–1148, Aug. 2001.

[15] E. Taylor, L. Ng, and J. Nilsson, “Thulium-doped tellurite fiber amplifier,” *IEEE Photonics Technology Letters*, vol. 16, no. 3, pp. 777–779, Mar. 2004.

[16] S. Aozasa, H. Masuda, and M. Shimizu, “S-band thulium-doped fiber amplifier employing high thulium concentration doping technique,” *IEEE/OSA Journal of Lightwave Technology*, vol. 24, no. 10, pp. 3842–3848, Oct. 2006.

[17] R. Mears, L. Reekie, I. Jauncey, and D. Payne, “Low-noise erbium-doped fibre amplifier operating at 1.54 μm,” *IET Electronics Letters*, vol. 23, no. 19, pp. 1026–1028, Sep. 1987.

[18] M. Yamada, H. Ono, and T. Kanamori, “Broadband and gain-flattened amplifier composed of a 1.55 μm-band and a 1.58 μm-band Er3+ doped fibre amplifier in a parallel configuration,” *IET Electronics Letters*, vol. 33, no. 8, pp. 710–711, Apr. 1997.

[19] P. Wysocki, J. Judkins, R. Espindola, M. Andrejco, and A. Vengsarkar, “Broad-band erbium-doped fiber amplifier flattened beyond 40 nm using long-period grating filter,” *IEEE Photonics Technology Letters*, vol. 9, no. 10, pp. 1343–1345, Oct. 1997.

[20] M. Yamada, A. Mori, and K. Kobayashi, “Gain-flattened tellurite-based EDFA with a flat amplification bandwidth of 76 nm,” *IEEE Photonics Technology Letters*, vol. 10, no. 9, pp. 1244–1246, Sep. 1998.

[21] T. Kucukarslan and N. Unverdi, “Gain analysis of erbium and ytterbium-doped optical fiber amplifiers,” in *Proc. Signal Processing and Communications Applications Conference (SIU)*, Apr. 2012, pp. 1–3.

[22] R. Paschotta, J. Nilsson, A. Tropper, and D. Hanna, “Ytterbium-doped fiber amplifiers,” *IEEE Journal of Quantum Electronics*, vol. 33, no. 7, pp. 1049–1056, Jul. 1997.

[23] C. Hung, N. Chen, Y. Lai, and S. Chi, “High-gain low-noise tunable EDFA over S- and C+L-bands with double-pass configuration,” in *Proc. Conference on Lasers and Electro-Optics/Pacific Rim (CLEOPR)*, Aug. 2007, p. THD2.

[24] M. Yucel and H. Goktas, “Gain flattening configurations at the L-band erbium-doped fiber amplifiers,” in *Proc. Signal Processing and Communications Applications Conference (SIU)*, Jun. 2007, pp. 1–4.

[25] G. Charlet and J. Renaudier, “Transmission of 16.4 bit/s capacity over 2550 km using PDM QPSK modulation format and coherent receiver,” *IEEE/OSA Journal of Lightwave Technology*, vol. 27, no. 3, pp. 153–157, Feb. 2009.

[26] S. Pachnicke, N. Luck, and P. Krummrich, “Novel physical-layer impairment-aware routing algorithm for translucent optical networks with 43 Gb/s and 107 Gb/s channels,” in *Proc. International Conference on Transparent Optical Networks (ICTON)*, Jun. 2009, p. Tu.A3.6.

[27] A. Morea, F. Leplingard, and T. Zami, “New transmission systems enabling transparent network perspectives,” *Comptes Rendus Physique*, vol. 9, no. 9, pp. 985–1001, Nov. 2008.

[28] K. Sato, “Optical technologies that enable green networks,” in *Proc. International Conference on Transparent Optical Networks (ICTON)*, Jun. 2010, p. Mo.A.2.

[29] R. Tucker, “Green optical communications part II: energy limitations in networks,” *IEEE Journal of Selected Topics in Quantum Electronics*, vol. 17, no. 2, pp. 261–274, Mar. 2011.

[30] G. Ellinas and J. Labourdette, “Network control and management challenges in opaque networks utilizing transparent optical switches,” *IEEE Communications Magazine*, vol. 42, no. 2, pp. 16–24, Feb. 2004.

[31] Y. Emori, Y. Akasaka, and S. Namiki, “Broadband lossless DCF using Raman amplification pumped by multichannel WDM laser diodes,” *IET Electronics Letters*, vol. 34, no. 22, pp. 2145–2146, Oct. 1998.

[32] E. Desurvire, “Capacity demand and technology challenges for lightwave systems in the next two decades,” *IEEE/OSA Journal of Lightwave Technology*, vol. 24, no. 12, pp. 4697–4710, Dec. 2006.

[33] B. Heens and X. Wang, “Improvement of the EDFA design for both preamplifier and booster applications,” in *Proc. Electrotechnical Conference*, May 1998, pp. 1404 – 1408.

[34] G. Agrawal, *Nonlinear fiber optics.* Springer, 2000.

[35] S. Namiki and Y. Emori, “Ultrabroad-band Raman amplifiers pumped and gain-equalized by wavelength-division-multiplexed high-power laser diodes,” *IEEE Journal of Selected Topics in Quantum Electronics*, vol. 7, no. 1, pp. 3–16, Jan. 2001.

[36] C. Fludger and V. Handerek, “Ultra-wide bandwidth Raman amplifiers,” in *Proc. Optical Fiber Communication Conference (OFC)*, vol. 13, Mar. 2002, p. TuJ3.

[37] S. Faralli, G. Bolognini, and F. Pasquale, “Design optimization of high power and low RIN lasers for efficient Raman co-pumping,” in *Proc. Optical Fiber Communication Conference (OFC)*, Mar. 2007, p. JThA13.

[38] S. Faralli, G. Bolognini, M. Andrade, and F. Di Pasquale, “Unrepeated WDM transmission systems based on advanced first-order and higher order Raman-copumping technologies,” *IEEE/OSA Journal of Lightwave Technology*, vol. 25, no. 11, pp. 3519–3527, Nov. 2007.

[39] L. Wang, B. Hwang, and L. Yang, “Gain transients in copumped and counterpumped Raman amplifiers,” *IEEE Photonics Technology Letters*, vol. 15, no. 5, pp. 664–666, May 2003.

[40] S. Kado, Y. Emori, and S. Namiki, “Broadband flat-noise Raman amplifier using low-noise bidirectionally pumping sources,” *Optics communications*, pp. 38–39, Sep. 2001.

[41] M. Karásek, J. Kanka, L. Boháč, D. Krcmarik, J. Radil, and J. Vojtěch, “Surviving channel power transients in second-order pumped lumped Raman fiber amplifier: experimentation and modeling,” *IEEE/OSA Journal of Lightwave Technology*, vol. 25, no. 3, pp. 664–672, Mar. 2007.

[42] S. Milo, R. Souza, and M. Silva, “An EDFA theoretical analysis considering different configurations and pumping wavelengths,” in *Proc. International Microwave and Optoelectronics Conference (IMOC)*, Sep. 2003, pp. 105–110.

[43] H. Kawakami, “Suppression of the cross-gain modulation in remotely-pumped EDF/DRA hybrid inline amplifier systems with online otdr for gain monitoring,” *IEICE Transactions on Communications*, vol. E88-B, no. 5, pp. 1986–1993, May 2005.

[44] M. Karásek and M. Menif, “Protection of surviving channels in pump-controlled gain-locked Raman fibre amplifier,” *Optics Communications*, vol. 210, no. 1, pp. 57–65, Sep. 2002.

[45] X. Liu and B. Lee, “Effective shooting algorithm and its application to fiber amplifiers,” *OSA Optics Express*, vol. 11, no. 12, pp. 1452–1461, Jun. 2003.

[46] M. Karásek and J. Kanka, “Time-domain simulation of power transients in Raman fibre amplifiers,” *Wiley International Journal of Numerical Modelling: Electronic Networks, Devices and Fields*, vol. 17, no. 2, pp. 165–176, Mar. 2004.

[47] B. Neto, A. Teixeira, N. Wada, and P. André, “Efficient use of hybrid genetic algorithms in the gain optimization of distributed Raman amplifiers,” *Optics Express*, vol. 15, no. 26, pp. 17 520–17 528, Dec. 2007.

[48] B. Min, W. Lee, and N. Park, “Efficient formulation of Raman amplifier propagation equations with average power analysis,” *IEEE Photonics Technology Letters*, vol. 12, no. 11, pp. 1486–1488, Nov. 2000.

[49] M. Fugihara and A. Pinto, “Low-cost Raman amplifier for CWDM systems,” *Microwave and Optical Technology Letters*, vol. 50, no. 2, pp. 297–301, Dec. 2008.

[50] M. Karásek and M. Menif, “Channel addition/removal response in Raman fiber amplifiers: modeling and experimentation,” *IEEE/OSA Journal of Lightwave Technology*, vol. 20, no. 9, pp. 1680–1687, Sep. 2002.

[51] Z. Tong, H. Wei, and S. Jian, “Transient responses to slowly varying input waveforms in backward pumped Raman amplifiers,” *Optics communications*, vol. 218, no. 1, pp. 105–111, Jan. 2003.

[52] J. Gest and L. Chen, “Impact of the all-optical gain-clamping technique on the transience characteristics of cascaded discrete fiber Raman amplifiers,” *Optics Communications*, vol. 273, no. 1, pp. 138–148, Jan. 2007.

[53] C. Giles and E. Desurvire, “Modeling erbium-doped fiber amplifiers,” *IEEE/OSA Journal of Lightwave Technology*, vol. 9, no. 2, pp. 271–283, Feb. 1991.

[54] OFS, “RightWave EDF Family,” (2014). [Online] Available at: http://www.ofsoptics.com/pdf/erbium_doped_optical_fiber.pdf [Accessed 3 Jan. 2015].

[55] A. Saleh, R. Jopson, J. Evankow, and J. Aspell, “Modeling of gain in erbium-doped fiber amplifiers,” *IEEE Photonics Technology Letters*, vol. 2, no. 10, pp. 714–717, Oct. 1990.

[56] Y. Sun, G. Luo, J. Zyskind, A. Saleh, A. Srivastava, and J. Sulhoff, “Model for gain dynamics in erbium-doped fibre amplifiers,” *IET Electronics Letters*, vol. 32, no. 16, pp. 1490–1491, Aug. 1996.

[57] E. Desurvire, J. Sulhoff, J. Zyskind, and J. Simpson, “Study of spectral dependence of gain saturation and effect of inhomogeneous broadening in erbium-doped aluminosilicate fiber amplifiers,” *IEEE Photonics Technology Letters*, vol. 2, no. 9, pp. 653–655, Sep. 1990.

[58] R. Tench and M. Shimizu, “Fluorescence-based measurement of g*(λ) for erbium-doped fluoride fiber amplifiers,” in *Proc. Optical Fiber Communication Conference (OFC)*, Feb. 1997, p. WA3.

[59] G. Luo, J. Zyskind, J. Nagel, and M. Ali, “Experimental and theoretical analysis of relaxation-oscillations and spectral hole burning effects in all-optical gain-clamped EDFAs for WDM networks,” *IEEE/OSA Journal of Lightwave Technology*, vol. 16, no. 4, pp. 527–533, Apr. 1998.

[60] K. Srivastava, J. Zyskind, and J. Sulhoff, “Room temperature spectral hole burning in erbium-doped fiber amplifiers,” in *Proc. Optical Fiber Communication Conference (OFC)*, Feb. 1996, p. TuG7.

[61] A. Bahrampour and M. Mahjoei, “Theoretical analysis of spectral hole burning and relaxation oscillation in all-optical gain stabilized multichannel erbium-doped fiber amplifier (EDFA),” *IEEE/OSA Journal of Lightwave Technology*, vol. 19, no. 8, pp. 1130–1139, Aug. 2001.

[62] P. Wysocki and V. Mazurczyk, “Polarization dependent gain in erbium-doped fiber amplifiers: computer model and approximate formulas,” *IEEE/OSA Journal of Lightwave Technology*, vol. 14, no. 4, pp. 572–584, Apr. 1996.

[63] M. Bolshtyansky, “Spectral hole burning in erbium-doped fiber amplifiers,” *IEEE/OSA Journal of Lightwave Technology*, vol. 21, no. 4, pp. 1032–1038, Apr. 2003.

[64] M. Bolshtyansky, N. King, and G. Cowle, “Dynamic behavior of spectral hole burning in EDFA,” in *Proc. Optical Amplifiers and Their Applications (OAA)*, Jun. 2006, p. OTuB2.

[65] P. Kean, S. Wilson, and M. Healy, “Pump induced inhomogeneity of gain spectra in conventional and extended-band EDFAs,” in *Proc. Optical Fiber Communication Conference (OFC)*, Feb. 1999, pp. 978–980.

[66] M. Yadlowsky, “Pump wavelength dependent spectral hole burning in EDFAs,” *IEEE/OSA Journal of Lightwave Technology*, vol. 17, no. 9, pp. 1643–1648, Sep. 1999.

[67] M. Bolshtyansky, N. King, and G. Cowle, “Characterization of site dependent pumping in EDFA,” in *Proc. Optical Amplifiers and Their Applications (OAA)*, Aug. 2005, p. WB5.

[68] M. Bolshtyansky, N. King, and G. Cowle, “Dynamic behavior of spectral hole burning in EDFA with 980 nm pumping,” in *Proc. Optical Fiber Communication Conference (OFC)*, Mar. 2007, p. OMN2.

[69] M. Holtmannspoetter and B. Schmauss, “Dynamic model of spectral hole burning for EDFAs with 980 nm pumping,” in *Proc. Optical Fiber Communication Conference (OFC)*, no. 2, Mar. 2011, p. OMH4.

[70] C. Layne, W. Lowdermilk, and M. Weber, “Multiphonon relaxation of rare-earth ions in oxide glasses,” *Phys. Rev. B*, vol. 16, no. 1, pp. 10–20, Jul. 1977.

[71] L. Rapp, “Transient behavior of EDFA stages using pump power splitting or pump bypass technique,” *IEEE/OSA Journal of Lightwave Technology*, vol. 25, no. 3, pp. 726–732, Mar. 2007.

[72] L. Rapp and J. Ferreira, “Dynamics of spectral hole burning in EDFAs: dependency on pump wavelength and pump power,” *IEEE Photonics Technology Letters*, vol. 22, no. 16, pp. 1256–1258, Aug. 2010.

[73] L. Rapp, “Effect of spectral hole burning on the feedforward control of erbium-doped fiber amplifiers,” in *Proc. Optical Fiber Communication Conference (OFC)*, Mar. 2010, p. OThI5.

Chapter 3

Simplified Model for Counter–Pumped RFAs

Network planning tools have to explicitly consider the quality of signal in order to minimize network costs and energy consumption [1]. Due to the computational effort required by numerical calculations, the simulation of signal degradation attributable to non–linear effects has to be based on simplified analytical models [2–5]. In addition to simplicity, these models must have good accuracy when estimating the signal degradation [6] in order to ensure that the network resources are used efficiently [7]. Simplified models can also be used to develop new routing algorithms that incorporate the impairments of the physical layer [8] and can be implemented in the control plane of the network [9, 10]. However, it is also necessary to choose the correct constraints to evaluate the feasibility of the lightpath [11], such as the gain and noise figure of optical fiber amplifiers [8, 12]. In order to understand and develop simplified analytical models to describe the signal degradation, an intrinsic understanding of the physical effects in the transmission link is required.

In this chapter, we develop a simplified model with low computational requirements for estimating the gain and amplified spontaneous emission (ASE) noise power of a counter–pumped Raman fiber amplifier (RFA). This model is suitable for use with multiple pumps and with a large number of signals. Using the proposed model, we estimate the OSNR of transmission links with counter–pumped RFA with different lengths and input signal powers, and compare them with numerical simulations. We also present an algorithm to design counter–pumped RFAs based on the proposed simplified model, allowing the reduction of computational requirements. The simplified model described in Section 3.2 was published in [13, 14] and it was implemented in the planning tool of the hosting company of the PhD program. The proposed algorithm to design counter–pumped RFA presented in Section 3.4 was published in [15].

3.1 Introduction

When modeling a RFA in a transmission link, there are three major interactions [16], i.e., pump–to–pump interactions, pump–to–signal interactions, and signal–to–signal interactions, that need to be considered. The signal–to–signal interaction needs to be taken into account even if the transmission link does not have RFAs [17]. For this reason, this interaction is usually considered as part of the transfer function of the transmission fiber and therefore it is not considered in the model of the amplifier.

Several numerical models have been developed to predict and describe the other interactions. In [18], a detailed numerical model (DNM), the average power analysis (APA), is presented. Since this model is faster than other numerical methods, as discussed in Section 2.3.2, it can be chosen for estimating the gain and ASE noise in a reduced time interval. However, it is still not suitable when dealing with large networks due to the computation power required by iterative convergence, particularly when a large number of counter–directional pumps and signals is considered. In [19, 20], the authors developed a closed integral form of coupled Raman equations, which allows a reduction of processing time while still maintaining a good accuracy. Nevertheless, it is still necessary to resort to a recursive propagation through the fiber length, and the time needed for this process may preclude its utilization in more complex scenarios.

Analytical or semi–analytical approaches to develop simplified models tend to imply a significant number of approximations which, in most cases, decrease the accuracy of the models. In [21] a model suitable for the small signal regime of a counter–pumped RFA with a single pump is presented, known as the undepleted pump model (UPM). In [22], it is developed a model for the gain and noise figure for a multi–pump RFA, without considering the pump–to–pump interactions. However, as shown in [23], these interactions tend to be relevant as the number of pumps and their power increases. Considering this, [23] presented an analytical approximated solution for the gain taking into account the pump–to–pump interactions, by iteratively solving the propagation equations for the pumps. These interactions can also be estimated by numerical or semi–analytical models as shown in [24]. In this case, the interactions between the pumps and signals are solved using the Runge–Kutta method. In [25], a semi–analytical model that considers the depleted regime of a RFA with a single pump and with frequency dependent losses is presented. In [26] the authors stated that the composite Raman gain can be expressed as the logarithmic sum of the weighted gain created by each pump wavelength. These weighting factors are obtained after solving the propagation equations.

This chapter is organized as follows. In Section 3.2 we customize the UPM [21], with the introduction of two new parameters in order to account for the pump–to–pump interactions. These parameters can be adjusted based on experimental measurements, simulation results, or analytical expressions. Based on this proposal, we also present and discuss a method to estimate the ASE noise. Using these two parameters, an accurate black box model for the gain profile and ASE noise is obtained without increasing the computational complexity of the UPM. All proposed models are validated by numerical simulations using the DNM presented in Section 2.3.2 and by experimental results. In Section 3.3, we use the proposed model to estimate the OSNR of several wavelength–division multiplexing (WDM) channels in a transmission link with different lengths, input signal powers and fibers types. The accuracy of the proposed model is assessed with a comparison with numerical results obtained by the hosting company. In Section 3.4, we present an efficient algorithm to design RFAs on the fly with low computational requirements. In the proposed algorithm, instead of solving the propagation equations with a DNM, we use a simplified model, which allows the achievement of results in a time efficient manner. The conclusions of this chapter are presented in Section 3.5.

3.2 Weighted Undepleted Pump Model

In order to develop a simplified model for the counter–pumped RFA suitable for network planning tools and routing algorithms, we assume that the pump wavelengths and powers of the amplifiers are known. This is a realistic scenario because usually RFAs have a limited number of pump configurations. The Raman gain coefficient is also a parameter that is assumed to be known for every used fiber. Moreover, we assume that it is possible to know the On/Off gain for a signal centered at a chosen wavelength, which can be obtained numerically or measured experimentally. Regarding the signals, we assume that we know all the wavelengths and input powers injected into the fiber.

Due to the fact that we are assuming that signal–to–signal interactions are part of the transfer function of the transmission fiber, only the pump–to–signal and the pump–to–pump interactions have to be considered. Also, due to the fact that the signal–to–signal interactions are not considered in the simplified model, in this section only one signal, tunable from 1510 nm to 1610 nm, is considered.

To develop a simplified model, we start by separating the contributions of the pump–to–signal and pump–to–pump interactions, neglecting second order effects. First, let us consider the UPM, where a small signal regime is assumed [21]. In this model, only one pump is considered, thus the counter–pumped RFA output signal power, $P_s(L)$, is given by

$$P_s(L) = P_s(0)\exp\left(C_{s,p}P_p(L)L_{eff} - \alpha_s L\right), \tag{3.1}$$

with the effective fiber length, given by

$$L_{eff} = \frac{1-\exp(-\alpha_p L)}{\alpha_p}, \tag{3.2}$$

where $P_s(0)$ is the input signal power at the beginning of the transmission fiber, $P_p(L)$ is the input pump power at the end of the transmission fiber, α_p is the fiber attenuation at the pump wavelength, α_s is the fiber attenuation at the signal wavelength and L is the transmission length. The parameter $C_{s,p}$ is related to the Raman gain efficiency of the fiber. Generically, for waves i and j centered at frequencies ν_i and ν_j, respectively, $C_{i,j}$ is given by [27]

$$C_{i,j} = \begin{cases} \dfrac{g_r(\nu_j-\nu_i)}{2A_{eff}} & \text{if } \nu_j-\nu_i \geq 0 \\ -\dfrac{\nu_i}{\nu_j}\dfrac{g_r(\nu_i-\nu_j)}{2A_{eff}} & \text{if } \nu_j-\nu_i < 0, \end{cases} \tag{3.3}$$

where A_{eff} is the fiber effective area, $g_r(\nu_j-\nu_i)$ is the Raman gain coefficient of the fiber and $\nu_j-\nu_i$ represents the frequency spacing between the two waves. We used the technique presented in [28] to determine the Raman gain coefficient of the standard single mode fiber (SSMF).

In eq. (3.1) only the presence of one pump is considered. However, the UPM can be extended to support multiple pumps. To achieve this, the contribution of the pump for the signal output power in eq. (3.1) is replaced by a sum over all pumps. In this case, the output signal power at the end of the amplifier is given by

$$P_s(L) = P_s(0)\exp\left(\left[\sum_{i=1}^{N} C_{s,i}P_i(L)L_{eff,i}\right] - \alpha_s L\right), \tag{3.4}$$

where

$$L_{eff,i} = \frac{1-\exp(-\alpha_i L)}{\alpha_i}. \tag{3.5}$$

$L_{eff,i}$ is the effective length for each pump wavelength i, $P_i(L)$ is the input pump power of pump i in the counter–pumped configuration, α_i is the fiber attenuation at the pump wavelength i, and N is the total number of pumps.

With this model, we can take into consideration the contribution of each pump to the amplifier gain. However, the interactions between the pumps are not considered. In order to assess the accuracy of eq. (3.4), we perform On/Off gain measurements and detailed numerical simulations (using the APA model presented in Section 2.3.2), in a transmission system with a counter–pumped RFA. In Fig. 3.1 a schematic diagram of the experimental setup implemented is presented. Several pump configurations and pump powers are used. We start with configuration 1 which has four pumps centered at 1426 nm, 1444 nm, 1462 nm, and 1487 nm, with fiber attenuation coefficients of 0.26 dB/km, 0.25 dB/km, 0.23 dB/km, and 0.23 dB/km, respectively. The input pump powers are presented in Table 3.1. The pumps P_1, P_2, P_3, and P_4 are coupled to the fiber using an optical multiplexer, followed by an optical coupler. The transmission fiber is a SSMF with 80 km, an effective area of 80 μm^2, and an attenuation coefficient of 0.2 dB/km around 1550 nm. Since we are interested in measuring the pump–to–signal and pump–to–pump interactions, a tunable laser operating at 0 dBm is used as the probe signal to be amplified. We measure the On/Off gain, from 1510 nm to 1610 nm using an optical spectrum analyzer (OSA).

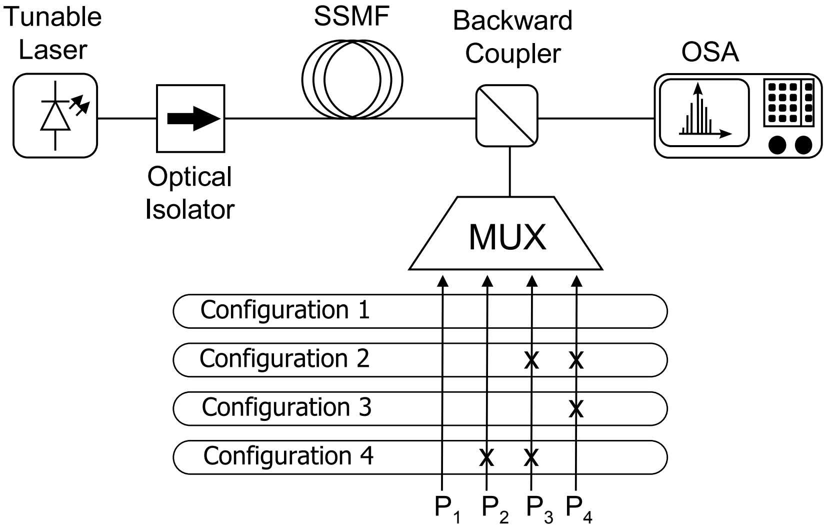

Figure 3.1: Experimental setup used to measure the amplifier On/Off gain. For each used configuration, the pump wavelengths not used are marked with a "X".

Figure 3.2 shows the On/Off gain results as function of the signal wavelength for configuration 1. The results are obtained with experimental measurements, with the UPM, eq. (3.4), and with DNM. Inspection of Fig. 3.2 shows that the DNM accurately describes the experimental data. When comparing the UPM with the experimental or

Table 3.1: Pump wavelengths and input pump powers of the different RFA configurations. In configuration 4, the input pump powers of the two pumps are always increased by the same amount.

	Pumps			
	P_1– 1426 nm	P_2–1444 nm	P_3– 1462 nm	P_4– 1487 nm
Conf. 1	183 mW	236 mW	88 mW	233 mW
Conf. 2	355 mW	257 mW	—	—
Conf. 3	398 mW	279 mW	84 mW	—
Conf. 4	25 - 500 mW	—	—	25 - 500 mW

DNM results, we can observe a large deviation, due to the non–linear effect of SRS between waves that leads to energy transfer between the pumps. This effect between the pumps is highlighted by observing the linear regression of the results obtained with each model, presented in Fig. 3.2. The UPM presents a gain with a negative tilt, whereas the real gain profile presents a positive tilt.

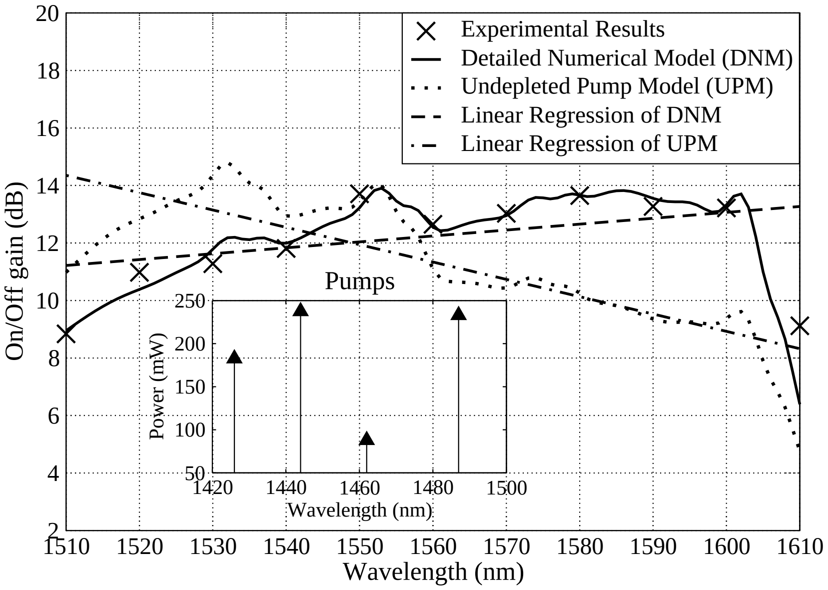

Figure 3.2: On/Off gain measurements and comparison with numerical models for a counter–pumped RFA with four pumps and a total pump power of 745 mW: experimental measurements (crosses); detailed numerical results (full line); undepleted pump model (dotted line); linear regression of the detailed numerical model (dashed line); linear regression of the undepleted pump model (dashed and dotted line). Inset refers to the pump wavelengths and pump powers of the RFA.

3.2.1 Adjustment of the On/Off Gain Tilt

The stimulated Raman scattering (SRS) between pumps changes the pump power distribution within the fiber, resulting in an amplification of the pumps with higher wavelengths and in the depletion of pumps with lower wavelengths. We propose to include this effect on the UPM, eq. (3.4), by correcting the input pump power, in order to consider the pump–to–pump interactions and, therefore, obtain the correct output signal power, i. e.,

$$P_s(L) = P_s(0)\exp\left(\left[\sum_{i=1}^{N} C_{s,i} P_i^{SRS} L_{eff,i}\right] - \alpha_s L\right), \tag{3.6}$$

where P_i^{SRS} is the corrected input pump power of the pump i, considering the pump–to–pump interactions. In order to estimate the P_i^{SRS}, we use

$$P_i^{SRS} = P_i(L)\exp\left(\sum_{j=1}^{N} C_{i,j} P_j(L)\frac{1-\exp(-\alpha_j D_{int})}{\alpha_j}\right), \tag{3.7}$$

where D_{int} can be understood as an interaction length between the pumps, in order to include the effect of amplification or depletion of the pumps due to SRS between them. Since D_{int} does not have any physical meaning, in a first approach, we have to adjust it based on the difference between the proposed model and numerical simulations or experimental measurements. In order to estimate D_{int}, based on a measured or simulated On/Off gain for a given signal s, we start by writing the amplifier On/Off gain using

$$G_s = \frac{P_{s,ON}(L)}{P_{s,OFF}(L)} = \exp\left(\sum_{i=1}^{N} C_{s,i} P_i^{SRS} L_{eff,i}\right), \tag{3.8}$$

where G_s is the On/Off gain for a wavelength s. To simplify this equation, let us consider the same attenuation coefficient for all the pump wavelengths, therefore, $L_{eff,i} = L_{eff}$. Using eq. (3.8), we obtain

$$\ln(G_s) \approx L_{eff}\sum_{i=1}^{N} C_{s,i} P_i(L)\exp\left(L_{eff'}\sum_{j=1}^{N} C_{i,j} P_j(L)\right), \tag{3.9}$$

where,

$$L_{eff'} = \frac{1-\exp(-\alpha D_{int})}{\alpha}. \tag{3.10}$$

Considering a first order of the Taylor expansion of the exponential in eq. (3.9), we obtain

$$\frac{\ln(G_s)}{L_{eff}} - \sum_{i=1}^{N} C_{s,i} P_i \approx L_{eff'} \sum_{i=1}^{N} \sum_{j=1}^{N} C_{s,i} C_{i,j} P_i P_j, \tag{3.11}$$

Expanding the exponentials of L_{eff} and $L_{eff'}$, and solving with respect to the coefficient D_{int}, we can write

$$D_{int} \approx \frac{\ln(G_s) - L \sum_{i=1}^{N} C_{s,i} P_i}{L \sum_{i=1}^{N} \sum_{j=1}^{N} C_{s,i} C_{i,j} P_i P_j}. \tag{3.12}$$

This expression relates D_{int} with the measured or simulated On/Off gain for the signal s. Replacing G_s with an experimental or numerical result, it is possible to obtain D_{int}. However, this derivation assumes some approximations, such as the exponential approximation based on the first order Taylor series. To minimize the possible impact of the approximations performed, several wavelengths must be compared and the chosen wavelength, s, should be the one which best adjusts the On/Off gain tilt given by eq. (3.6), when compared with DNM or experimental measurements.

Let us consider the amplifier shown in configuration 1. By simulating the On/Off gain at different wavelengths with the DNM and using it on eqs. (3.6), (3.7), and (3.12), we verify that the wavelength that better adjusts the tilt is 1571 nm. Fig. 3.3 shows the On/Off gain results as function of the signal wavelength for configuration 1. The results are obtained with experimental measurements, with the customized undepleted pump model (CUPM), and with the DNM. Moreover, the linear regressions for the detailed numerical simulations and for the CUPM are shown. When the CUPM is tuned using the simulated On/Off gain for the signal 1571 nm, we verify that the gain tilt is well adjusted. This result is highlighted by the comparison between the linear regressions of the DNM and of the CUPM, which present the same tilt. However, an offset of about 2 dB in the gain is still present.

3.2.2 Adjustment of the On/Off Gain Offset

We can adjust the offset in the On/Off gain of the RFA by including another parameter in the model, i. e.

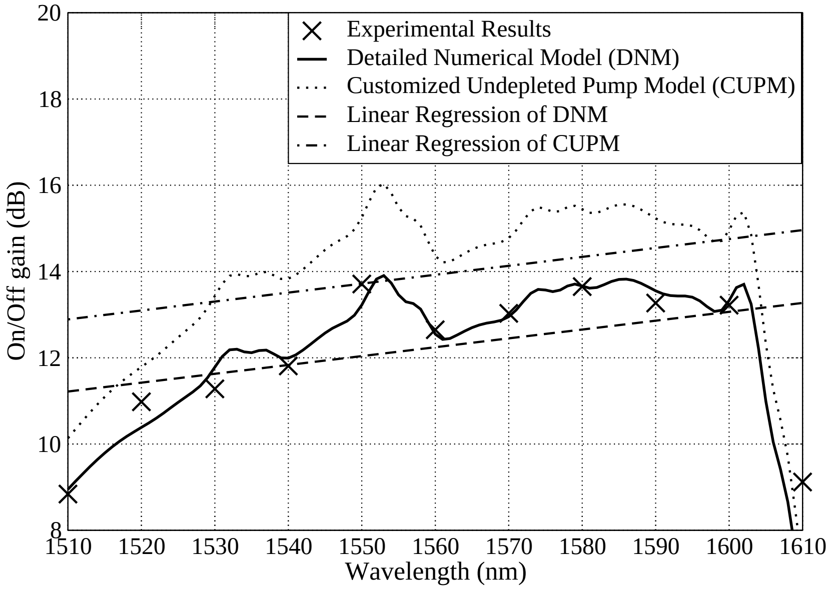

Figure 3.3: On/Off gain measurements and comparison with numerical models for a counter–pumped RFA with four pumps and a total pump power of 745 mW: experimental measurements (crosses); detailed numerical results (full line); weighted undepleted pump model (dotted line); linear regression of the detailed numerical model (dashed line); linear regression of the weighted undepleted pump model (dashed and dotted line), when adjusting the tilt.

$$P_s(L) = P_s(0)\exp\left(\left[\sum_{i=1}^{N} C_{s,i} P_i^{SRS} L'_{eff,i}\right] - \alpha_s L\right), \tag{3.13}$$

where $L'_{eff,i}$ is given by

$$L'_{eff,i} = \frac{1-\exp(-(\alpha_i + \alpha_{SRS})L)}{\alpha_i + \alpha_{SRS}}, \tag{3.14}$$

where α_{SRS} accounts for a gain reduction due to the depletion of the pumps, and $C_{s,i}$ is given by eq. (3.3).

We can write the On/Off gain difference between the CUPM, G_t, obtained with eq. (3.6), and the experimental or numerical result, G_s, for the wavelength s, as

$$\begin{aligned} \Delta G_s = \exp&\left(\sum_{i=1}^{N} C_{s,i} P_i^{SRS} L_{eff,i}\right) \\ -\exp&\left(\sum_{i=1}^{N} C_{s,i} P_i^{SRS} L'_{eff,i}\right). \end{aligned} \tag{3.15}$$

Solving eq. (3.15) in order to $L'_{eff,i}$ and considering the first order of the Taylor expansion of the exponentials, we obtain

$$L'_{eff,i} = -\frac{\Delta G_s}{\sum\limits_{i=1}^{N}(C_{s,i}P_i^{SRS})} + L_{eff,i}. \tag{3.16}$$

Setting $L_{eff,i} \approx 1/\alpha_i$, and $L'_{eff,i} \approx 1/(\alpha_i + \alpha_{SRS})$, we obtain

$$\alpha_{SRS} = \frac{1}{-\frac{\Delta G_s}{\sum\limits_{i=1}^{N} C_{s,i}P_i^{SRS}} + \frac{1}{\alpha_i}} - \alpha_i. \tag{3.17}$$

Figure 3.4 shows the On/Off gain results as function of the signal wavelength for configuration 1. The results are obtained with experimental measurements, with the CUPM, and with the DNM. The linear regressions for the DNM and for the CUPM are also shown in the figure. We can observe similar results both with the CUPM with the tilt and offset adjusted based on the gain of a selected wavelength, and the DNM. This result is highlighted by observing the linear regression of the CUPM and DNM. With this, we show that when using a proper wavelength, both the tilt and the offset are well adjusted and the CUPM estimates the gain with good accuracy. We conclude that the error introduced when deriving the model is compensated by the proper choice of the reference signal wavelength.

3.2.3 Analytical Expressions for the Two Adjustment Parameters

We have shown that it is possible to obtain accurate results for the amplifier gain based on a customization of the UPM with two extra parameters. These parameters are estimated based on the comparison with experimental or numerical results, and we named this method weighted–by comparison (WBC). Nevertheless, it can be useful to have analytical expressions for D_{int} and α_{SRS}.

In a first attempt to develop an analytical model to estimate D_{int}, we can perform several numerical simulations and adjust D_{int} in order to minimize the difference between the proposed model and numerical simulations. Thus, this parameter can be found by setting α_{SRS} to zero and minimizing the mean squared error (MSE) between the gain obtained by this model and the gain obtained from numerical simulations. The MSE is given by

$$MSE = \frac{1}{N}\sum_{i=1}^{N}(x_i - \hat{x}_i)^2 \tag{3.18}$$

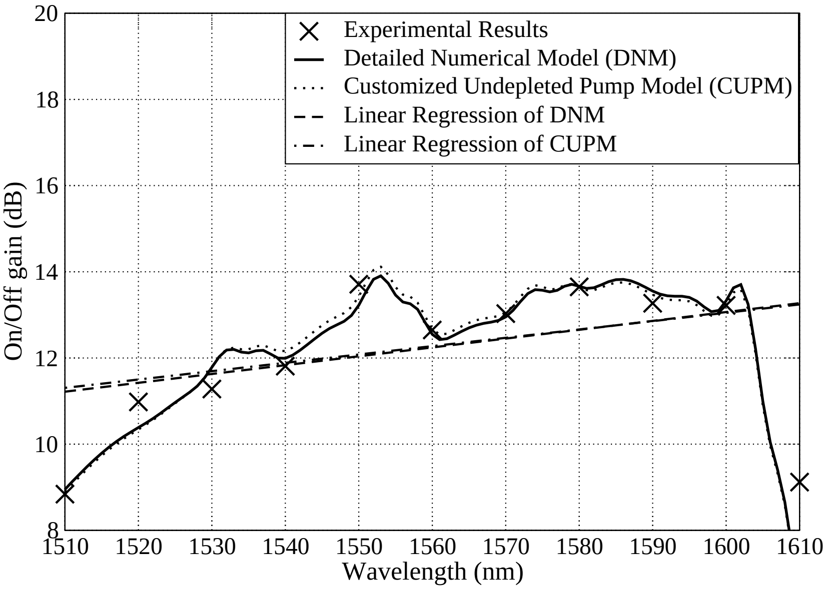

Figure 3.4: On/Off gain measurements and comparison with numerical models for a counter–pumped RFA with four pumps and a total pump power of 745 mW: experimental measurements (crosses); detailed numerical results (full line); weighted undepleted pump model (dotted); linear regression of the detailed numerical model (dashed line); linear regression of the weighted undepleted pump model (dashed and dotted line), when adjusting the tilt and offset.

---

where $\hat{x_i}$ is the On/Off gain for each signal wavelength obtained with the numerical model in decibels, x is the On/Off gain obtained by the proposed model in decibels, and N is the number of wavelengths in the considered wavelength window. We use the MSE function because, as it squares the gain deviations, the values with a higher deviation will have more weight in the error function. Thus, by minimizing the MSE, we are reducing the deviations between the proposed model and the numerical simulations. By adjusting D_{int}, we obtain the solution presenting smaller gain deviations and, therefore, closer to the numerical simulation results.

We can use the MSE to assess the behavior of D_{int} as function of the pump power and the frequency separation between pumps. For these simulations, we consider a 80 km SSMF with an effective area of $80\,\mu m^2$. The pump wavelengths are centered at 1426 nm, 1444 nm, 1462 nm, and 1487 nm, with an attenuation coefficient of 0.25 dB/km, 0.24 dB/km, 0.23 dB/km, and 0.23 dB/km, respectively, and are arranged in different setup configurations. Setup 1 has 3 pumps centered at 1426 nm, 1444 nm, and 1467 nm; setup 2 has two pumps centered at 1426 nm and 1462 nm; and setup 3 has 3 pumps centered at 1426 nm, 1462 nm, and 1487 nm. The pump power is increased equally for all the pump wavelengths considered in each setup. The attenuation coefficient for the signals wavelengths is 0.20 dB/km. The optimized value for D_{int} is found when the MSE between the gain obtained by the simplified model and the one estimated by the numerical model is minimized.

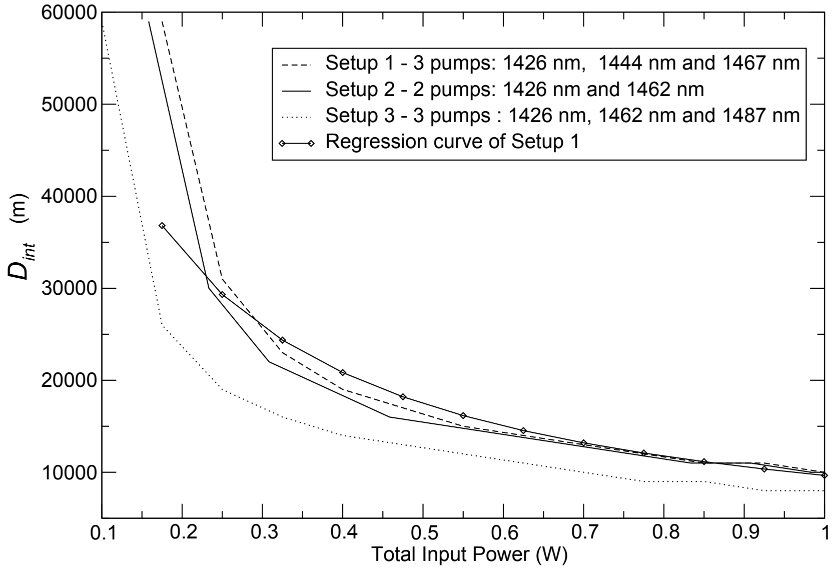

Figure 3.5: D_{int} as a function of the total input power for a RFA with two and three pumps.

Figure 3.5 shows the evolution of the parameter D_{int} as function of the total input power for a RFA with two and three pumps. It can be observed that D_{int} decreases as the total input pump power increases. Also, although setups 1 and 2 have different number of pumps, the fact that their first and last pumps have the same wavelength leads to a similar behavior and follows the regression equation of setup 1, which is obtained by fitting the results obtained for setup 1. On the other hand, setup 3 and setup 1 have 3 pumps, but different pump wavelength separation between the pump wavelengths. When comparing the results obtained for these setups, we can see that the behavior of the curve is different. This suggests that there is a dependency between D_{int} and the maximum separation of the pump wavelengths.

Considering that the CUPM should converge for the UPM when the number of pumps is one, due to the fact that there is no pump depletion when considering only one pump in the amplifier, we expect that both D_{int} and α_{SRS} approach zero for this configuration. Moreover, as shown in Fig 3.5, D_{int} should be inversely proportional to the total pump power, and should account for the pump–to–pump interactions. Based on the stated principles, and only considering known parameters of the system, we find an analytical expression for D_{int} that better adjusts the results obtained from several simulations for different scenarios. That equation can be written as

$$D_{int} \approx \frac{N_{pumps} - 1}{P_{total} \sum\limits_{j=2}^{N} |C_{1,j}|}, \tag{3.19}$$

where $C_{1,j}$ is the Raman gain efficiency of the fiber between the first pump P_1 and the pump j, N_{pumps} is the number of pumps, and P_{total} is the total input pump power.

After developing an analytical equation for D_{int}, to complete the model we need to find a second analytical equation for estimating α_{SRS}. α_{SRS} can be understood as an extra attenuation at the pump wavelength that accounts for the loss of power due to the pump depletion. When considering several pumps in a RFA, the pump with highest depletion is the pump with the smaller wavelength, thus the behavior of the α_{SRS} should be proportional to the loss of power of the first pump. After simulating several scenarios with different numbers of pumps and pump powers, we verify that α_{SRS} can be written as function of the logarithm of the remaining power after taking into account the depletion of the first pump divided by the input pump power and further divided by the transmission distance. Therefore, in dB/km,

$$\alpha_{SRS} \approx -\frac{10}{L} \log_{10}\left(\frac{P_1^{SRS}}{P_1(L)}\right). \tag{3.20}$$

With eqs. (3.19) and (3.20), we are able to propose a model for the output signal power of RFAs with different number of pumps and powers, excluding the need to compare with experimental measurements or numerical simulations in order to adjust the parameters. This approach is defined as weighted–by analytic expression (WAE) and it is given by eq. (3.13), and eq. (3.7), and the parameters, D_{int} and α_{SRS}, obtained with the analytical expressions eq. (3.19), and eq. (3.20).

Figure 3.6 shows the On/Off gain results as function of the signal wavelength for configuration 1 considering experimental measurements, the WAE model, and the DNM. As one can see, the results obtained with the WAE present good accuracy, although slightly lower than the accuracy achieved when D_{int} and α_{SRS} are obtained through comparison with the WBC model, see Fig. 3.4. Nevertheless, based on WAE, the obtained results do not require any comparison with experimental or numerical data, which can make this method simpler to use than the WBC model.

3.2.4 Performance Assessment

We have assessed the accuracy of the CUPM adjusted by WBC and WAE, when considering a counter–pumped RFA with four pumps. However, in order to further assess

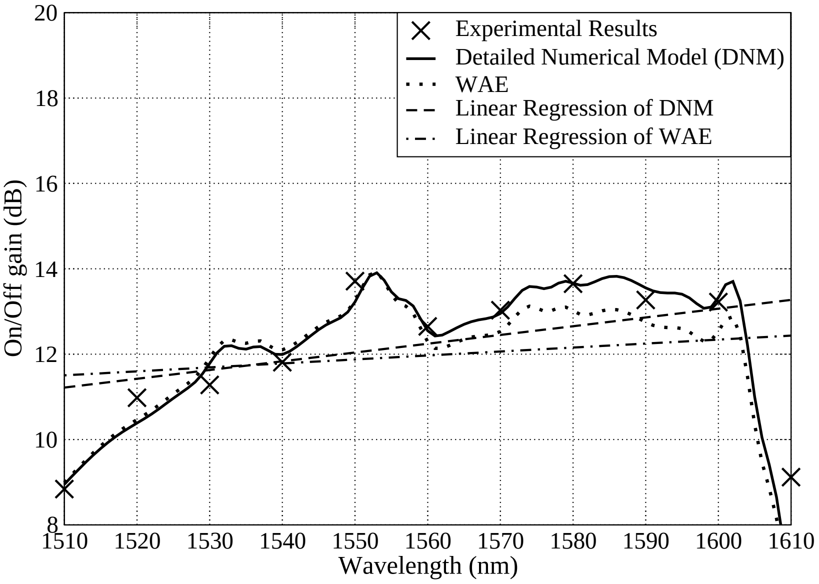

Figure 3.6: On/Off gain measurements and comparison with numerical models for a counter–pumped RFA with four pumps and a total pump power of 745 mW: experimental measurements (crosses); detailed numerical results (full line); WAE (dotes); linear regression of the detailed numerical model (dashed line); linear regression of the WAE (dash and dot line).

---

the proposed model in scenarios with different number of pumps, pump wavelengths and powers, we experimentally implement one counter–pumped RFA with two pumps and one with three pumps, see Fig. 3.1 and Table 3.1. We consider the same assumptions for configurations 2 and 3 as the ones presented for configuration 1 in Section 3.2. We measure the signal On/Off gain for configuration 2 and 3 from 1510 nm to 1570 nm.

Figures 3.7 and 3.8 show the On/Off gain results as function of the signal wavelengths for configurations 2 and 3, respectively. The results are obtained with experimental measurements, with detailed numerical simulations, and with the WBC and WAE models. Inspection of the figures show that the DNM provides good accuracy when estimating the amplifier gain for the configurations. On the other hand, the UPM is the most inaccurate, presenting a higher error for configuration 3. Regarding the WBC and the WAE approaches to estimate the parameters of the CUPM, we verify that the results obtained have a good accuracy for configurations 2 and 3. Also, both approaches provide similar results. To further discuss the error of the gain profile estimation, we measure the mean absolute error (MAE) between the estimated and measured gain profiles, which is given by

$$\mathrm{MAE} = \frac{1}{n}\sum_{i=1}^{n} |G_i - G_{ref,i}|, \tag{3.21}$$

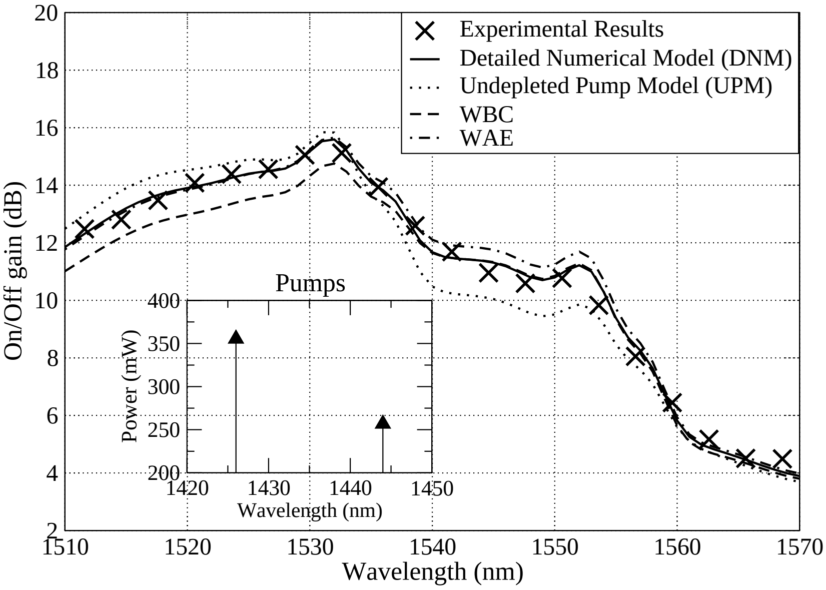

Figure 3.7: On/Off gain measurements and comparison with numerical models for a counter–pumped RFA configuration 2 with a total pump power of 612 mW: experimental measurements (crosses); detailed numerical results (full line); undepleted pump model (dotted line); weighted undepleted pump model based on comparison with experimental or detailed numerical simulation, WBC (dashed line); weighted undepleted pump model based on analytical expressions, WAE (dashed and dotted line). Inset refers to the pump wavelengths and pump powers of the RFA.

---

where G_i is the estimated gain that we want to evaluate in decibels, $G_{ref,i}$ is the reference gain profile in decibels, and n is the total number of wavelengths measured.

Figure 3.9 shows the MAE of the UPM, the DNM, the WBC model and the WAE model, when compared with the experimental measurements, for configurations 1, 2, and 3. An analysis of Fig. 3.9 shows that the DNM correctly describes the experimental measurements for all the setups considered, with a MAE below 0.5 dB. When considering the UPM, we verify that it presents a higher error than the DNM. Moreover, this error increases with the number of pumps and respective powers, until a MAE of 2.8 dB is reached for configuration 1. When comparing the CUPM, adjusted with WBC and WAE, we verify that, for some configurations, the MAE almost matches the DNM, which highlights the accuracy of the proposed models. Nevertheless, we verify that, when using the WBC, typically the error is smaller than when using the WAE. Regarding configuration 2, the WBC presents a slightly higher error than the UPM. This happens because the depletion of the first pump is over estimated by the model. This is due to the fact that, in this configuration, the first pump has a higher input power than the second and the wavelength separation between them is small, about 18 nm, which means that the depletion is almost negligible.

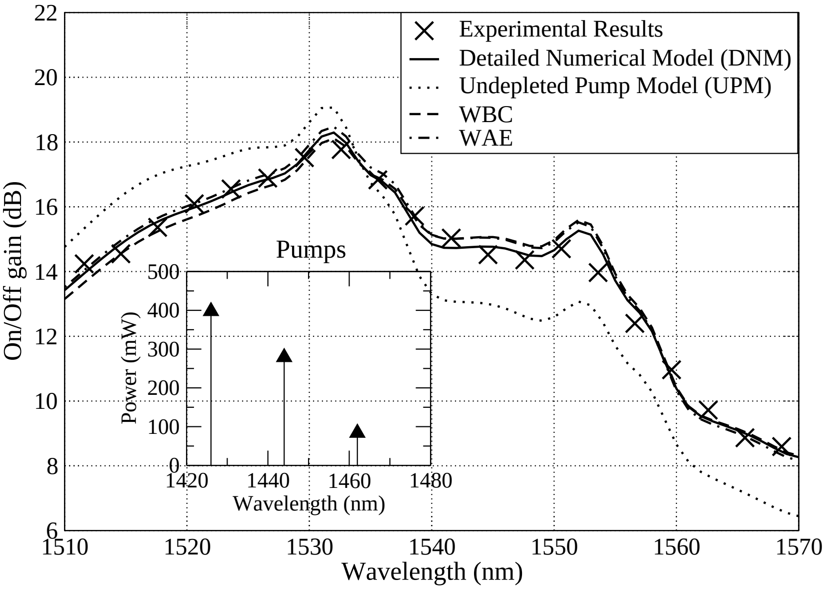

Figure 3.8: On/Off gain measurements and comparison with numerical models for a counter–pumped RFA configuration 3 with a pump power of 760 mW: experimental measurements (crosses); detailed numerical results (full line); undepleted pump model (dotted line); weighted undepleted pump model based on comparison with experimental or detailed numerical simulation, WBC (dashed line); weighted undepleted pump model based on analytical expressions, WAE (dashed and dotted line). Inset refers to the pump wavelengths and pump powers of the RFA.

It is also important to assess the impact of the fiber length on the accuracy of the proposed model. Therefore, we calculate the MAE as function of the fiber length, for the UPM, the WBC and for the WAE, when compared with DNM for configuration 1. Fig. 3.10 shows the MAE as function of the transmission distance for the UPM, the WBC and WAE, when compared against the DNM. The results in the figure show that, when considering the WBC model, the MAE is below 0.3 dB for all the distances considered. For the WAE model, the results present a MAE below 0.5 dB up to 180 km. Moreover, the UPM provides a higher error when compared with the proposed models. The obtained results for all other configurations are similar to the ones presented. Therefore, based on the obtained results we verify that the proposed models maintain the accuracy for transmission distances up to 180 km.

The evaluation of the behavior of the proposed model with the increase of the total input pump power is also important. To achieve this, we increase the total pump power in intervals of 100 mW, with power equally distributed for all the pumps in the amplifier. For this trial, we selected configuration 1 and 4, see Table 3.1, which have 4 and 2 pumps, respectively, and an equal spacing between the first pump and the last pump. The On/Off gain is estimated using the UPM, the WAE, and the WBC. All

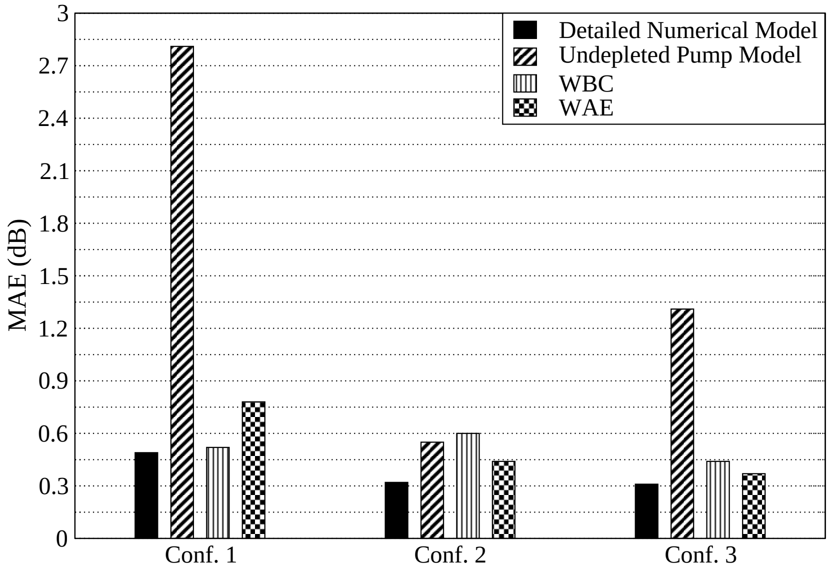

Figure 3.9: MAE of the On/Off gain for the different models for configurations 1, 2 and 3, when compared with experimental results.

---

estimations are compared with results obtained with the DNM. Fig. 3.11 shows the MAE as function of the total input power, for the UPM, the WBC, and WAE, when compared with the DNM for configurations 1 and 4, see Table 3.1. Considering the WBC approach, we verify that the obtained MAE is always below 0.4 dB. Regarding WAE, we conclude that it tends to be suitable for a total pump power of up to 900 mW and a wavelength separation below 60 nm between the first and last pump, considering a MAE up to 1 dB. When comparing the WBC and WAE approaches with the UPM, we verify that the results are significantly improved.

The processing time is also an important factor when validating the applicability of a simplified model. In Table 3.2 is shown the processing time of each model for configurations 1, 2, and 3. When considering configuration 1, the processing time to calculate individually the On/Off gain of 100 signals, by the DNM, with a spacial resolution of 200 m and a convergence criterion of 1x10^{-6}, is longer than 7300 ms, contrary to the WAE, which takes less than 100 ms. This means that the WAE is more than 70 times faster than the DNM for this configuration. When considering configurations 2 and 3, to calculate individually the On/Off gain of 70 signals, the DNM took more than 2500 ms and 4700 ms, respectively. When considering the WAE, the process takes less than 40 ms and 50 ms, respectively. As we can observe, the WAE is faster than the DNM even in simpler configurations. Also, considering WAE, the processing time is almost the same, despite the complexity of the RFA configurations. As expected, when comparing the WAE with the UPM, the computational time is similar for all configurations considered. Regarding the WBC approach, the computational time is

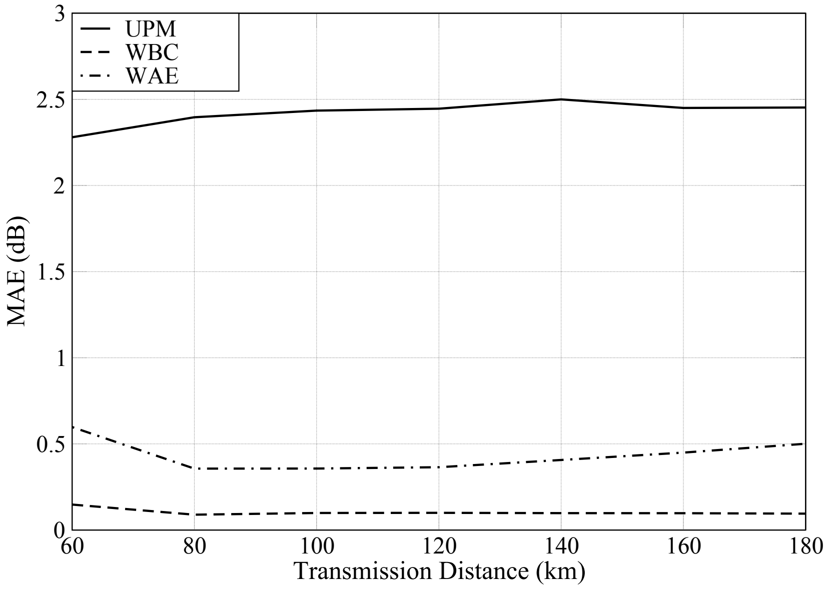

Figure 3.10: MAE between the On/Off gain obtained with the UPM, WBC and WAE, when compared with the DNM, for different transmission distances for configuration 1, see Table 3.1.

---

not tested because it is necessary to adjust the parameters based on a comparison with either numerical simulations or experimental measurements. However, after determining the parameters D_{int} and α_{SRS}, the computational time for each configuration is similar to WAE.

Table 3.2: Processing time, in milliseconds (ms), of the models in an Intel T5500 processor at 1.66 GHz with 2 GB of RAM.

Model	**Conf. 1**	**Conf. 2**	**Conf. 3**
Detailed Numerical Model (DNM)	7300	2500	4700
Undepleted Pump Model (UPM)	90	35	50
WAE	90	40	50

3.2.5 ASE Noise Model

Some planning tools and routing algorithms are based not only on the amplifier gain profile, but also on the optical signal–to–noise ratio (OSNR) after the transmission links. Therefore, it is also important to develop and improve the noise estimation for the transmission systems.

The ASE noise of the amplifier can be related to the amplifier gain [29, 30]. For this reason, we can apply the proposed approach to better estimate the ASE noise

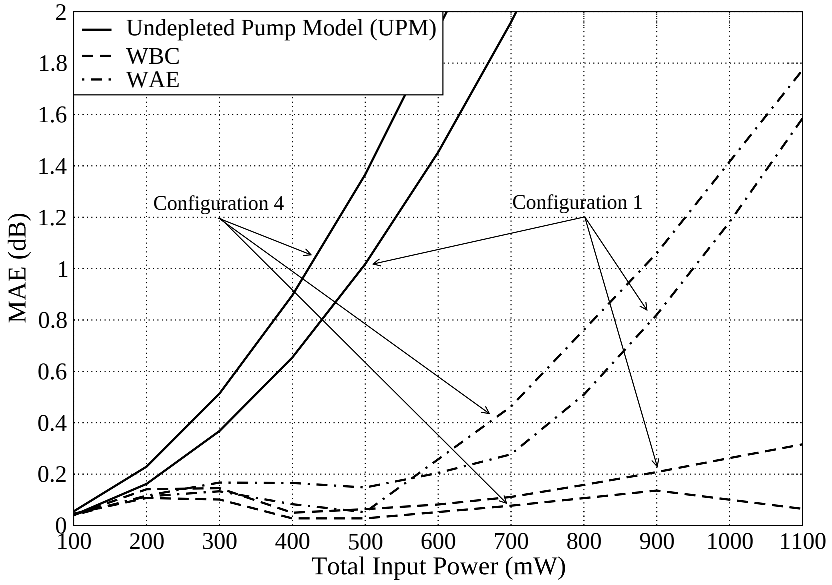

Figure 3.11: MAE between the On/Off gain obtained with the undepleted pump model, WBC and WAE, when compared with the DNM, for different total input pump powers for configuration 1 and configuration 4, see Table 3.1.

---

profile of the RFA. Let us consider a multi–pumped RFA. The net gain, G, is given by [29]

$$G = \exp(-\alpha_{signals} L) \prod_i g_i, \tag{3.22}$$

where i refers to the pump of the configuration implemented and $\alpha_{signals}$ the attenuation coefficient of the fiber. Considering the UPM, g_i is given by

$$g_i = \exp\left(C_{s,i} P_i(L) L_{eff,i}\right). \tag{3.23}$$

Using the proposed model, we can estimate g_i using

$$g_i = \exp\left(C_{s,i} P_i^{SRS} L'_{eff,i}\right), \tag{3.24}$$

where P_i^{SRS} is the corrected input pump power given by eq. (3.7) and $L'_{eff,i}$ is given by eq. (3.14). Based on [29] and considering the proposed model, the ASE noise power at the end of the amplifier, L, can be written as

$$\begin{gathered} P_{ASE}(L) = h\nu B_0 \left[\frac{\sum\limits_i E_i \ln(g_i)}{\sum\limits_i \ln(g_i)}\right] \\ \left[\left(1+\frac{\alpha L_{eff}\exp(\alpha L)}{\sum\limits_i \ln(g_i)}\right) G - \left(1+\frac{\alpha L_{eff}}{\sum\limits_i \ln(g_i)}\right)\right], \end{gathered} \tag{3.25}$$

where α is the average attenuation coefficient of the fiber at the pump wavelengths and E_i is the spontaneous factor, given by

$$E_i = 1 + \frac{1}{\exp\left(\frac{h\Delta\nu_i}{k_B T}\right) - 1}, \tag{3.26}$$

and h is the Planck's constant, k_B is the Boltzman's constant, T is the temperature in Kelvin, $\Delta\nu_i$ is the frequency difference between the i–th pump and signal, and B_0 is the reference bandwidth.

Figure 3.12 shows experimental measurements for the ASE noise power as function of the wavelength for configuration 1, from 1520 nm to 1590 nm. The ASE noise power is measured without signals and the reference bandwidth is 2.5 GHz. The ASE noise power is also numerically simulated with the ASE noise model eq. (3.25), when using the UPM or the WAE model to estimate the gain of the amplifier. When comparing the experimental results with the ones obtained using the UPM to estimate the gain of the amplifier, we verify that there is a deviation between the results higher than 2 dB, which is not suitable. When comparing the results obtained using the WAE to estimate the amplifier gain with the experimental results, we verify that the ASE noise powers are correctly described. However, a maximum deviation of about 1 dB is still present. This suggests that this model needs further improvements, which will be discussed in Section 3.3.

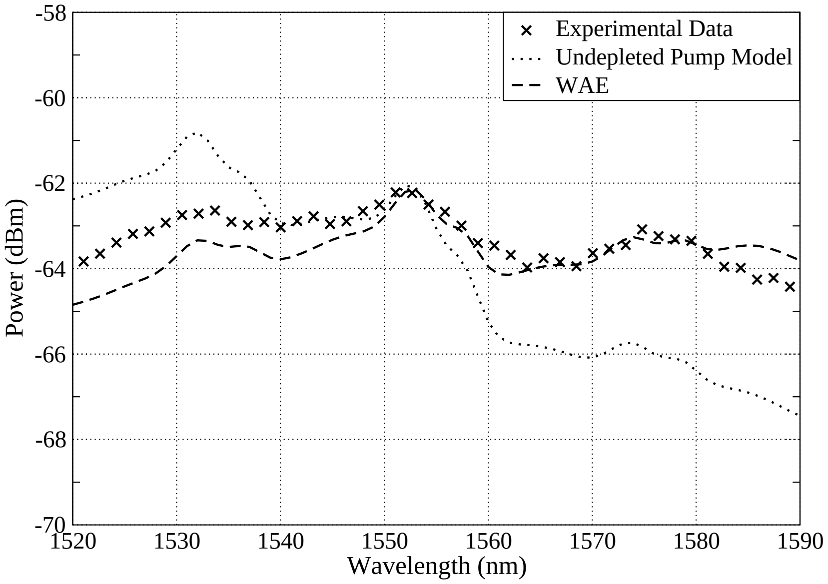

Figure 3.12: ASE noise measured and estimated based on the UPM and on WAE for the amplifier of configuration 1.

3.3 OSNR Estimation in a Transmission Link With a RFA

In Section 3.2 we proposed and validated the WAE model for the gain and ASE noise generation when considering a different number of pumps and pump powers. However, only one signal is used to probe the amplifier On/Off gain. In order to verify if the proposed WAE model can be a good choice of implementation in network planning tools, further validations are needed when considering WDM channels in transmission links with different fibers types, input signals powers, and distances.

3.3.1 Insertion Losses and Pump Configuration of the RFA

When including a RFA element in the transmission link, extra losses are introduced along the signal path. Table 3.3 shows the system losses for pumps and signals due to the insertion of the RFA element. The signals, going from "line in" to "line out" connectors, are subject to a loss of 1.2 dB due to couplers and connections inside the RFA. The pumps are also subjected to a loss between the pump fiber pigtail splice and the "line in" port of the element, called "pump path loss". As shown in Table 3.3, this loss is assumed to be the same for every pump and equal to 1.8 dB. There is an additional loss between the "line in" port and the transmission fiber, which accounts for patch panel losses and is assumed to be 0.4 dB. This loss affects both pumps and signals. Therefore, due to the insertion of the RFA in the transmission system, the signals and the ASE noise signals at the input of the RFA will have an extra attenuation of 1.8 dB. This attenuation directly affects the output signal and output ASE noise powers. The pumps will have an attenuation of 2.3 dB, which will reduce the injected pump power in the amplifier. Thus, when configuring the pump powers, this value needs to be taken into account, in order to obtain a gain flattened amplifier.

Table 3.3: System losses due to the insertion of the RFA.

	Patch panel (dB)	**Path loss (dB)**	**Connectors (dB)**	**Total (dB)**
Signals	0.4	1.2	0.2	1.8
Pumps	0.4	1.8	0.1	2.3

Table 3.4 shows the pumps wavelengths and maximum output powers of the considered counter–pumped broadband RFA element. The pumps are centered at 1424 nm, 1435 nm, 1455 nm, and 1472 nm, with a maximum pump power of 360 mW for each

pump. The RFA is designed in such a way that the pump power for each pump wavelength is divided by the two orthogonal polarizations of the fiber.

Table 3.4: Pump wavelengths and maximum powers of the considered RFA.

LD#	**Wavelength (nm)**	**Max. power (mW)**
1	1424	360
2	1435	360
3	1455	360
4	1472	360

3.3.2 Transmission Link Model

Since the transfer function of the transmission fiber in the planning tool takes into account the signal–to–signal interactions, when estimating the On/Off gain of the transmission link we have to separate the contributions of the signal–to–signal interactions from the On/Off gain of the amplifier. Therefore, the On/Off gain of the transmission link with Raman amplification is the summation of the On/Off gain between signals, and the On/Off gain between the pumps and signals. Thus, we have to estimate the output signals powers and the ASE noise powers by taking into account the different gains and losses present in the transmission system separately. In order to estimate the output signal power we need to take into consideration the transmission losses and the insertion losses of the RFA element, the On/Off gain due to signal–to–signal interactions and the amplifier On/Off gain. Similarly, to estimate the ASE noise we have to consider the transmission losses and the insertion losses of the RFA element, the On/Off gain due to the interaction between the ASE noise, and the generation and amplification of the ASE noise.

Based on the summation of all of these contributions, the system output signal power and the output ASE noise power are given by, in decibels,

$$P_{out}(s) = P_{in}(s) - A_{fiber}(s) + G_{signals}(s) + G_{RFA}(s) - A_{RFA}, \tag{3.27}$$

$$P_{ase,out}(a) = 10\mathrm{Log}_{10}(10^{P_{ase,trans}(a)/10} + ase_{RFA}(a)), \tag{3.28}$$

where

$$P_{ase,trans}(a) = P_{ase,in}(a) - A_{fiber}(a) + G_{signals}(a) - A_{RFA}, \tag{3.29}$$

and where $P_{in}(s)$ is the input signal power, the $A_{fiber}(s)$ is the total attenuation of the fiber for the signal index s, $G_{signals}$ is the gain or losses due to signal–to–signal interaction for the signal s along the transmission fiber, G_{RFA} is the On/Off gain of the amplifier for the signal s, and A_{RFA} is the attenuation caused by including the RFA in the signal path. $P_{ase,in}(a)$ is the input ASE noise power of wavelength a in linear units, ase_{RFA} is the ASE noise generation of the RFA for the wavelength a in linear units, and $G_{signals}(a)$ accounts for the On/Off gain for the ASE noise wavelength a due to interaction between the ASE noise wavelengths.

In order to estimate $P_{out}(s)$, we assume that the $P_{in}(s)$ is known, as well as the transmission losses. Since we do not have any simplified tool or lookup table to estimate $G_{signals}$, we simulate the impact of the signal–to–signal interaction with the APA model presented in Section 2.3.2, having the pumps set to zero. Finally, the G_{RFA} is the only unknown variable in order to calculate $P_{out}(s)$, which will be calculated using the WAE model. Regarding the ASE noise output power estimation, the input ASE noise power is known, and $G_{signals}(a)$ is numerically simulated with the APA model, presented in Section 2.3.2. The ASE_{RFA} will be obtained as presented in Section 3.2.5.

3.3.3 WDM Signals Output Power and ASE Noise Output Power

Let us consider a transmission system with 96 channels starting at 1528 nm and with 50 GHz of channel spacing. Each channel is considered to be a continuous wave (CW) channel. The fiber length, input signal powers, and the amplifier gain are selected in such a way that the total attenuation at the end of the transmission link with the RFA gain still allows the detection of the signals at the receiver. The transmission fiber can be a SSMF or a large effective area fiber (LEAF). The fiber characteristics are shown in Table 3.5. Due to the different characteristics of the fiber, the gain provided by the RFA will be different for both fibers. For that, we consider a gain of 10 dB for the SSMF and a gain of 13 dB for the LEAF fiber. For each fiber type, several distances, with a total propagation loss around 20 dB, 25 dB, 30 dB, and 40 dB for the signals and with different input signal powers are considered, as we can see in Table 3.6 for the SSMF fiber and in Table 3.7 for the LEAF. For each link, an optimization of the pump powers is performed in order to minimize the ripple of the output signal power for the given trial. The initial conditions are the input signal powers and the input ASE noise powers. In these trials we assume that P_{in} is adjusted in such a way that, after the transmission link, the output signal power is flattened. This means that the input signal power is tilted in an opposite way to the $G_{signals}$.

Table 3.5: SSMF and LEAF characteristics, g_r correspond to the peak Raman gain coefficient and the attenuation is referred to a wavelength around 1550 nm.

Fiber	$g_r(m/W)$	$A_{eff}(m^2)$	**Loss (dB/km)**
SSMF	2.8x10^{-14}	80x10^{-12}	0.22
LEAF	3.5x10^{-14}	72x10^{-12}	0.22

Table 3.6: Trial number and parameters used, when considering a SSMF with a counter–pumped RFA with 10 dB of On/Off gain.

Trial	**Distance (km)**	**Total loss (dB)**	**Power per Channel (dBm)**
1	91	20	-1.1
2	114	25	0.7
3	136	30	2.7
4	182	40	3.2

In order to assess the accuracy of the proposed simplified model, we will compare the results obtained against numerical simulations performed by the hosting company. These reference numerical results were obtained based on the model presented in [31]. From these reference results we obtain the output signal power, the output ASE noise power, and the OSNR at the end of the transmission link.

When using the WAE model to estimate $P_{out}(s)$ and $P_{ase,out}(a)$, we consider the same set of conditions used on the reference numerical simulations. This means that the attenuation, the Raman gain coefficient for each fiber, the input signal power and the input ASE noise power, are the same as the ones used in the numerical simulations. We assess the maximum deviation between the the WAE model for the output signal power and the ASE noise power and the respective simulated value. The maximum deviation is chosen because it provides a better understanding of the maximum difference between the reference numerical results and the estimated ones. Regarding the comparison between the OSNR results we also use the MAE to assess the average error when considering all signals in the transmission link.

Output Signal Power Estimation

Let us estimate the output signal power according to eq. (3.27) of trial 8, see Table 3.7. The optimized pump powers used in the RFA element are shown in Table 3.8. In Fig. 3.13(a), the input signal power in the transmission link as function of the signals wavelength is given. As discussed, the input signal spectrum is tilted in order to

Table 3.7: Trial number and parameters used, when considering a LEAF with a counter–pumped RFA with 13 dB of On/Off gain.

Trial	**Distance (km)**	**Total loss (dB)**	**Power per Channel(dBm)**
5	91	20	-1.1
6	114	25	0.7
7	136	30	2.7
8	182	40	3.2

compensate for the signal–to–signal interactions. We estimate $G_{signals}$ using the input signal power given and the APA model. In Fig. 3.13(b) the On/Off gain due to the signal–to–signal interactions, $G_{signals}$, as function of the signal wavelength is shown. Inspection of the figure shows that signals with higher wavelengths have a higher gain, and signals with a lower wavelength have a higher loss. This happens because signals with lower wavelength are amplifying signals with higher wavelength. Thus, the $G_{signals}$ has an opposite tilt, when compared with the input signal power.

Table 3.8: Pump powers used for trial 8 with provide a On/Off gain around 13 dB gain for the LEAF.

Pump Number	**Pump Powers (mW)**
P_1	333
P_2	262
P_3	273
P_4	179

To calculate the $G_{RFA}(s)$, we use the WAE model. Fig. 3.14(a) shows the On/Off gain predicted by the proposed model as function of the signal wavelength. Since this model does not allow us to consider the signal–to–signal interactions, the On/Off gain profile is flat. In Fig. 3.14(b), the On/Off gain of the transmission link as function of the signal wavelengths is shown. The results are obtained with the reference numerical model and by adding the $G_{signals}(s)$ to the On/Off gain estimated by WAE model $G_{RFA}(s)$. As we can see, the On/Off gain of the transmission system obtained with $G_{signals}(s) + G_{RFA}(s)$ is similar to the On/Off gain of the transmission link obtained with the reference numerical model.

Having the $G_{signals}(s)$, $G_{RFA}(s)$, and knowing the signal losses and the insertion losses of the RFA, we can calculate the output signal power. Fig. 3.15 shows the output signal power as function of the signals wavelengths, obtained with the reference numerical model and with the WAE model. Inspection of the figure shows that the

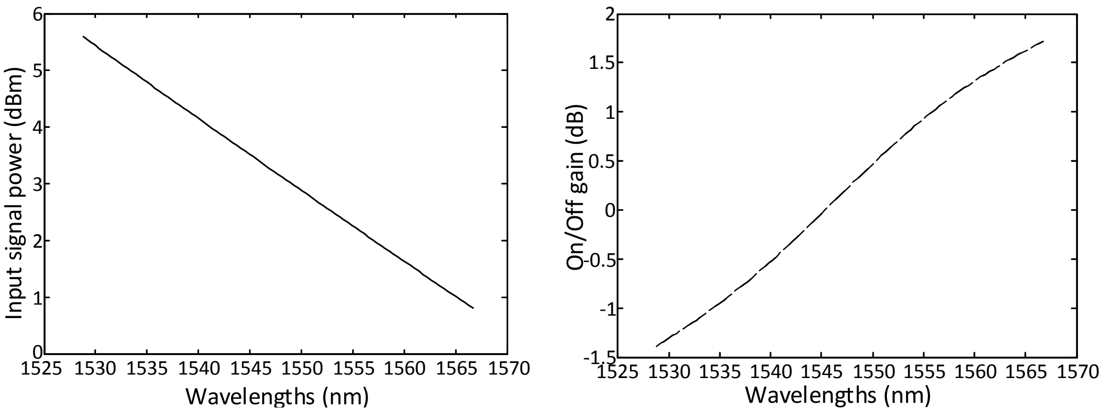

(a) (b)

Figure 3.13: a) Input signal power considered in trial 8. b) Simulated $G_{signals}$ at the end of the transmission link of trial 8.

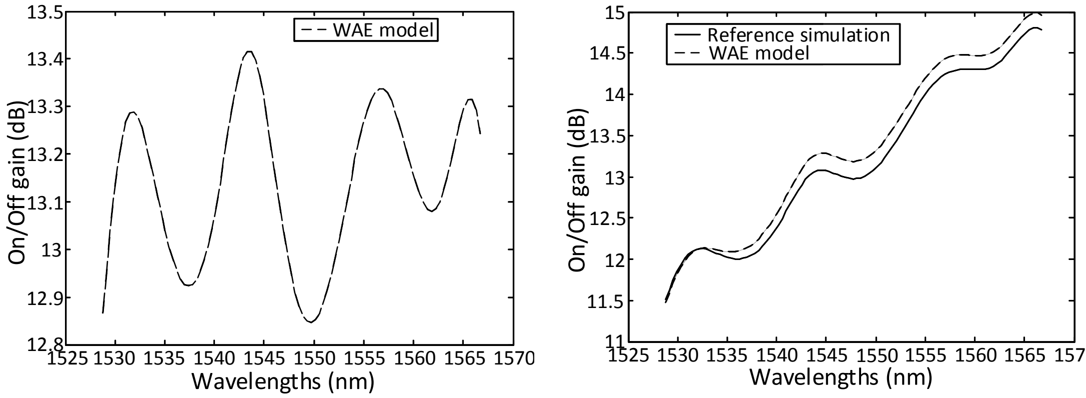

(a) (b)

Figure 3.14: a) Estimated On/Off gain using the WAE model for trial 8. b) Reference and estimated On/Off gain of the transmission link, trial 8.

---

reference numerical simulation presents an output signal power without any tilt. On the other hand, the proposed model does have some tilt. However, the difference between both is very small and with a maximum deviation in the order of 0.2 dB. When considering $G_{signals}(s)$ and $G_{RFA}(s)$ separately, we are introducing a possible source of error by neglecting the amplification of the signals and its impact on the $G_{signals}(s)$. However, as shown in the figure, the output signal power estimation is still accurate, when compared with the reference numerical model. Therefore, we verify that it is possible to use our approach the estimate the On/Off gain of the transmission link.

These steps are repeated for the other trials. Table 3.9 shows the maximum deviation between the WAE model and the reference numerical simulations when considering a SSMF fiber with a counter–pumped RFA with a gain of 10 dB. When comparing the

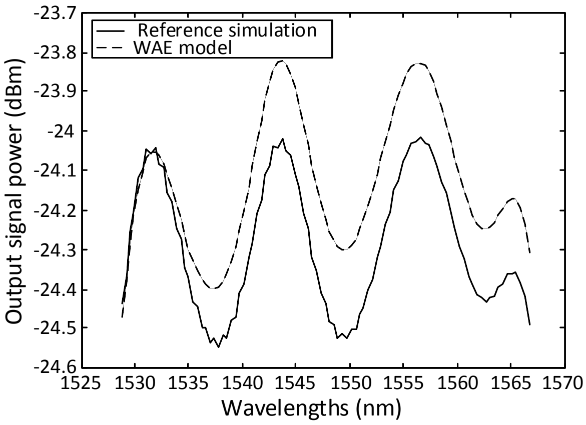

Figure 3.15: Output signal power obtained with the reference numerical model and estimated using the WAE model for trial 8.

results we can see that, despite the increase of distance and input signal power, the maximum deviation maintains a constant value below 0.4 dB, meaning that the proposed model is suitable for a higher range of signal powers and transmission distances. Table 3.10 shows the maximum deviation between the WAE model and the numerical simulations, regarding the use of a LEAF fiber with a counter–pumped RFA with a gain of 13 dB. From the results obtained, we verify that the deviation is below 0.5 dB. When increasing the transmission distance and the input signal power, we can see that the maximum deviation does not increase considerably for the LEAF fiber. When comparing both fibers, we verify that the LEAF fiber has a slightly higher error, which can be related to the fact that the amplifier gain is higher for this fiber. These results show that the model WAE can be used to estimate the output signal power for the considered trials.

Table 3.9: Maximum deviations of the output signal power between the reference numerical simulations and the WAE model for a SSMF transmission system with a counter–pumped RFA with 10 dB gain.

Trial	Distance (km)	Total loss (dB)	Signal (dBm)	Max. dev (dB)
1	91	20	-1.1	0.4
2	114	25	0.7	0.4
3	136	30	2.7	0.3
4	182	40	3.2	0.3

Table 3.10: Maximum deviations of the output signal power between the reference numerical simulations and the WAE model for a LEAF transmission system with a counter–pumped RFA with 13 dB gain.

Trial	Distance (km)	Total loss (dB)	Signal (dBm)	Max. dev (dB)
5	91	20	-1.1	0.5
6	114	25	0.7	0.3
7	136	30	2.7	0.3
8	182	40	3.2	0.2

Output ASE Noise Power Estimation

Let us estimate the output ASE noise power according to eq. (3.28), considering the conditions of trial 8. Fig. 3.16(a) shows the ASE noise input power as function of the ASE noise wavelength. We calculate ASE_{RFA} with the model presented in Section 3.2.5. By summing up all the terms according to eq. (3.28), it is possible to estimate the output ASE noise power.

Figure 3.16(b) shows the output ASE noise power as function of ASE noise the wavelength. The results are obtained with the reference numerical model and estimated using the proposed model. Inspection of the figure shows that there is a significant difference between the estimated ASE noise output power and the reference numerical model, higher than 2.5 dB. Despite the length of the transmission fiber, the difference is too high to be considered useful.

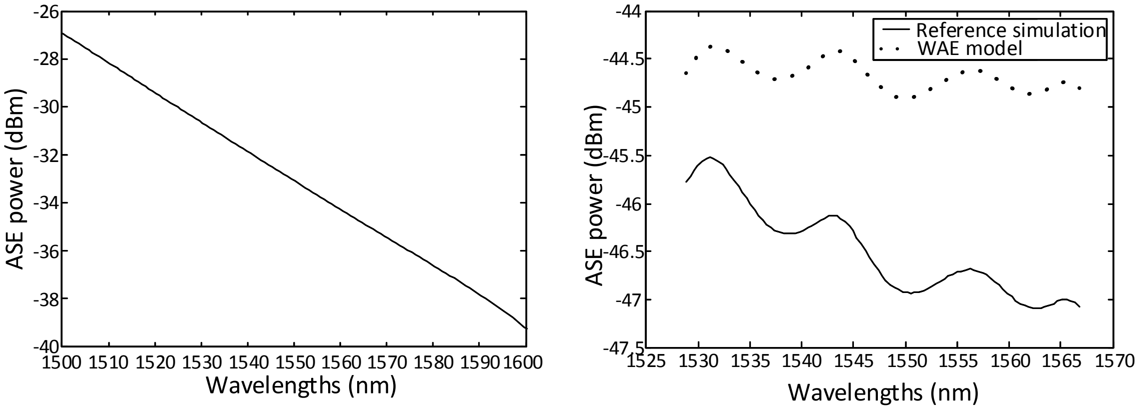

(a) (b)

Figure 3.16: a) Input ASE noise power of trial 8; b) Output ASE noise power of trial 8 obtained with the reference numerical model and estimated using WAE.

Let us perform the calculations for the other trials considered. Tables 3.11 and

Table 3.11: Maximum deviations of the ASE noise output power between the reference numerical simulations and the WAE for a SSMF transmission system with a counter–pumped RFA with 10 dB gain.

Trial	**Distance (km)**	**Total loss (dB)**	**Signal (dBm)**	**Max. dev (dB)**
1	91	20	-1.1	1.5
2	114	25	0.7	1
3	136	30	2.7	0.6
4	182	40	3.2	1.75

Table 3.12: Maximum deviations of the ASE noise output power between the reference numerical simulations and the WAE for a LEAF transmission system with a counter–pumped RFA with 13 dB gain.

Trial	**Distance (km)**	**Total loss (dB)**	**Signal (dBm)**	**Max. dev (dB)**
5	91	20	-1.1	1.1
6	114	25	0.7	0.6
7	136	30	2.7	0.9
8	182	40	3.2	2.7

3.12 show the maximum deviation obtained between the estimated ASE noise output power using the proposed model and the reference numerical model for the SSMF and LEAF, respectively. When observing both tables, between 114 km and 136 km the obtained results have a reduced deviation, which indicates that the accuracy of the model depends on the distance. Thus, it can be possible to tune the proposed model for the ASE noise with another parameter, dependent on the transmission distance, α_{adj}, to improve the accuracy of the model. Consequently, the net gain, G, is given by

$$G = \exp(-\alpha_{adj} L) \prod_i g_i. \tag{3.30}$$

This new parameter, α_{adj}, with units of dB/km, has to be carefully adjusted in order to accurately estimate the ASE noise output power in each trial. This adjustment needs to be based on experimental data or on a numerical model. Nevertheless, for each fiber type we can gather several results from trials with different transmission lengths and then perform a linear regression to the adjusted values obtained for α_{adj}. With this approach it is possible to estimate the ASE noise without the need of manually adjusting α_{adj}. Let us consider the SSMF trials 1, 2, 3, and 4 presented on Table 3.6. By comparing the ASE noise output power obtained with the proposed model against the reference numerical model, it is possible to adjust α_{adj}. Fig. 3.17 shows the manually adjusted α_{adj} obtained for trial 1, 2, 3, 4, as function of the fiber length of the SSMF. The obtained results for the trials considering the fiber length can be adjusted by a linear regression. In the case of the SSMF we obtain the following equation

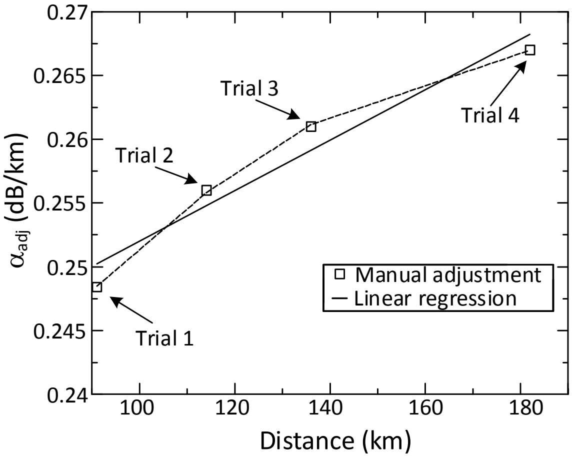

Figure 3.17: Manual adjustment of α_{adj} for the SSMF for the trial of Table 3.6. The line represent linear regression on the values α_{adj} for trial 1, 2, 3, and 4.

$$\alpha_{adj} = 0.23 + 1.97\text{x}10^{-7}L, \tag{3.31}$$

where L is the total length of the transmission fiber. Adopting a similar approach for the LEAF fiber, we obtain the following equation

$$\alpha_{adj} = 0.22 + 2.37\text{x}10^{-7}L. \tag{3.32}$$

With eqs. (3.31) and (3.32) it is possible to estimate the α_{adj} for these two fibers as function of the fiber length. Fig. 3.18(a) shows the ASE noise power for trial 8, using eq. (3.32) to estimate α_{adj}. We can see that now the ASE noise is properly estimated with a maximum deviation smaller than 0.8 dB. The use of a different attenuation coefficient for the fiber can be justified by the fact that we are over estimating the gain and, thus, the production of the ASE noise. Using the simulation results for adjusting α_{adj} is a valid approach since the RFA will be used in a reduced number of situations, and any variations in terms of signal powers and distances can be interpolated from these results. However, this process has to be performed for each fiber type to tune the ASE noise model. The α_{adj} parameter is introduced to estimate the ASE noise power, therefore there is no impact on the estimation of the amplifier On/Off gain.

Based on eqs. (3.31) and (3.32) we estimate the ASE noise output powers for the other trials and compare with the ASE noise output power obtained by the reference numerical model. Table 3.13 shows the maximum deviation between the estimated ASE noise power and the reference numerical simulations for the SSMF. As we can see, the maximum deviation between the numerical simulation and the estimated with the improved ASE noise model is below 0.7 dB. Table 3.14 shows the maximum deviation between the improved ASE noise model and the reference numerical model for the LEAF. The obtained results show a maximum deviation bellow 0.8 dB.

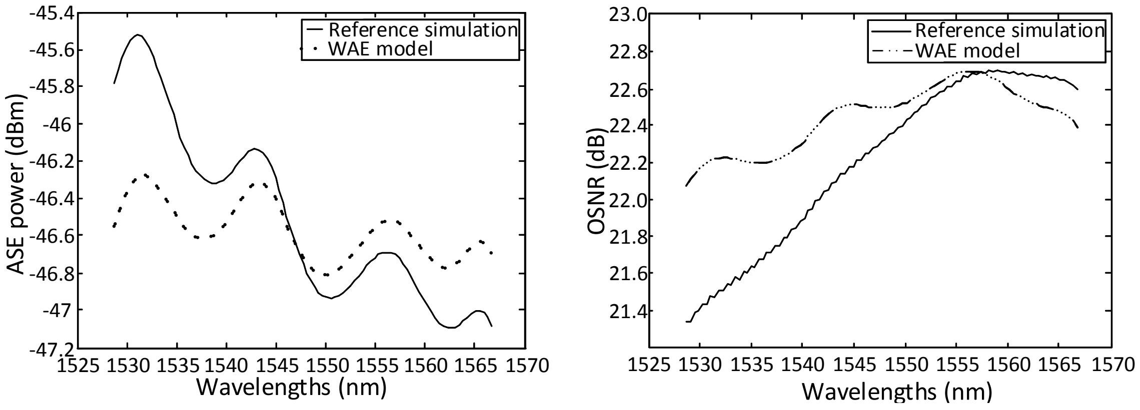

(a) (b)

Figure 3.18: a) ASE noise output power of trial 8 obtained with the improved ASE noise model and the reference numerical model; b) OSNR at the end of the transmission link of trial 8 obtained with the simplified model and the reference numerical model.

Table 3.13: Maximum deviations for the ASE noise output power between the reference numerical simulations and the WAE with improved ASE noise estimation for a SSMF transmission system with a counter–pumped RFA with 10 dB gain.

Trial	Distance (km)	Total loss (dB)	Signal (dBm)	Max. dev (dB)
1	91	20	-1.1	0.6
2	114	25	0.7	0.7
3	136	30	2.7	0.6
4	182	40	3.2	0.6

3.3.4 OSNR Estimation When Considering the Propagation of WDM Signals

After estimating the output signal power and the output ASE noise power for each signal, it is possible to calculate the OSNR at the end of the transmission link. The OSNR is given by

Table 3.14: Maximum deviations for the ASE noise output power between the reference numerical simulations and the WAE with improved ASE noise estimation for a LEAF transmission system with a counter–pumped RFA with 13 dB gain.

Trial	**Distance (km)**	**Total loss (dB)**	**Signal (dBm)**	**Max. dev (dB)**
5	91	20	-1.1	0.5
6	114	25	0.7	0.7
7	136	30	2.7	0.8
8	182	40	3.2	0.8

$$OSNR = 10\log_{10}\left(\frac{P_{out}(s)}{P_{ase,out}(a)}\right) \tag{3.33}$$

Therefore, using trial 8 as an example, Fig. 3.18(b) shows the OSNR at the end of the transmission link obtained with the reference numerical model and when estimating with the proposed model. When comparing with the OSNR obtained by the reference numerical model we can see that the maximum deviation is 0.77 dB and the MAE is 0.3 dB. These values are within the considered limits of 1 dB.

We perform the calculations for all the other trials. Table 3.15 shows the maximum deviation and the MAE when comparing the proposed model with the reference numerical model. As we can see, the OSNR at the end of the transmission link is estimated with a maximum deviation of 0.4 dB and a MAE of 0.18 dB. When observing the increase of the input signal power and distance, we can notice that the variation is not significant and the results are still accurate. These errors are smaller than the output signal power and the output ASE noise power estimation maximum deviation individually, since both estimations have a deviation which is related to the gain of the amplifier. Regarding the OSNR deviations when considering the LEAF fiber, Table 3.16, we verify that the errors are slightly higher than when comparing with the SSMF fiber, with a maximum deviation of 0.8 dB and a MAE below 0.4 dB.

We are also interested in changing the input signal power and inferring the impact on the OSNR estimation when considering the same distance. Therefore, two extra simulations with -2 dBm and 2 dBm of input signal power for a SSMF with a distance of 114 km are simulated. Table 3.17 shows the obtained results. When comparing trial 2 with trials 9 and 10 we can see that, despite a significant change in input signal power, the error when estimating the OSNR has negligible influence.

By comparing these trials, we show that using the WAE model to estimate the OSNR of WDM signals provides accurate results. Thus, when using the WAE model,

Table 3.15: OSNR maximum deviation and medium absolute error between the numerical simulations and the WAE model for a SSMF transmission system with a counter–pumped RFA with 10 dB gain.

Trial	**Distance (km)**	**Signal (dBm)**	**MAE (dB)**	**Max. dev (dB)**
1	91	-1.1	0.11	0.22
2	114	0.7	0.14	0.3
3	136	2.7	0.16	0.35
4	182	3.2	0.18	0.38

Table 3.16: OSNR maximum deviation and medium absolute error between the numerical simulations and the WAE model for a LEAF transmission system with a counter–pumped RFA with 13 dB gain.

Trial	**Distance (km)**	**Signal (dBm)**	**MAE (dB)**	**Max. dev (dB)**
5	91	-1.1	0.21	0.50
6	114	0.7	0.26	0.55
7	136	2.7	0.37	0.73
8	182	3.2	0.30	0.76

the OSNR at the end of the transmission link can be estimated in a reduced time interval without increasing the processing time of the planning tool.

3.4 Efficient Algorithm for Designing Broadband RFAs

In a near future it will be possible to adjust in real time several characteristics of the RFAs, such as number of pumps, pump wavelengths, and powers. This feature will allow to optimize the amplifier gain according to the characteristics of the transmission link, such as the number and input power of signals, in the case of network reconfigurations or end of life planning. Therefore, it is important to search for algorithms to design RFAs with low computational requirements, suitable for implementation on the control layer of the amplification element. However, this is a complex problem, because the propagation equations do not have an analytical solution and the search for optimal solutions depends on several parameters, such as number of pumps, pump powers and wavelengths, fiber length, and fiber type. Thus, developing an algorithm to enable a fast search for the solution which minimizes the gain ripple is important.

Table 3.17: OSNR maximum deviation and MAE between the reference numerical simulations and the WAE model for a SSMF transmission system with a counter–pumped RFA with 10 dB gain.

Trial	Distance (km)	Signal (dBm)	MAE (dB)	Max. dev (dB)
9	114	0	0.15	0.33
10	114	3	0.13	0.29

There are several heuristics to search for the optimized configuration for the pumps wavelengths and powers, such as simulated annealing algorithm, genetic algorithm (GA) and neural networks algorithm [32, 33]. In each of these approaches, the solutions given by the heuristics have to be tested until a solution that minimizes the objective function is found. Thus, for each attempt, it is necessary to numerically simulate the power evolution for the pump wavelengths in the RFA, which is time consuming. On the other hand, as discussed in Section 3.1, in order to implement analytical models for the RFA, some approximations, such as neglecting the pump–to–pump interactions, have to be considered. However, as shown in [23], the pump–to–pump interactions are an important effect as the number of pumps and the pump power increases, meaning that it is mandatory to include the pump–to–pump interactions in the model for a broadband RFA. In order to account for this effect and estimate the On/Off gain of the RFA we propose the use of the simplified model developed, the WAE model.

3.4.1 Optimization Method

From all the available heuristics we will use the GA, since it is very efficient when the solution space is significantly large and the function is highly non–linear [33]. The GA is a heuristic based on the theory of natural evolution and has the following steps: generation of an initial population, encoding, evaluation, selection, crossover, mutation, and decoding [33]. The GA modifies a set of solutions from the initial population repeatedly, in an attempt to improve the set in each iteration. In general, the fittest individuals of any population are used to crossover, giving rise to next generation (offspring). To increase the population diversity, mutations can also be applied. GAs have been shown to solve linear and nonlinear problems by exploring all regions of the state space and exponentially exploiting promising areas through mutation, crossover and selection operations applied to individuals in the population.

We want to design a flat gain RFA for a desired gain given by the user. Since we will use a GA to minimize only one objective function, we selected the MSE function between the estimated gain and the desired gain. We use the MSE function because it squares the gain deviations, giving more weight to wavelengths with higher deviation. Therefore, the GA will try to decrease the difference between the higher and the lower gain of the RFA. In this case, the MSE is given by

$$MSE = \frac{1}{M}\sum_{i=1}^{M}(x_i - \hat{x}_i)^2, \tag{3.34}$$

$$x_i = F_i(\lambda_1, ..., \lambda_N, P_1, ..., P_N), \tag{3.35}$$

where x_i is the gain for the channel i and $\hat{x}_i$ is the intended gain of the RFA in decibels, and M is the number of channels. In eq. (3.35), F_i is the propagation function, which in this case can be the DNM, or the simplified model which is the WAE model.

3.4.2 Benchmark Between the APA Model and the WAE

Without loss of generality, we intend to design a counter–pumped RFA with four pumps, to provide an average gain of 10 dB with the lowest possible ripple for the extended C band, ranging from 1530 nm to 1595 nm. The maximum pump power of each pump is limited to 500 mW. We choose seven channels at different wavelengths in the extended C band to test the solutions given by the GA. They are centered at 1531 nm, 1541 nm, 1551 nm, 1561 nm, 1571 nm, 1581 nm, and 1591 nm. This optimization problem has eight variables, divided in four pump wavelengths and four pump powers.

After the optimization process, we analyze the gain ripple deviation, which is the difference between the maximum gain and the minimum gain. Since we are using 4 pumps, we consider that the obtained solutions are acceptable when the gain ripple is smaller than 1.3 dB [34].

We use an initial population size of 300, and the termination criterion is the number of generations, in this case 20 generations. The options used for the GA are based on [32]. The considered counter–pumped RFA has 150 km of SSMF, with an attenuation of 0.25 dB/km for wavelengths smaller than 1450 nm, 0.23 dB/km for wavelengths from 1450 nm to 1500 nm and 0.2 dB/km for wavelengths higher than 1500 nm. Since we are not interested in accounting for the signal–to–signal interactions, the signals have an input power of -13.8 dBm. The computer used for these simulations is an Intel T5500 processor at 1.66 GHz with 2 GB of RAM.

When using the GA with APA numeric model to solve the propagation equations for 4 pumps and 7 signals, we verify that the optimization program takes more than 9 minutes to calculate 20 generations and minimize the objective function. The obtained gain ripple is 1.2 dB for the extended C band. Fig. 3.19 shows the obtained solutions for the pump powers and wavelengths, and the amplifier On/Off gain, $G_{\mathrm{On/Off}}$, as a function of the signal wavelength.

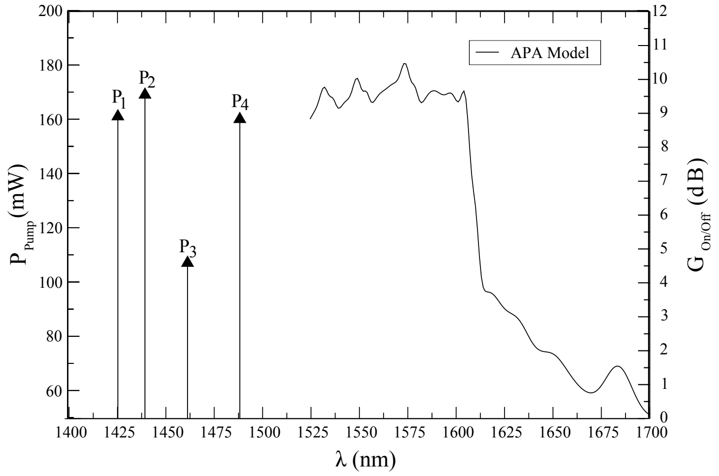

Figure 3.19: On/Off gain as function of the signal wavelength obtained for RFA using the GA with the APA model. The pump powers and wavelengths used are also shown.

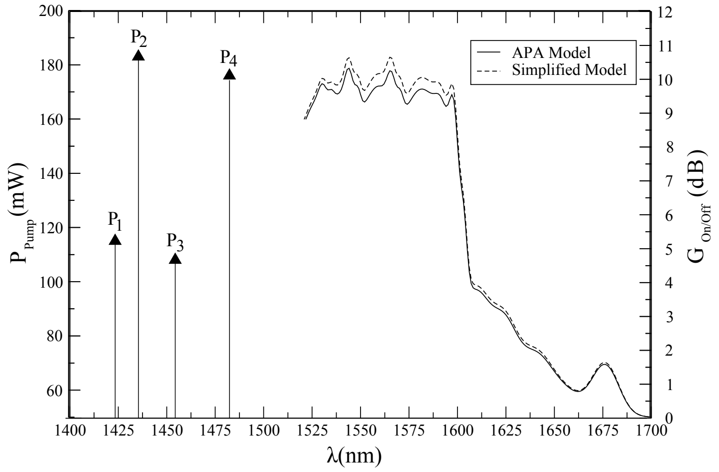

Figure 3.20: On/Off gain as function of the signal wavelength obtained for RFA using the GA with the simplified model, WAE, and the comparison with the gain given by the APA model using the same pump powers and wavelengths.

When using the GA with the simplified model, WAE model, we verify that a solution is obtained in less than 8 seconds, and the achieved ripple for the simplified model is 1.1 dB, see Fig. 3.20. To validate the accuracy of the solution given by the simplified model, we use the pump powers and wavelengths provided by the simplified approach and simulate the amplifier with the APA model. The results obtained with the APA model are presented in the same figure. We verify that the ripple obtained with the APA model is about 1.2 dB, which is very similar to the one given by the simplified model. Similar results are obtained for other configurations with different number of pumps, fiber lengths and number of signals. Thus, the simplified model provides a solution with good accuracy.

3.5 Conclusions

In this chapter, a novel model to estimate the On/Off gain and ASE noise of a transmission link with RFA amplification with multiple pumps was proposed. This model is based on a customization of the undepleted pump power model with two extra parameters, D_{int} and α_{SRS}, to account for the pump–to–pump interactions. Two methods were proposed to adjust these parameters, one based on the comparison with experimental data or detailed numerical simulations, WBC, and the other based on analytical expressions, WAE. The second method is simpler to implement, because it can be used without comparison with experimental or numerical simulations. When comparing the WAE with experimental measurements and detailed numerical simulations, we found that this model provides accurate results for a total input pump power of up to 900 mW, a wavelength separation of up to 60 nm between pumps, and a transmission distance of up to 180 km. The WAE model presents an improved computational processing performance without losing significant accuracy for the most used pump configurations. In fact, it was verified that the model can be more than 70 times faster than the DNM.

We used the proposed WAE model to estimate the OSNR of WDM signals at the transmission link with a counter–pumped RFA, when considering different fiber types, fiber lengths and input signals powers. The obtained results were compared with the results obtained by a reference numerical model. From the comparison between both, we verified that the On/Off gain was properly estimated. However, the accuracy of the ASE noise power estimation was not enough. To overcome this, an extra parameter α_{adj} was introduced to adjust the estimation of the ASE noise output power. With the introduction of this parameter, we verified that the proposed model estimates the OSNR of the WDM signals at the end of the transmission link with a good accuracy. Thus, the proposed simplified model can be implemented in planning tools, providing an accurate estimation of the OSNR, without increasing the computational requirements of the tool.

We also presented an efficient algorithm to design counter–pumped RFA with low computation requirements. To minimize the gain ripple of the RFA, we implemented a GA to search for the quasi–optimum solutions for the pump powers and wavelengths, and used the APA model or the WAE model to simulate the signal propagation. The goal of the task was to assess how much time can be saved if the WAE model is used to estimate the gain of the amplifier. Therefore, the properties of the GA were not investigated and were the same for both trials. We verified that the APA model took more than 9 minutes to find a solution. On the other hand, the WAE only took 8 seconds, meaning that a solution was found more than 50 times faster than when using the APA model, with a similar ripple to the one obtained for with the APA model. Thus, the proposed algorithm is suitable for designing RFAs in systems with computational constraints.

References

[1] A. Morea, T. Zami, and F. Leplingard, “Importance of reliability when dimensioning an optical transparent network with physical impairments awareness,” in *Proc. International Conference on Transparent Optical Networks (ICTON)*, Jun. 2009, p. Mo.C4.2.

[2] A. Morea, N. Brogard, F. Leplingard, J. Antona, T. Zami, B. Lavigne, and D. Bayart, “QoT function and A* routing: an optimized combination for connection search in translucent networks,” *OSA Journal of Optical Networking*, vol. 7, no. 1, pp. 42–60, Jan. 2008.

[3] S. Norimatsu and M. Maruoka, “Accurate Q-factor estimation of optically amplified systems in the presence of waveform distortions,” *IEEE/OSA Journal of Lightwave Technology*, vol. 20, no. 1, pp. 19–27, Jan. 2002.

[4] B. Ramamurthy, D. Datta, H. Feng, J. Heritage, and B. Mukherjee, “Impact of transmission impairments on the teletraffic performance of wavelength-routed optical networks,” *IEEE/OSA Journal of Lightwave Technology*, vol. 17, no. 10, pp. 1713–1723, Oct. 1999.

[5] S. Pachnicke, N. Luck, and P. Krummrich, “Novel physical-layer impairment-aware routing algorithm for translucent optical networks with 43 Gb/s and 107 Gb/s channels,” in *Proc. International Conference on Transparent Optical Networks (ICTON)*, Jun. 2009, p. Tu.A3.6.

[6] E. Rouzic, “Physical impairment awareness in the context of an operator infrastructure,” in *Proc. International Conference on Photonics in Switching*, Sep. 2009, pp. 1–4.

[7] S. Pachnicke, T. Paschenda, and P. Krummrich, “Physical impairment based regenerator placement and routing in translucent optical networks,” in *Proc. Optical Fiber Communication Conference (OFC)*, Feb. 2008, p. OWA2.

[8] K. Manousakis, K. Christodoulopoulos, E. Kamitsas, I. Tomkos, and E. Varvarigos, “Offline impairment-aware routing and wavelength assignment algorithms in translucent WDM optical networks,” *IEEE/OSA Journal of Lightwave Technology*, vol. 27, no. 12, pp. 1866–1877, Jun. 2009.

[9] S. Pasqualini, A. Kirstadter, A. Iselt, R. Chahine, S. Verbrugge, D. Colle, M. Pickavet, and P. Demeester, “Influence of GMPLS on network providers operational expenditures: a quantitative study,” *IEEE Communications Magazine*, vol. 43, no. 7, pp. 28–38, Jul. 2005.

[10] R. Martinez and C. Pinart, “Challenges and requirements for introducing impairment-awareness into the management and control planes of ASON/GMPLS WDM networks,” *IEEE Communications Magazine*, vol. 44, no. 12, pp. 76–85, Dec. 2006.

[11] T. Zami, A. Morea, F. Leplingard, and N. Brogard, “The relevant impact of the physical parameters uncertainties when dimensioning an optical core transparent network,” in *Proc. European Conference on Optical Communication (ECOC)*, vol. 3, Sep. 2008, p. We.3.D.2.

[12] F. Leplingard, T. Zami, A. Morea, N. Brogard, and D. Bayart, “Determination of the impact of a quality of transmission estimator margin on the dimensioning of an optical network,” in *Proc. Optical Fiber Communication Conference (OFC)*, Feb. 2008, p. OWA6.

[13] J. Ferreira, R. Nogueira, P. Monteiro, and A. Pinto, “Raman amplifier undepleted pump model customization to include pump-to-pump interactions,” in *Proc. Conference on Computer as a Tool (EUROCON)*, no. 1, Apr. 2011, pp. 1–4.

[14] J. Ferreira, R. Nogueira, P. Monteiro, and A. Pinto, “Weighted undepleted pump model for broadband counter-pumped Raman fiber amplifiers,” *IEEE/OSA Journal of Optical Communications and Networking*, vol. 4, no. 8, pp. 595–602, Aug. 2012.

[15] J. Ferreira, D. Fonseca, P. Monteiro, and A. Pinto, “Efficient algorithm for designing broadband Raman fiber amplifiers,” in *Proc. Conference on Telecommunications (ConfTele)*, May 2013, pp. 1–4.

[16] C. Headley and G. Agrawal, *Raman amplification in fiber optical communication systems.* Academic press, 2005.

[17] M. Zirngibl, "Analytical model of Raman gain effects in massive wavelength division multiplexed transmission systems," *IET Electronics Letters*, vol. 34, no. 8, pp. 789–790, Apr. 1998.

[18] B. Min, W. Lee, and N. Park, "Efficient formulation of Raman amplifier propagation equations with average power analysis," *IEEE Photonics Technology Letters*, vol. 12, no. 11, pp. 1486–1488, Nov. 2000.

[19] J. Park and P. Kim, "Closed integral form expansion of Raman equation for efficient gain optimization process," *IEEE Photonics Technology Letters*, vol. 16, no. 7, pp. 1649–1651, Jul. 2004.

[20] J. Park and P. Kim, "Gain and noise figure spectrum control algorithm for fiber Raman amplifiers," *IEEE Photonics Technology Letters*, vol. 18, no. 10, pp. 1125–1127, May 2006.

[21] S. Chinn, "Analysis of counter-pumped small-signal fibre Raman amplifiers," *IET Electronics Letters*, vol. 33, no. 7, pp. 607–608, Mar. 1997.

[22] X. Zhou, C. Lu, P. Shum, and T. Cheng, "A simplified model and optimal design of a multiwavelength backward-pumped fiber Raman amplifier," *IEEE Photonics Technology Letters*, vol. 13, no. 9, pp. 945–947, Sep. 2001.

[23] N. Cani, L. Calmon, M. Pontes, M. Ribeiro, M. Segatto, and A. Cartaxo, "An analytical approximated solution for the gain of broadband Raman amplifiers with multiple counter-pumps," *IEEE/OSA Journal of Lightwave Technology*, vol. 27, no. 7, pp. 944–951, Apr. 2009.

[24] J. Zhou, J. Chen, X. Li, and W. Jiang, "A novel algorithm for backward-pumped Raman amplifier," *Fiber and Integrated Optics*, vol. 24, no. 6, pp. 529–535, Nov. 2005.

[25] M. Santagiustina, "Exact, implicit, integral solution of depletion and saturation in Raman and Brillouin fiber amplifiers," in *Proc. Lasers and Electro-Optics (CLEO)*, Jun. 2007, p. 1.

[26] S. Namiki and Y. Emori, "Ultrabroad-band Raman amplifiers pumped and gain-equalized by wavelength-division-multiplexed high-power laser diodes," *IEEE Journal of Selected Topics in Quantum Electronics*, vol. 7, no. 1, pp. 3–16, Jan. 2001.

[27] M. Fugihara and A. Pinto, "Low-cost L-band Raman amplifier for CWDM systems," in *Proc. IEEE/LEOS Summer Topical Meetings*, Jul. 2008, p. ME2.3.

[28] M. Fugihara and A. Pinto, "Low-cost Raman amplifier for CWDM systems," *Microwave and Optical Technology Letters*, vol. 50, no. 2, pp. 297–301, Dec. 2008.

[29] C. Fludger, V. Handerek, N. Jolley, and R. Mears, “Fundamental noise limits in broadband Raman amplifiers,” in *Proc. Optical Fiber Communication Conference (OFC)*, Mar. 2001, pp. MA5/1–MA5/3.

[30] N. Muga, M. Fugihara, M. Ferreira, and A. Pinto, “Non-gaussian ASE noise in Raman amplification systems,” *IEEE/OSA Journal of Lightwave Technology*, vol. 27, no. 16, pp. 3389–3398, Aug. 2009.

[31] P. Krummrich, R. Neuhauser, and C. Glingener, “Bandwidth limitations of broadband distributed Raman fiber amplifiers for WDM systems,” in *Proc. Optical Fiber Communication Conference (OFC)*, Mar. 2001, p. MI3.

[32] B. Neto, A. Teixeira, N. Wada, and P. André, “Efficient use of hybrid genetic algorithms in the gain optimization of distributed Raman amplifiers,” *Optics Express*, vol. 15, no. 26, pp. 17 520–17 528, Dec. 2007.

[33] D. Goldberg, *Genetic algorithms in search, optimization, and machine learning.* Addison-Wesley, 1989.

[34] X. Liu and B. Lee, “Effective shooting algorithm and its application to fiber amplifiers,” *OSA Optics Express*, vol. 11, no. 12, pp. 1452–1461, Jun. 2003.

Chapter 4

Energy Efficient RFA Configuration

Given the extensively growing demand for traffic, the amount of energy required to operate optical networks cannot be overlooked. Therefore, future communication networks should have the ability to support an enormous amount of bandwidth in an energy efficient way. This problem should be address not only at the planning level, but also at the component level. By increasing the efficiency of amplifiers, we can contribute to reduce the power consumption of optical networks. However, the proposed solutions have to be compatible with transparent and dynamic optical networks.

In this chapter we study and investigate the steady–state and the dynamic regime of an energy efficient Raman fiber amplifier (RFA) named pump–reflecting RFA. Afterwards, a mitigation technique to control the dynamic response of the amplifier due to channel add/drop is proposed. This work was published in [1, 2] and also a patent was granted for the mitigation technique presented in Section 4.4 [3].

4.1 Introduction

Considering the optical fiber amplifiers, there are already solutions to increase the efficiencies of the erbium–doped fiber amplifier (EDFA) and RFA [4–7]. Regarding RFAs, the amplification medium is usually the transmission fiber itself or, sometimes, a dispersion compensating fiber (DCF) used in the transmission system. This means that usually the amplifier is not designed to take advantage of all the injected pump power, specially when using DCF, because the fiber length is short. Therefore, several solutions were proposed in order to increase the RFA efficiency. For example, in [7, 8], the authors use the remaining pump power to pump an EDFA. Another solution is proposed in [4], where a fiber–Bragg grating (FBG) or a fiber–mirror reflector (FMR), positioned at the opposite side of the pump, with a peak reflectivity at the pump wavelength, is used to reflect the remaining pump power back into the amplifier. The amplifier becomes bidirectionally pumped, but using only one pump. This configuration is analyzed in [9] in the steady–state regime and it is concluded that this pumping scheme increases the amplifier efficiency by increasing the gain of the amplifier. Thus, in order to obtain the same gain as in conventional configurations, it allows a reduction in the required pump power, improving important parameters such as the optical signal–to–noise ratio (OSNR). However, with the development of dynamic optical networks, channels add/drop will occur in the transmission link and at the input of the amplifier, and, due to that, power fluctuations of the surviving channels will occur at the output of the RFA. Regarding these power fluctuations, previous work concluded that the transient effect in RFA occurs due to the combination of two phenomena [10]. There is a small but fast response due to signal–to–signal Raman crosstalk, which can either increase or decrease the signal power of the surviving channel, depending on the relative position of the add/drop channel. There is also a larger and slower response due to pump readjustments, which occurs on a time scale determined by the length of the amplifier.

An analytical study of the transient phenomenon attributable to the input power variation in a RFA is presented in [11]. In [12], the authors studied the influence of some parameters, such as the pump powers, signal input powers, and different fiber lengths on the transient response of a counter–pumped RFA. In [13], the transients in co–pumped and counter–pumped RFAs are investigated. It is shown that the transient effect in a co–pumped RFA is more pronounced and faster than in a counter–pumped amplifier. In [14] the authors analyzed the transient effect in a bidirectional amplifier, with two independent pumps, and they concluded that the use of a low power forward pump allows the improvement of the overall static and dynamic performance of the amplifier.

Transient effects due to input power variation, known as power transients [15], in RFA can be mitigated using several techniques, such as dummy channels (to replace the dropped channels), all–optical–gain–clamped (AOGC) [16–18] and pump–controlled gain–clamping system [19, 20]. When using dummy channels, at the dropping event, extra lasers are activated in order to minimize the power drop along the fiber. By doing this, the pump fluctuations are reduced and the impact on the surviving channels is minimized. However, since extra channels need to be injected into the amplifier, the cost will increase.

When considering AOGC, there are two methods to implement this mitigation technique. The first method is based on the re–injection of a percentage of a chosen wavelength back into the amplifier, forming a fiber ring [18, 21]. The second technique is based on using two FBG tuned at a selected wavelength [16, 17], creating a resonant optical cavity. The selected wavelength does not carry any information and, due to the successive reflections inside of the transmission fiber, its power will increase by consuming pump power until a stationary regime is reached. In a dropping event, when properly tuned, the selected channel will consume the extra gain of the amplifier, and the surviving channels will experience smaller power fluctuations. The selected channel does not need to be a laser, since it is possible to use an amplified spontaneous emission (ASE) noise wavelength to construct the optical feedback system. Performing this will avoid the need of including more lasers in the system, which would increase the amplifier cost. One major disadvantage of AOGC is the restriction of the amplifier gain, since the selected channel will consume optical power from the pump and, consequently, reduce the efficiency of the amplifier [20].

Another transient mitigation technique is the pump–controlled gain–clamping system [19, 20]. The transient control can be accomplished using photodiodes to monitor the behavior of the amplifier, and a processing system together with an actuator to control the pump power. The monitoring can be performed by measuring the total signal input power of the transmission system or by using one or more probe channels. Note that the signals that are being monitored cannot be removed from the transmission link, limiting the network reconfiguration. The information retrieved from the monitoring channels can be used in an algorithm in order to directly control the pump power. When the power of a surviving channel or a probe channel increases, the control system decreases the pump power, in order to compensate for the increase in gain caused by the removal of signals. This contributes for the surviving signal to fluctuate as little as possible. The same is valid when signals are added. A disadvantage of this system is the response time. In fact, between reading a fluctuation and controlling the transient response, a few milliseconds can elapse. This time interval can be unacceptable, specially when implementing this technique in a co–propagating amplifier, since the rise time of the surviving channels in co–pumped amplifiers is much smaller than the counter–pumped RFA [22]. On the other hand, it is noticed that an increase in the number of pumps and signals leads to more complex mitigation mechanisms, because more monitoring channels and more complex algorithms are needed in order to effectively mitigate power fluctuations in surviving channels. An advantage of this method is that the technique does not restrict gain, thus allowing a higher efficiency of the amplifier. The disadvantage of this control system is the increased amplifier cost, caused by the requirement of extra devices to retrieve information from the amplifier and adjust the pump power.

This chapter is organized as follows. In Section 4.2, we experimentally implement the pump–reflecting RFA and observe an increase on the gain of the amplifier, although associated with an increase in the transient response. In Section 4.3, we analyze numerically, using the model described in Section 2.3.3, the dynamic behavior of a pump–reflecting RFA and assess the impact of reflecting the pump power back into the amplifier on the surviving channels transient response. The dependence of the transient response on the RFA configuration, pump power and distance is further discussed. In order to implement a low cost solution to mitigate the transient effect, in Section 4.4 we propose a new approach to implement a pump–controlled gain–clamping system, taking advantage of the amplifier configuration. The proposed mitigation technique is validated numerically and experimentally. Following this approach, an efficient low–cost RFA, suitable for dynamic optical networks, is obtained. The conclusions of this chapter are presented in Section 4.5.

4.2 On/Off Gain and Dynamic Response

In order to investigate the increase in efficiency and the dynamic regime of the pump–reflected RFA when compared with the conventional counter–pumped RFA, we experimentally implemented a counter–pumped RFA with 4 pumps. Fig. 4.1 shows the schematic diagram with the experimental setup to be implemented. Since it is expensive to implement four FBG centered at each pump wavelength when testing the pump–reflecting RFA, we choose to implement a FMR with 99% of reflection between 1420 nm and 1490 nm. Whenever we want to test the conventional counter–pumped RFA, we remove the FMR, and connect an optical isolator (ISO).

In the case of the pump–reflecting counter–pumped amplifier, all of the unused pump power will be reflected back at the beginning of the amplifier fiber, meaning that the extra pump power will be re–injected into the amplifier. The circulator is used in the pumps path in order to avoid any damage to the pumps and also, by connecting the output 3 to a photo–diode, to monitor the pump behavior in the dynamic regime. Since in this case we are interested in measuring the increase in gain due to the reflection of the pump power when compared with the conventional counter–pumped RFA, we will use the same input pump power for each pump in both configurations. The pumps used for this experiment are centered at 1426 nm, 1444 nm, 1462 nm, and 1487 nm with 167.5 mW, 106.7 mW, 48.9 mW, and 134 mW of input pump power, respectively. The

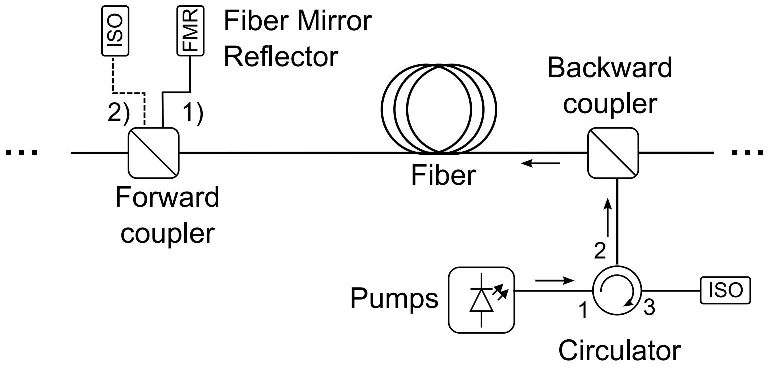

Figure 4.1: Schematic diagram of the 1) pump–reflecting RFA, and 2) conventional counter–pumped RFA.

fiber used is a 40 km length standard single mode fiber (SSMF), with an effective area of 80 μm^2 and with an attenuation coefficient of 0.25 dB/km at the pump wavelengths centered at 1426 nm and 1444 nm and 0.23 dB/km for the rest of the pumps. The attenuation coefficient for the signals is 0.20 dB/km.

Depending of the type of measurement, On/Off gain or dynamic response due to channel add/drop, different devices need to added to the setup.

4.2.1 Measurement of the On/Off Gain

To study the gain increase due to the reflection of the pump powers, we experimentally compared the behavior of the pump–reflecting RFA with the conventional counter–pumped RFA. Fig. 4.2 shows a schematic diagram of the experimental setup implemented to measure the amplifier On/Off gain of a conventional counter–pumped RFA, and of the pump–reflecting RFA using the same pump powers. A laser tunable between 1515 nm and 1610 nm, with an input signal power of 0 dBm is used to measure the On/Off gain of the amplifier. The channel output power is measured with an optical spectrum analyzer (OSA).

Figure 4.3 shows the measured On/Off gain as function of the signal wavelength for the conventional counter–pumped RFA, and for the pump–reflecting RFA when using the same pump powers. By including the FMR in the amplifier, the gain of the amplifier increases in more than 1 dB when compared with the conventional counter–pumped RFA. Since the pump powers are the same for both configurations, we confirm that, by reflecting the pump power, the efficiency of the amplifier in the steady–state regime is increased.

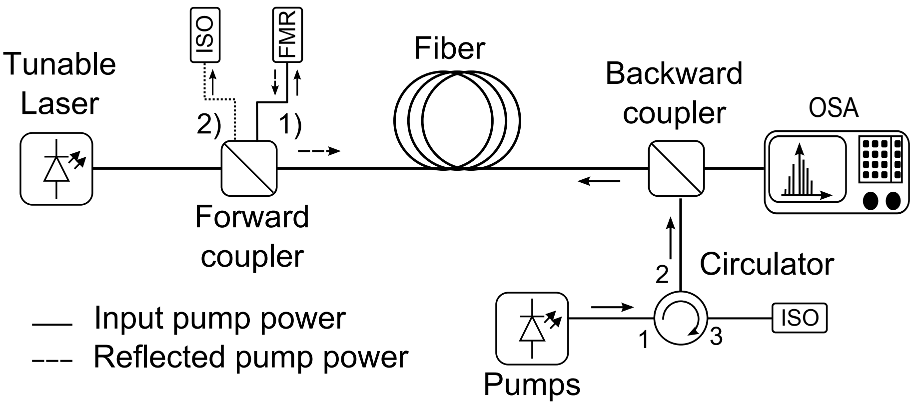

Figure 4.2: Schematic diagram of the experimental setup implemented to measure the amplifier On/Off gain of 1) the counter–pumped RFA, 2) the pump–reflecting RFA.

4.2.2 Measurement of the Dynamic Response

In order to measure the dynamic response of the pump–reflecting pumping scheme and the conventional counter–pumped RFA we need to include the addition or the removal of several channels. In this case we use an add/drop channel with a higher power than the surviving channel, in order to emulate the drop of two channels. Fig. 4.4 shows a schematic diagram of the setup implemented to study the dynamic regime. We implemented two signals, S_1, centered at 1551 nm with 1.6 dBm of input optical power, and S_2, centered at 1601 nm with 4.5 dBm of input optical power. The signal S_2 is a square wave modulated with 250 Hz of frequency to reproduce the channel add/drop. The fiber and the pump powers used are the same as stated before. An optical filter centered at the signal wavelength, S_1, is implemented before the oscilloscope (OSC). Again, to switch between the conventional RFA and the pump–reflecting RFA, we need to change the ISO for the FMR. The oscilloscope is used to measure the surviving channel power deviations and the reflected pump power deviations, when the amplifier configuration is the pump–reflecting RFA. Since we are interested in improving the gain of the amplifier, we use the same pump power, both with and without the pump reflection.

Figure 4.5(a) shows the surviving channel gain deviation, channel S_1, as function of time, when channel S_2 is add/drop, with and without the reflection of the pumps. The drop of channel S_2 occurs at 0 ms and the add at 2 ms, and it is repeated periodically. The surviving channel transient response does not start at 0 ms, but rather presents a delay around 193 μs, due to the propagation time of signals along the fiber. An analysis of the figure shows that the gain deviation of the pump–reflecting RFA is 20 % higher when compared with conventional counter–pumped RFA configuration. Fig. 4.5(b)

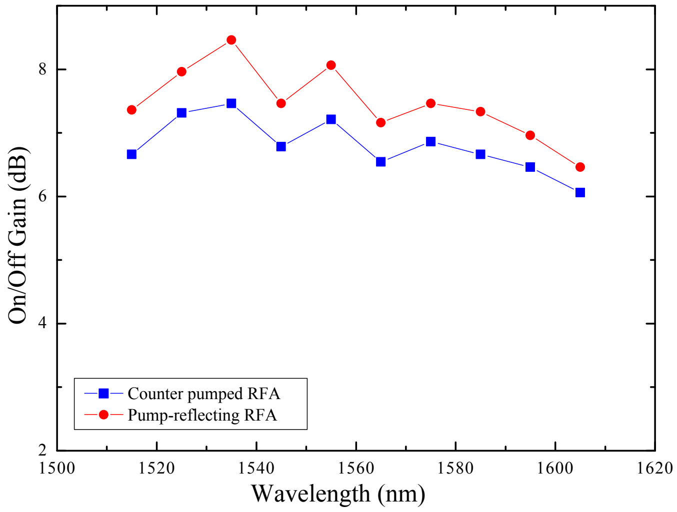

Figure 4.3: Experimental measurements of the On/Off gain of the amplifier with and without the pump reflection.

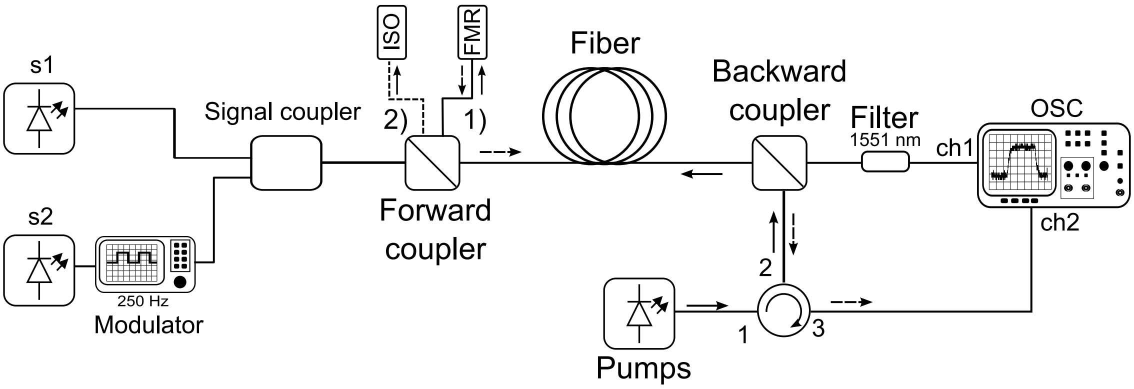

Figure 4.4: Experimental setup for measuring the transient effect of the amplifier with and without the pump reflection.

shows the total reflected pump power deviations of the pump–reflecting RFA. Results show that the drop of the S_2 channel will increase the reflected pump power. This observation reflects the fact that the pump suffers from less depletion when the channels are dropped from the system. Because of this increase in the reflected pump power, the transient response of the surviving channel will be higher when compared to the counter–pumped RFA. These experimental results show that the pump–reflecting RFA has a worse response due to channel add/drop, when compared to the conventional pumping schemes. This could lead to stronger signal degradation if this configuration is applied to dynamic optical networks.

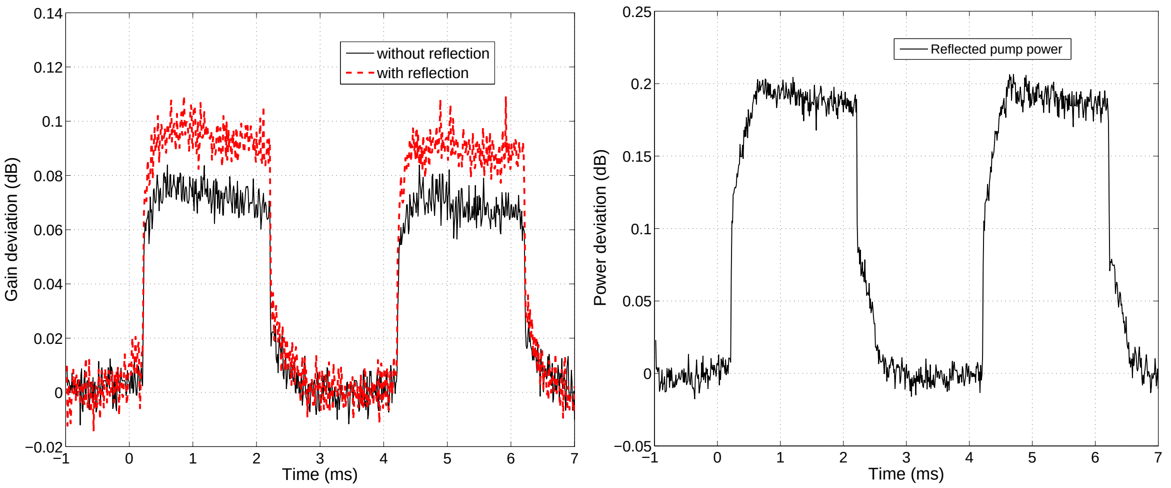

(a) (b)

Figure 4.5: a) Surviving channel gain deviations as function of time when the signal S_2 is add/drop, considering a counter–pumped RFA or a pump–reflecting RFA; b) Reflected pump power deviations as function of time, due to channel add/drop, at the output of the circulator.

4.3 Numerical Evaluation of Pump–Reflecting RFAs

In order to analyze the pump–reflecting RFA behavior, we perform numerical simulations using different parameters for the amplifier, such as RFA configuration, pumping power, and different length. Since we are performing simulations, instead of using a FMR, we use a FBG, with an ideal reflectivity coefficient, $R = 1$, and centered at the wavelength of the pump. We investigate the counter–pumped RFA with a FBG, Fig. 4.6(a), and the co–pumped RFA with a FBG, Fig. 4.6(b). In order to have a reference behavior for the RFA, we also investigate the conventional counter–pumped RFA, co–pumped RFA and the bidirectional RFA. In the bidirectional configuration, the pumps on both sides are independent from each other.

In these simulations, unless otherwise stated, we consider the use of a SSMF with 40 km of length with an effective area of 80 μm^2 and a pump centered at 1450 nm, with an attenuation of 0.22 dB/km. We use three channels, S_1, S_2, and S_3, with wavelengths centered at 1550 nm, 1551 nm, and 1552 nm, respectively, with an attenuation of 0.20 dBm/km, and with 0 dBm of input signal power per channel. To reproduce the add/drop of channels, both signals S_2 and S_3 are turned ON and OFF with a frequency of 250 Hz.

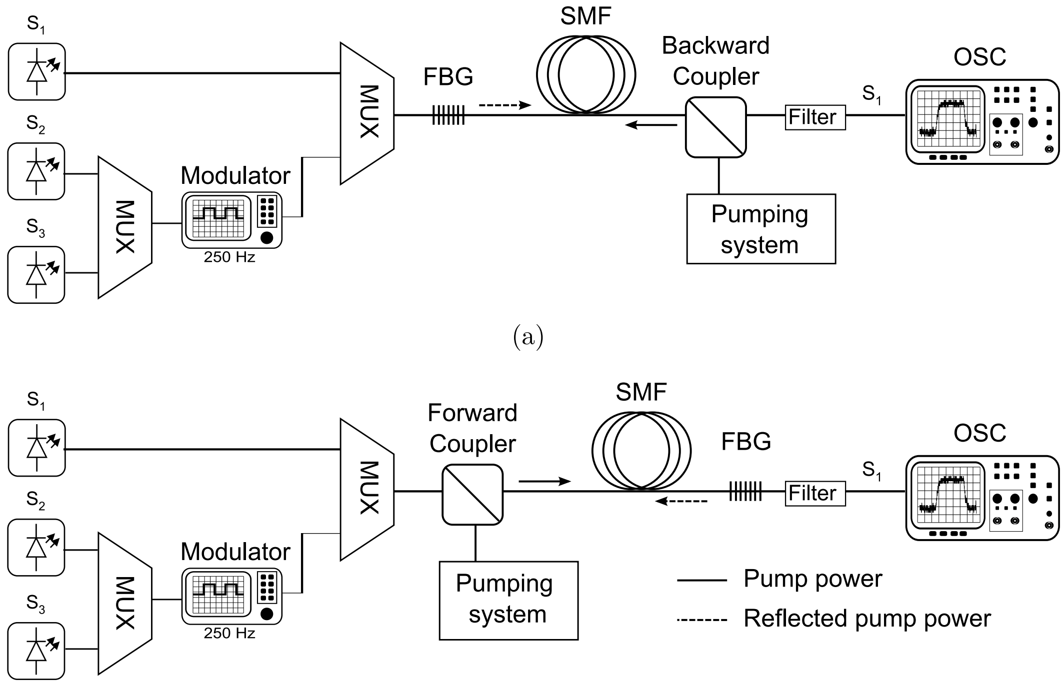

Figure 4.6: a) Counter–pumped and b) co–pumped schematic diagram of a RFA with a FBG to reflect the unused pump power.

4.3.1 Modeling the Pump–Reflecting RFA

In order to simulate the behavior of the RFA, we will use the average power analysis (APA) numerical model, presented in Section 2.3.3. However, in order to describe the pump–reflecting RFA, we need to take special attention to the boundary conditions. To reflect the pump power, we insert a FBG centered at the pump wavelength in the opposite side of the pump. Because of this, the pump power that reaches the end of the amplifier in the opposite side of the pumps is reflected back into the amplifier. In the case of a counter–pumped RFA with reflection, the reflected pump wavelength has the following boundary conditions,

$$P^{-}_{pump,i}(L,t) = P_{pump,i}(t), \tag{4.1}$$

$$P^{+}_{refle,i}(0,t) = RP^{-}_{pump,i}(0,t), \tag{4.2}$$

where, $P_{pump,i}$ is the power of pump i, $P^{-}_{pump,i}(L,t)$ is the injected pump power in the end of the transmission fiber, $P^{-}_{pump,i}(0,t)$ is the optical power of pump i in the backward direction at the beginning of the amplifier, R is the reflectivity coefficient of the FBG and $P^{+}_{refle,i}(0,t)$ is the reflected pump power at the beginning of the amplifier.

In the case of a co–pumped RFA with reflection, the reflected pump wavelength has the following boundary conditions

$$P^{+}_{pump,i}(0,t) = P_{pump,i}(t), \tag{4.3}$$

$$P^{-}_{refle,i}(L,t) = RP^{+}_{pump,i}(L,t), \tag{4.4}$$

where $P^{+}_{pump,i}(0,t)$ is the injected pump power at the beginning of the transmission fiber in the forward direction, $P^{+}_{pump,i}(L,t)$ is the optical pump power of pump i in the forward direction at the end of the amplifier, and $P^{-}_{refle,i}(L,t)$ is the reflected pump power of pump i at the end of the amplifier in the backward direction.

4.3.2 Steady–State Regime

For the evaluation of the steady–state regime of the pump–reflecting RFA, we compare three configurations: the conventional counter–pumped amplifier with 700 mW of pump power; the pump–reflecting counter–pumped RFA with the same pump power as the conventional configuration; and the pump–reflecting counter–pumped RFA with the pump power reduced to 625 mW in order to maintain the same gain as the conventional amplifier.

Figure 4.7 shows the On/Off gain as function of the input signal power, for a signal centered at 1550 nm in the steady–state regime and with the considered configurations. Results show that the pump–reflecting counter–pumped RFA with the same pump power as the conventional counter–pumped amplifier enhances the On/Off gain up to 2 dB, when the amplifier is not saturated. In order to provide the same gain as the conventional counter–pumped amplifier for a total input power of 4.8 dBm, the input pump power in the amplifier with FBG can be reduced by 75 mW. Thus, if the goal is to provide the same On/Off gain as in the conventional counter–pumped amplifiers, the configuration with the FBG allows a reduction of pump power. This fact can also lead to an improvement in the amplifier noise figure [4]. In Fig. 4.7, we can also observe a difference between the On/Off curves for the conventional counter–pumped RFA and the pump–reflecting counter–pumped RFA with the pump power adjusted. This difference occurs because the configuration with the FBG behaves as a bidirectional amplifier and, therefore, the relationship between the amplifier gain and the input signal power is slightly different compared to the conventional counter–pumped RFA. These results allow us to conclude that the inclusion of a FBG in the system increases the efficiency of the Raman amplifiers in the steady–state regime. Further investigations show a similar behavior for the co–pumping schemes.

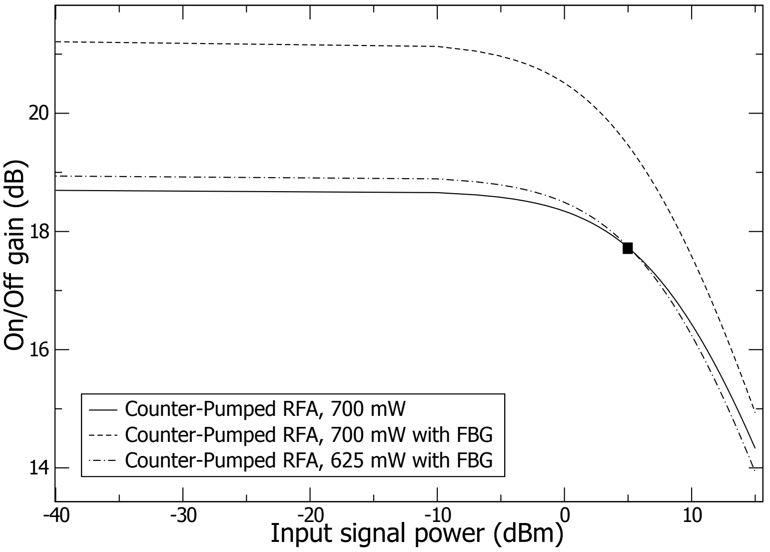

Figure 4.7: On/Off gain for a counter–pumped RFA amplifier (Fig. 4.6(a)), with and without the FBG, as function of the input signal power for the channel centered at 1550 nm; $L_{SMF} = 40\,\text{km}; \lambda_p = 1450\,\text{nm}$; $\lambda_s = 1550\,\text{nm}$.

We also analyze the relationship between the improvement in gain (the difference between the On/Off gain of amplifier with and without the FBG), as a function of the fiber length. We consider a pump power of 600 mW and a signal centered at 1550 nm with 0 dBm of optical power. Since we are interested in assessing the improvement of the On/Off gain, the pump power is the same in both configurations. Fig. 4.8 depicts the difference between the On/Off gain of the amplifier with or without the FBG, as function of the transmission length. Analysis of the figure shows that the improvement in the gain of the amplifier will depend on the fiber length. This happens because, as the fiber length increases, the unused pump power decreases, reducing the pump power reflected back by the FBG.

4.3.3 Dynamic Regime

The transient response of a RFA is mainly influenced by the pumping scheme, the pump power, and the length of the fiber [12]. To compare the behavior of the dynamic regime between different pumping schemes, we need to ensure that the amplifier gain is approximately the same in all configurations. Therefore, we reduce the pump power of the pump–reflecting Raman amplifiers in order to establish a similar On/Off gain, when all channels are turned ON. For the counter–pumped RFA with a FBG, the pump power should be reduced from 700 mW to 625 mW, and for the co–pumped RFA with a FBG, from 700 mW to 635 mW.

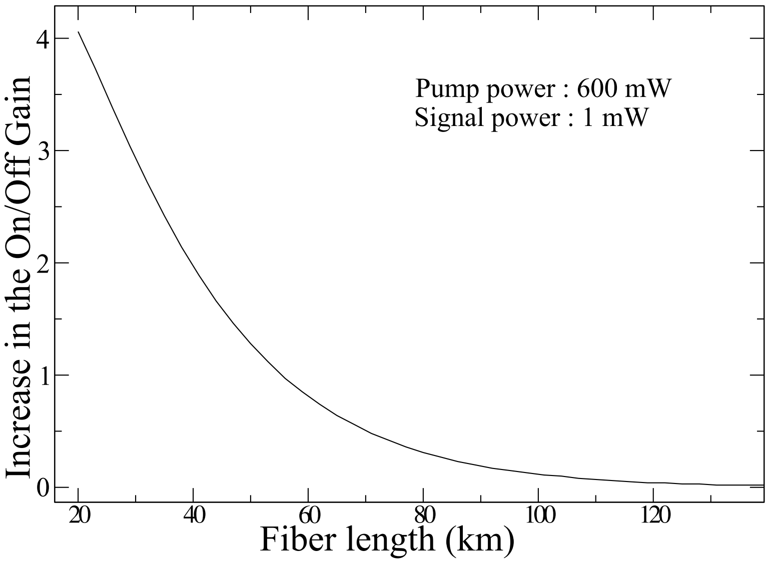

Figure 4.8: Improvement in the On/Off gain between the amplifier with and without a FBG, as function of the fiber length. $\lambda_p = 1450\,\text{nm}$; $P_{p,in} = 600\,\text{mW}$; $\lambda_s = 1550\,\text{nm}$.

To analyze the impact of including a FBG in a counter–pumped amplifier, Fig. 4.6(a), and in a co–pumped amplifier Fig. 4.6(b), we compare the following pumping schemes:

I – counter–pumped RFA with a pump power of 700 mW;

II – bidirectional pumped RFA with two independent pumps with the same pump wavelength, but different powers: forward and backward pump powers of 75 mW and 625 mW;

III – counter–pumped RFA with a FBG, with a pump power of 625 mW.

IV – co–pumped RFA with a pump power of 700 mW;

V – bidirectional pumped RFA with two independent pumps with the same pump wavelength, but different powers: forward and backward pump powers of 635 mW and 63.5 mW;

VI – co–pumped RFA with a FBG, with a pump power of 635 mW.

All schemes present approximately the same On/Off gain for the surviving channel when all signals are present in the fiber. Note that the FBG is only considered in cases III and VI. In case II the forward pump has the same input power as the reflected pump power in case III. Regarding case V, the backward pump has the same pump power as the reflected pump power in case VI.

Figure 4.9 shows the gain deviation of the surviving channel centered at 1550 nm, as function of time, when channels S_2 and S_3 are added/dropped for the configurations I, II, and III. The drop of these two signals occurs at 0 ms and the addition at 2 ms. The surviving channel in case I has a gain deviation of 0.6 dB with a rise time of 247 μs (between 10 % and 90 % of the maximum value of the deviation). In case II the behavior of the transient is similar to case I. When the FBG is included in the amplification system, case III, the results show that the gain deviation is higher, around 0.7 dB, with a rise time of 316 μs. Despite the longer rise time, which can be an advantage to mitigate the transient effects, the gain deviations are higher, showing that this configuration has a worse response to the channels add/drop, when compared with the others pumping schemes. With this analysis, we can conclude that the increase in the transient response occurs due to the fluctuations in the reflected pump power that are re–injected into the fiber.

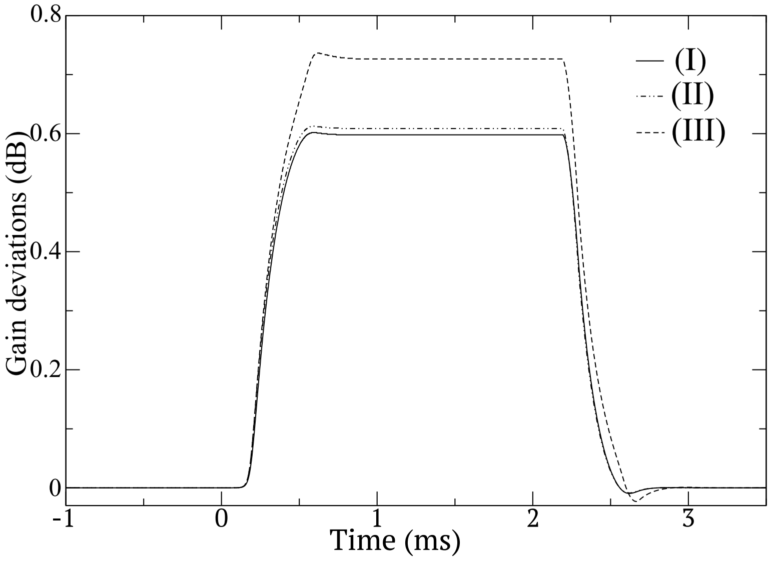

Figure 4.9: Gain deviation of the surviving channel as function of time, when 2 out of 3 channels are added/dropped. L_{SMF} = 40 km; λ_p = 1450 nm; λ_s = 1550, 1551, 1552 nm; $P_{s,in}$ = 0 dBm/channel.

Figure 4.10 shows the gain deviation of the surviving channel centered at 1550 nm for the considered co–pumped schemes, IV, V, and VI as function of time, when signals S_2 and S_3 are add/drop. As it is shown, the transient response in case IV has a rise time of 6.4 μs, and a gain deviation of approximately 0.9 dB. In case V the surviving gain deviations are smaller, 0.8 dB, with a rise time of 9.3 μs. When the FBG is used, in case VI, the results show that the gain deviation is up to 1.1 dB, with a rise time of 199 μs. This corresponds to an increase of the gain deviation in more than 25%, when compared with a conventional co–pumped RFA.

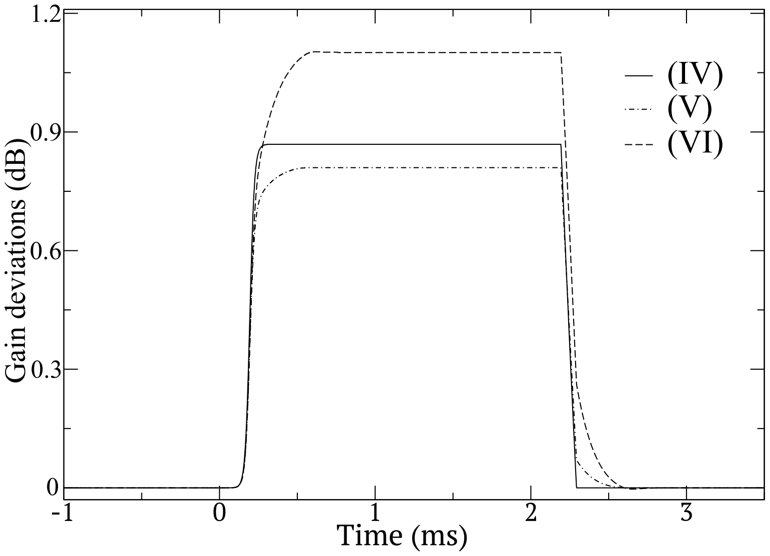

Figure 4.10: Surviving channel, S_1, gain deviation as function of time, when 2 out of 3 channels are added/dropped, in co–pumped schemes. $L_{SMF} = 40\,\text{km}$; $\lambda_p = 1450\,\text{nm}$; $\lambda_s = 1550,\ 1551,\ 1552\,\text{nm}$; $P_{s,in} = 0\,\text{dBm/channel}$.

We can also observe that the co–pumped RFA with a FBG, case VI, has a higher gain deviation than when compared to the counter–pumped RFA with a FBG, case III. In Fig. 4.11 we present the gain deviation of the reflected pump power, in the opposite side of the pump, as function of time for the counter–pumped RFA and co–pumped RFA, when the last 2 out of 3 channels are added/dropped. Results show that the reflected pump power fluctuation in the co–pumped RFA with a FBG, case VI, is higher. This is due to the faster saturation of the co–pumped configuration relative to the counter–pumped configuration [12]. Consequently, a variation in the input signal power has a higher impact in the depletion of the pump power.

Figure 4.12 shows the reflected pump power of case III and case VI, as function of total input power for only one channel centered at 1550 nm. Results show that the increase in the input signal power depletes the pump power faster in the co–pumped RFA with a FBG, case VI, when compared to case III. When the input power changes from 4.8 dBm to 0 dBm (drop of 2 channels), the reflected pump power increases to 11.8 mW for the co–pumped amplifier RFA with a FBG, case VI, and to 4.8 mW in the case of the counter–pumped RFA with a FBG, case III. This increase in the reflected pump power leads to a higher transient response of the co–pumped RFA with FBG, case VI. Moreover, the transient effect in co–pumped configurations is quicker than the counter–pumped configurations, which makes the mitigation of the transient effect hard to achieve. Therefore, in the following analysis, we will focus exclusively in the counter–pumped RFA with a FBG, Fig. 4.6(a).

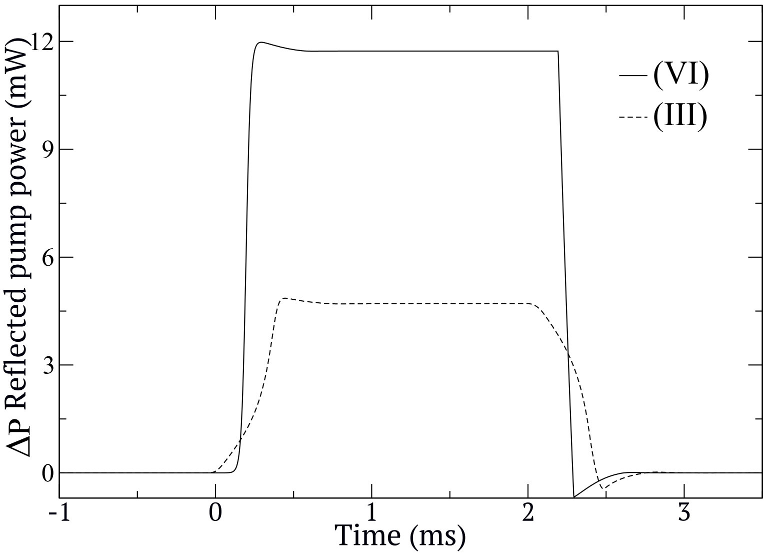

Figure 4.11: Gain deviation of the reflected pump power at the opposite side of the pump as function of time for the counter–pumped RFA and co–pumped RFA, Fig. 4.6(a) and Fig. 4.6(b) respectively, when the last 2 out of 3 channels are added/dropped. $L_{SMF} = 40\,\text{km}$; $\lambda_p = 1450\,\text{nm}$; $\lambda_s = 1550,\ 1551,\ 1552\,\text{nm}$; $P_{s,in} = 0\,\text{dBm/channel}$.

Different Pumping Power

In order to investigate the impact of reflecting the pump power in the transient response, we simulate three scenarios using different backward pump powers for the conventional counter–pumped RFA: (a) 300 mW, (b) 600 mW, and (c) 800 mW. And, for each of these scenarios we simulate the behavior of the counter–pumped RFA with a FBG, Fig 4.6(a). The pump power in the pump–reflecting RFA is reduced in order to assure that, for each scenario, the two pumping configurations have approximately the same On/Off gain.

Figure 4.13 shows the surviving channel gain deviation as function of time, when the channels S_2 and S_3 are added/dropped, for scenarios (a) 300 mW, (b) 600 mW, and (c) 800 mW. Results show the contribution of the reflected pump power to the increase of the gain deviation related to the counter–pumped RFA is about 36 %, 24 %, and 19 % for scenarios (a), (b), and (c), respectively. Therefore, the fluctuations of the reflected power have a small impact on the surviving channels power transients as the pump power increases. This happens because, as the pump power increases, the depletion of the pump has a smaller impact. The rise time of the conventional counter–pumped RFA is about 234 μs, 245 μs, and 244 μs, for scenarios (a), (b), and (c), respectively. For the counter–pumped RFA with a FBG, the rise time is around 283 μs, 311 μs, and 319 μs for scenarios (a), (b), and (c), respectively. When comparing

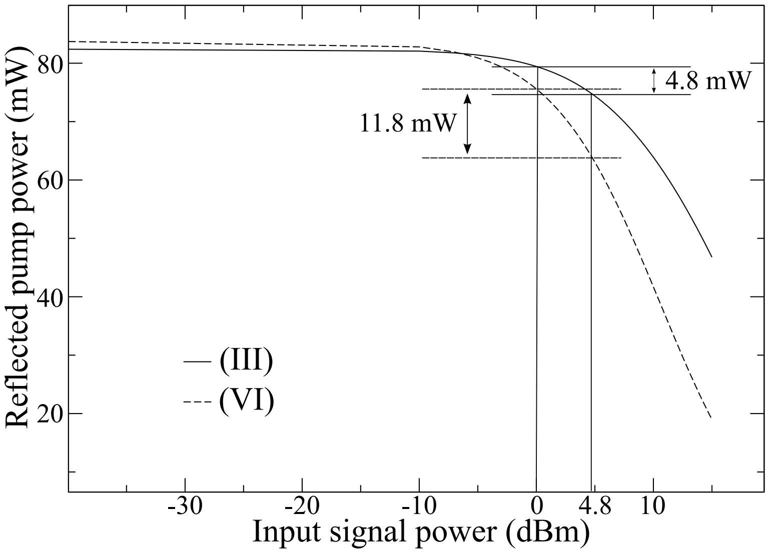

Figure 4.12: Reflected pump power for a RFA counter–pumped with 625 mW of pump power and with a FBG and a RFA co–pumped with 635 mW of pump power with a FBG, Fig. 4.6(a) and Fig. 4.6(b), respectively, as function of the signal input power. $L_{SMF} = 40\,\text{km}$; $\lambda_p = 1450\,\text{nm}$; $\lambda_s = 1550\,\text{nm}$.

these configurations we can conclude that the rise time is higher in the configurations that include FBG. This happens because both the pump and the signal take longer to achieve a new steady–state power distribution, due to the reflection of the pump power fluctuations back into the amplifier. When analyzing the dependence of the rise time on the input pump power, we conclude that an increase in the pump power will not have a significant impact in the rise time of the transient response.

Different Length

We investigate the transient response as a function of the fiber length. We simulate different scenarios with 40 km, 60 km, and 80 km of fiber length. The pump has an optical power of 600 mW for the amplifier without a FBG, and it is reduced for the amplifier with a FBG, in order to maintain the same On/Off gain as the conventional counter–pumped RFA for each fiber length. Fig. 4.14 shows the surviving channel gain deviation as function of time. Considering the intensity of the transient effects, results show that, for distances of 40 km, 60 km, and 80 km, the increase in the transient effect in the amplifier with a FBG is around 24 %, 13 %, and 6 %, respectively, when compared to the counter–pumped RFA. These results also show that, as the length of the fiber increases, the impact of the FBG on the RFA is smaller. The rise time for the conventional counter–pumped RFA is about 245 μs, 322 μs, and 368 μs, for a fiber length of 40 km, 60 km, and 80 km, respectively. In the case of the counter–pumped

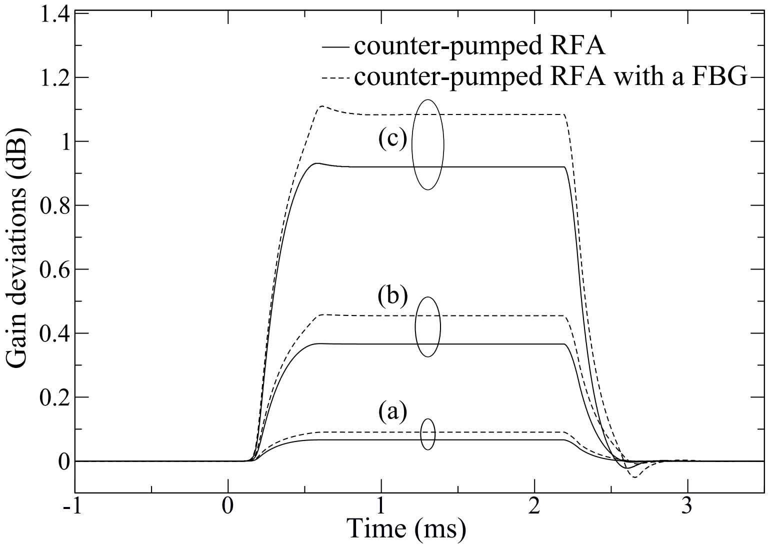

Figure 4.13: Surviving channel gain deviation as function of time, when 2 out of 3 channels are add/drop, when scenarios a) pumped with 300 mW, (b) pumped with 600 mW, and (c) pumped with 800 mW considering. The two pumping schemes in each scenario have approximately the same On/Off gain.

RFA with a FBG, the rise time is about 310 μs, 377 μs, and 398 μs, for the fiber length of 40 km, 60 km, and 80 km, respectively. As the fiber length increases, the rise time also increases in both configurations. This happens because the propagation time in the fiber for the signals and pumps increases and thus the time that the amplifier takes to reach a new steady–state power distribution also increases.

4.4 Mitigation and Control of the Power Transients

In order to develop an efficient RFA suitable for dynamic optical networks, it is necessary to find a solution that mitigates the transient effect due to the channels add/drop. We propose a solution based on a pump–controlled gain–clamping technique. With this technique, we are able to operate close to the maximum possible gain, when all signals are present [20].

In a pump–reflecting RFA, when an add/drop occurs, the reflected pump power and the surviving channel output power will have different transient responses. However, the transient response of the reflected pump power will be proportional to the transient effects on the surviving channels. Therefore, by monitoring the reflected pump power after the propagation through the fiber, we can extract information regarding the evolution of the powers inside the amplifier without using probe channels or signals. By monitoring the reflected pump power after the propagation on the fiber,

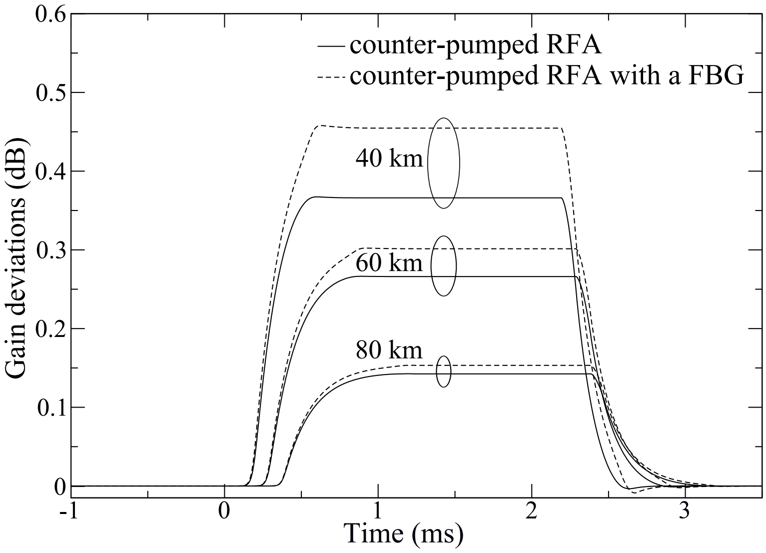

Figure 4.14: Surviving channel gain deviation for a distance of 40 km, 60 km and 80 km, as function of time, when 2 out of 3 channels are add/drop. The two pumping schemes for each distance have approximately the same On/Off gain.

---

we are monitoring the impact of several effects, such as pump depletion, pump power reflections, Rayleigh backscattering and noise generation. However, it is important to understand that the main objective is not to mitigate the power fluctuations in the reflected pump power, but rather to use the information retrieved from the reflected pump power to control the input pump power and mitigate the surviving channel power fluctuations.

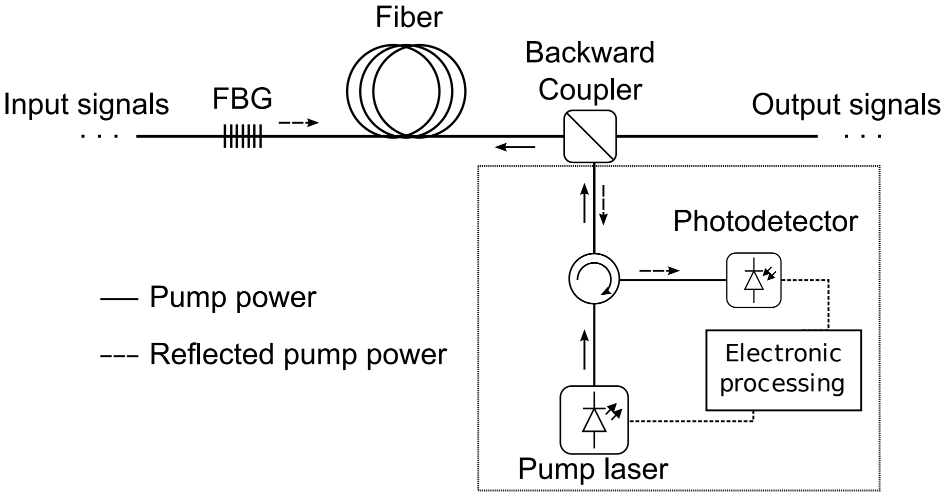

Figure 4.15: Schematic diagram of pump–reflecting RFA with transient control.

In Fig. 4.15, a schematic diagram of the proposed control system that mitigates the transient response in a pump–reflecting RFA is presented. It consists of an optical circulator, a monitoring system and an electronic processing module at the end of the amplifier. The pump power is injected through both the circulator and the WDM backward coupler positioned at the end of the transmission fiber, in the opposite direction of the signals. At the beginning of the amplifier, the unused pump power is reflected in the forward direction by the FBG. Due to the bidirectionality of the WDM backward coupler, the reflected pump power is removed from the transmission fiber at the end of the amplifier. Finally, the reflected pump power is redirected to the photodetector on the optical circulator. Based on the information acquired, it is possible to control the input pump power with a feedback control loop.

4.4.1 Numerical Assessment

In order to validate this technique in terms of applicability, we analyze the amplifier behavior numerically. The pump control is performed using a negative–feedback control loop, based on a proportional–derivative (PD) control. The time evolution of the backward input pump power, $P_{in}^{-}(t)$, is given by [20]

$$\begin{aligned} P_{in}^{-}(t+dt) = P_{in}^{-}(t) + K_p[P_{refle}^{+}(t) - P_{refle}^{+}(0)] \\ + K_d\frac{d}{dt}[P_{refle}^{+}(t) - P_{refle}^{+}(0)], \end{aligned} \tag{4.5}$$

where $P_{refle}^{+}(t)$ is the reflected pump power at the end of the amplifier, $P_{refle}^{+}(0)$ represents the stationary value of the reflected pump when all channels are present. The coefficients K_p and K_d represent the gains of the proportional and differential errors used in the negative–feedback system [20], respectively. These coefficients must be carefully chosen in order to achieve a fast elimination of surviving channel fluctuations and avoid unwanted oscillations of the surviving channel. To determine these coefficients, we follow the Ziegler–Nichols method [23]. According to this method, we start by setting K_d to zero, and then increase K_p, in a step–by–step basis, until a periodic oscillation of the surviving channel is reached. At this point, the proportional gain constant obtained is denoted as K_c and the oscillation period as P_c. Based on these coefficients the starting values for K_p and K_d are given by $K_p = 0.6K_c$ and $K_d = 0.075K_cP_c$ [23]. The optimum values of K_p and K_d are found by adjusting each coefficient until an acceptable power fluctuation of the surviving channels is obtained.

Let us consider three input channels, S_1, S_2, and S_3, with an input signal power of 0 dBm/channel, a backward pump with a wavelength centered at 1450 nm with 625 mW of input pump power, and a FBG centered at the pump wavelength at the beginning of the amplifier fiber, identical to case III from Section 4.3.3. The fiber used is a SSMF with 40 km of fiber length. The dropping of channels S_2 and S_3 occurs at 0 ms and the adding of these channels at 4 ms. By applying the Ziegler–Nichols method, $K_c = 0.8$ and $P_c = 1.5\text{x}10^{-3}$ s are obtained as starting point for the optimization process. After the optimization process, in which we evaluate the behavior of the surviving channel after the add/drop, we obtain $K_p = 0$, and $K_d = 7.848\text{x}10^{-5}$. Fig. 4.16 shows the gain deviation of the surviving channel as function of time, with and without the control system. With the control system, the power fluctuations of the RFA are kept below 0.2 dB, when two channels are dropped. Consequently, a new steady state is reached and the input pump power is reduced by the control loop to approximately 600 mW. When only one channel is dropped, the gain deviations of the surviving channels are smaller, below 0.1 dB. At 4 ms, when the channels are added to the system, we can observe that the control system will increase the pump power and the initial steady–state is reached.

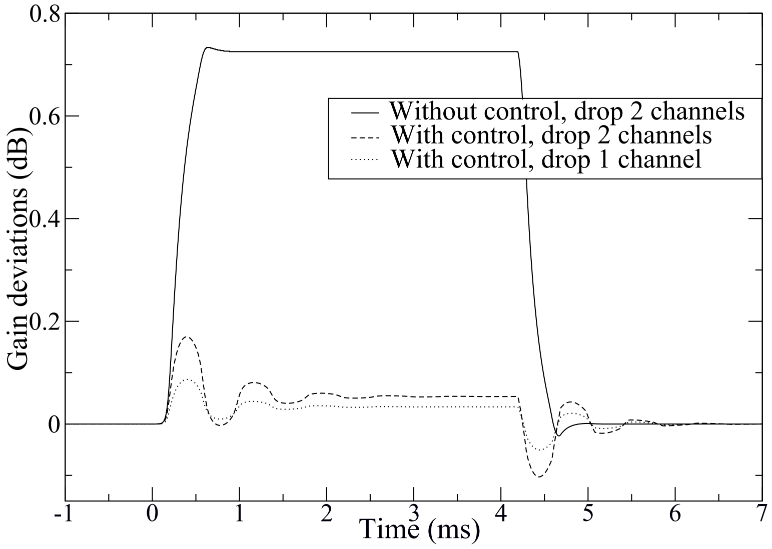

Figure 4.16: Surviving channel gain deviation as function of time of a counter–pumped RFA with a FBG, with and without the pump–control gain–clamping technique.

By monitoring the reflected pump power and applying the PD control, we are able to successfully mitigate the transient effect in the surviving channel. Similar results are obtained for other scenarios considering a different number of channels dropped and fiber length.

4.4.2 Experimental Validation

Figure 4.17 presents the experimental setup implemented to evaluate the feasibility of the proposed method to control the transient effect, based on monitoring the reflected pump power. Two signals are used, centered at 1551 nm and 1601 nm, with

1.76 dBm and 6.02 dBm of input optical power, respectively. The signal centered at 1601 nm is a square–wave modulated to reproduce the add/drop of this channel. As a pump we use a butterfly laser controlled by a Newport 5005 laser diode controller module (Newport Corp., Irvine, California, USA). This laser is centered at 1490 nm and has an input optical power of 85 mW at the steady–state regime. An optical filter centered at 1551 nm is used to filter the modulated channel at the end of the fiber. We use a DCF with 5 km of fiber length, and attenuation coefficients of 0.93 dB/km, 0.92 dB/km, and 1.8 dB/km for the wavelengths centered at 1551 nm, 1601 nm, and 1490 nm, respectively. The reflection is done using a WDM coupler and a fiber mirror reflector, with a reflectivity of 99% from 1420 nm to 1490 nm, at the beginning of the fiber. The reflected pump power, at the output 3 of the circulator, is monitored by a HP8153A series power meter (Agilent, Santa Clara, California, USA) with a sampling time of 20 ms. The power meter and the butterfly laser controller communicate with the computer by means of a general purpose interface bus (GPIB). On the computer, a program is developed using LabView, in order to retrieve the information from the power meter and calculate the output power with a PD emulator. The PD controls the current of the laser according to the power fluctuation of the reflected pump at the end of the transmission fiber. A digital OSC detects the surviving channel power fluctuations at the end of the amplifier.

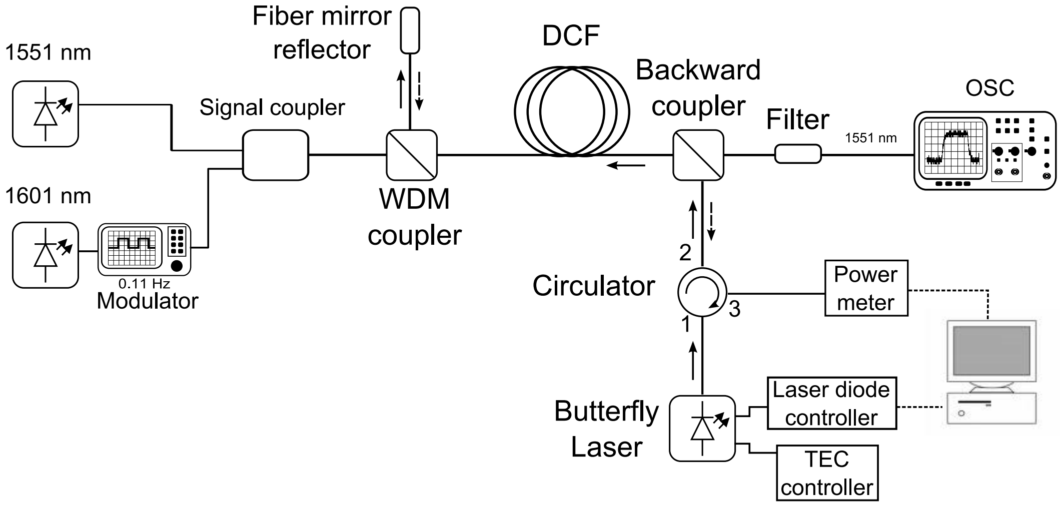

Figure 4.17: Experimental setup used to measure and control the transient effect of a pump–reflecting counter–pumped RFA.

In the implemented setup, the pump control is performed using a feedback loop, implemented in the control unity (which is a computer). The time evolution of the backward input pump power, $P_{in}^{-}(n+1)$, is now discretized with a sampling time of

20 ms and therefore eq. (4.5) becomes

$$\begin{aligned} P_{in}^{-}(n+1) = P_{in}^{-}(n) + K_p[P_{refle}^{+}(n) - P_{refle}^{+}(0)] \\ + K_d \frac{[P_{refle}^{+}(n) - P_{refle}^{+}(n-1)]}{\Delta t}, \end{aligned} \tag{4.6}$$

where $P_{refle}^{+}(n)$ is the reflected pump power at the end of the amplifier, $P_{refle}^{+}(0)$ represents the stationary value of the reflected pump when all channels are present and Δt the sampling interval.

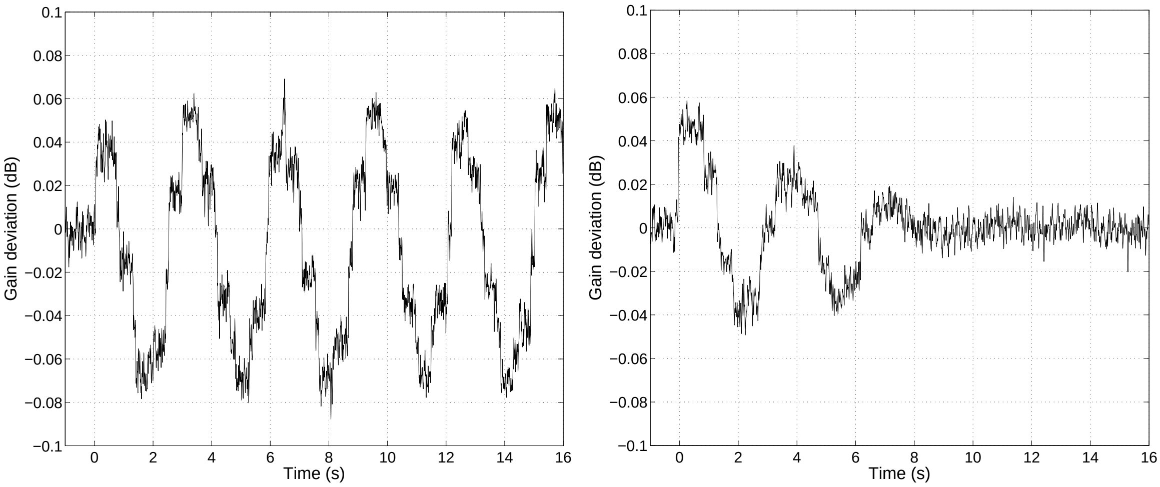

(a) (b)

Figure 4.18: a) Surviving channel gain deviation at the oscilloscope in a channel drop scenario, when the feedback control loop coefficient K_c is equal to 1.5 and K_d is equal to 0; b) Surviving channel gain deviation at the oscilloscope in a channel drop scenario, when the feedback control loop coefficient K_c is equal to 0.97 and K_d is equal to 0.34.

The reflected pump power is obtained from experimental measurements where there are additional transmission effects (e.g. power reflections due to the fiber splices and connectors) that were not taken into account in the numerical simulations. For this reason, the adjustment of K_p and K_d in order to be able to mitigate the surviving channel transient response is more difficult. Let us consider a drop scenario, where the channel centered at 1601 nm is removed. Following the Ziegler–Nichols technique, we start by maintaining $K_d = 0$ and increase the K_p until a steady oscillation of the surviving channel is achieved. Fig. 4.18(a) shows the surviving channel power fluctuation as function of time when the proportional gain, K_c, is 1.5. As we can see, the surviving channel is oscillating with a period around 3 s which is the P_c.

Based on the results obtained, we manually adjust the K_p and the K_d with different combinations, in order to allow a smooth mitigation of the power fluctuation of the surviving channel. Fig. 4.18(b) shows the surviving channel gain deviation when the drop of the channel centered at 1601 nm occurs at t=0 s, when considering K_p= 0.97 and $K_d = 0.34$. As we can see, the surviving channel returns to the initial steady–state power 8 s after the removal event. The settling time is high because of all the delay associated with the control system.

Now, let us consider an drop/add scenario, where the channel centered at 1601 nm is removed and then added to the fiber. Due to the fact that the control system is limited by the sampling time of the power meter and the response time of the laser diode controller, a low add/drop frequency is used to modulate the 1601 nm channel, in this case, 0.11 Hz. Fig. 4.19 shows a comparison between the surviving channel gain deviation as function of time with and without control. In this case, after the adjustment the K_p is 0.5 and the K_d is 0. As we can see in the figure, with control the surviving channel returns to the initial steady state before the next add/drop event. The oscillation of the surviving channel obtained is caused by the slow response time and the delays of the control system. Nevertheless, and despite of the system delay, the transient effect is mitigated before it reaches its higher value.

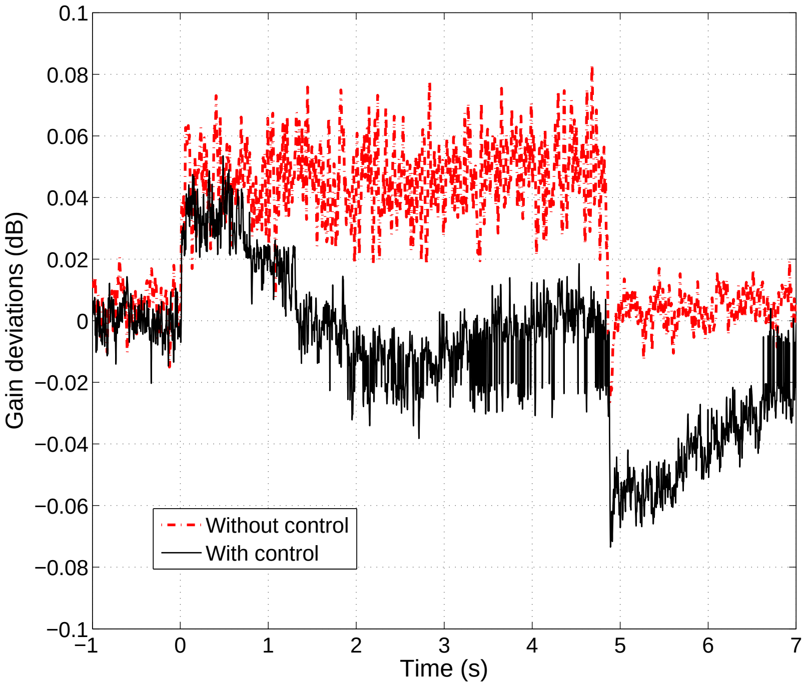

Figure 4.19: Experimental results of the surviving channel gain deviation as function of time of a counter–pumped RFA, with and without the pump–control gain clamping technique channel add/drop.

The experimental results obtained show that it is possible to control the surviving channel power fluctuations based on the information retrieved from the reflected pump power. Furthermore, based on the experiments made we estimate that it is possible to control the transient in a shorter time interval with the development of a fast control system.

4.5 Conclusions

Future communication networks should have the ability to support an enormous amount of bandwidth in an energy efficient way. One step further in that direction is the increase of the efficiency of optical amplifiers, such as RFA. However, these efficient amplifiers need to be compatible with dynamic networks.

Using a FMR or a FBG to reflect the unused pump power back into the amplifier fiber has advantages in the steady–state regime, namely a higher efficiency. However, when considering the dynamic regime, the amplifier has a worse response to channel add/drop. Experimental results showed that the dynamic response of a pump–reflected RFA increased in more than 20 %, when compared with the conventional pumping scheme.

We investigated the pump–reflecting RFA based on a numerical implementation of the propagation equation for the RFA that includes the time and space variation. The transient response dependence on the amplifier configuration, on input pump power, and on the distance was analyzed. Results showed that the pump–reflecting co–pumping scheme has a worse dynamic response than the pump–reflecting counter–pumped RFA. Also, that the impact of reflecting the pump power on the transient effect diminished with the increase of the input pump power and with the increase of the fiber length.

We presented a new technique to implement a pump–controlled gain clamping technique, that allows to obtain an efficient low cost RFA with transient control. The mitigation technique is based on the control of the input pump power, using a negative–feedback control loop based on the monitoring of the behavior of the reflected pump power at the same side of the pump. With this control scheme, there is no need for extra lasers and WDM couplers. We showed numerically that in the considered setup, the power fluctuations of the surviving channel were about 0.7 dB, when transient response was not controlled. On the other hand, when transient control was applied, these fluctuations were maintained bellow 0.2 dB. Finally, we experimentally implemented this technique to a pump–reflecting counter–pumped RFA, and we were able to mitigate and control the power fluctuations of the surviving channel, demonstrating that this proposal can be successfully implemented. Despite, the low response time of this solution and also the short length of the DCF, we were able to reduce the transient effect before reaching its highest value. With this control system it is possible to use a FBG that will increase the efficiency of the RFA without compromising the dynamic regime, allowing the development of an efficient low cost RFA suitable for dynamic optical networks.

References

[1] J. Ferreira, M. Fugihara, and A. Pinto, "Energy efficient Raman fiber amplifiers suitable for dynamic optical networks," in *Proc. European Conference on Networks and Optical Communications (NOC)*, Jun. 2010.

[2] J. Ferreira, M. Fugihara, and A. Pinto, "Transient response and control of pump-reflecting Raman fiber amplifiers," *Fiber and Integrated Optics*, vol. 29, no. 1, pp. 44–61, Dec. 2009.

[3] J. Ferreira, A. Pinto, and P. Mão Cheia, "Método e mecanismo para controlo e mitigação do efeito transitório em amplificadores ópticos de Raman com reflexão das bombas," Patent: 104930, Dec. 2009.

[4] J. Nicholson, "Dispersion compensating Raman amplifiers with pump reflectors for increased efficiency," *IEEE/OSA Journal of Lightwave Technology*, vol. 21, no. 8, pp. 1758–1762, Aug. 2003.

[5] M. Tang, Y. Gong, and P. Shum, "Design of double-pass dispersion-compensated Raman amplifiers for improved efficiency: guidelines and optimizations," *IEEE/OSA Journal of Lightwave Technology*, vol. 22, no. 8, pp. 1899–1908, Aug. 2004.

[6] M. Ali, A. Ahmad, A. Zamzuri, R. Mohamad, and M. Mahdi, "Impact of the pump reflector in double-pass discrete Raman amplifiers," *Microwave and optical technology letters*, vol. 48, no. 4, pp. 777–779, Apr. 2006.

[7] J. Lee, Y. Chang, and Y. Han, "A detailed experimental study on single-pump Raman/EDFA hybrid amplifiers: static, dynamic, and system performance comparison," *IEEE/OSA Journal of Lightwave Technology*, vol. 23, no. 11, pp. 3484–3493, Nov. 2005.

[8] H. Lin and P. Lai, "The research of mix Raman and EDFA amplifier recycling residual Raman pump for amplifier gain efficiency improvement," *Microwave and Optical Technology Letters*, vol. 51, no. 2, pp. 358–361, Feb. 2009.

[9] J. Nicholson, “Discrete Raman amplifiers with pump reflectors for increased gain and efficiency,” in *Proc. European Conference on Optical Communication (ECOC)*, Sep. 2002, pp. 1–2.

[10] S. Gray, “Transient gain dynamics in wide bandwidth discrete Raman amplifiers,” in *Proc. Optical Fiber Communication Conference (OFC)*, Mar. 2002, pp. 512–513.

[11] Z. Zhang, J. Fu, D. Guo, and L. Zhang, “Lightpath routing for intelligent optical networks,” *IEEE Network*, vol. 15, no. 4, pp. 28–35, Jul. 2001.

[12] M. Karásek and M. Menif, “Channel addition/removal response in Raman fiber amplifiers: modeling and experimentation,” *IEEE/OSA Journal of Lightwave Technology*, vol. 20, no. 9, pp. 1680–1687, Sep. 2002.

[13] L. Wang, B. Hwang, and L. Yang, “Gain transients in copumped and counterpumped Raman amplifiers,” *IEEE Photonics Technology Letters*, vol. 15, no. 5, pp. 664–666, May 2003.

[14] C. Kim, E. Son, H. Cho, and Y. Han, “Experimental study on the effect of codirectional Raman gain on system’s performance,” *Optics Express*, vol. 15, no. 10, pp. 6146–6151, May 2007.

[15] C. Chen and W. Wong, “Transient effects in saturated Raman amplifiers,” *IET Electronics Letters*, vol. 37, no. 6, pp. 371–373, Jan. 2001.

[16] T. Zambelis, N. Gryspolakis, and L. Chen, “Design of all-optical gain-clamped discrete fiber Raman amplifiers,” in *Proc. Lasers and Electro-Optics Society (LEOS)*, Oct. 2003, p. ThFF1.

[17] J. Gest and L. Chen, “Impact of the all-optical gain-clamping technique on the transience characteristics of cascaded discrete fiber Raman amplifiers,” *Optics Communications*, vol. 273, no. 1, pp. 138–148, Jan. 2007.

[18] M. Karásek, J. Kanka, G. Khan, and J. Radil, “Design of all-optical gain-clamped lumped Raman fibre amplifier for optimal dynamic performance,” in *IEE Proceedings-Optoelectronics*, vol. 152, no. 4, Aug. 2005, pp. 223–229.

[19] C. Chen, J. Ye, W. Wong, Y. Lu, M. Ho, Y. Cao, M. Gassner, J. Pease, H. Tsai, H. Lee, W. Lu, S. Cabot, and Y. Sun, “Control of transient effects in distributed and lumped Raman amplifiers,” *IET Electronics Letters*, vol. 37, no. 21, pp. 1304–1305, Oct. 2001.

[20] M. Karásek and M. Menif, “Protection of surviving channels in pump-controlled gain-locked Raman fibre amplifier,” *Optics Communications*, vol. 210, no. 1, pp. 57–65, Sep. 2002.

[21] G. Bolognini and F. Pasquale, “Transient effects in gain-clamped discrete Raman amplifier cascades,” *IEEE Photonics Technology Letters*, vol. 16, no. 1, pp. 66–68, Jan. 2004.

[22] X. Zhou, M. Feuer, and M. Birk, “Submicrosecond transient control for a forward-pumped Raman fiber amplifier,” *IEEE Photonics Technology Letters*, vol. 17, no. 10, pp. 2059–2061, Oct. 2005.

[23] J. Ziegler and N. Nichols, “Optimum settings for automatic controllers,” *Transactions of the A.S.M.E.*, vol. 64, pp. 759–768, Nov. 1942.

Chapter 5

Dynamic Response due to SHB and SDP in EDFAs

Nowadays, as margins in network design are decreasing in order to reduce the network cost, it is important to study all effects, even those previously assumed to be small and non–relevant. Together with gain fluctuations caused by the variation of the input signal power, gain fluctuations induced by changing the input signal spectrum, due to spectral hole burning (SHB) and site dependent pumping (SDP), are also important in erbium–doped fiber amplifiers (EDFAs). When considering these effects, even if we assume that the transients caused by input power variation are perfectly compensated by the transient control system, we observe gain fluctuations that appear in our experiment as power fluctuations on the surviving channel. As these power fluctuations propagate through several cascaded amplifiers, their impact will increase.

In this chapter, we experimentally assess the dynamical response dependence due to SHB and SDP effects on pump wavelength, pump power, and temperature of EDFAs. Following, to describe the dependence on the pump wavelength measured for EDFAS pumped around 1480 nm, we derive and validate a model that includes the SDP effect in a two–level EDFA. Finally, an investigation of the dynamic response due to SHB and SDP in an ideal gain–controlled EDFA pumped around 980 nm is presented. Part of this work was performed during an internship at Technical University of Munich. The results presented in Section 5.2 were published in [1, 2], the model presented in Section 5.3 was published in [3], and the results presented in Section 5.4 in [4].

5.1 Introduction

Gain fluctuations arising from total input power variation have been characterized extensively [5, 6]. The fundamental differential equations describing the amplifier behavior for the steady–state and for the dynamic regime for two–levels EDFAs (energy levels up to $^4I_{13/2}$ populated) are derived in [7]. This model is suitable for amplifiers pumped at wavelengths around 1480 nm and for small pump powers around 980 nm. Several solutions to mitigate and control the gain fluctuations due to input power variation were proposed [8, 9]. With respect to the contributions of SHB to gain fluctuations, several studies have been published [10, 11]. Nevertheless, most of these publications focus on its impact on steady–state performance. Experimental data presented in [12] confirms that the depth of induced spectral holes increases with amplifier compression. On the other hand, there are few reports analyzing the dynamics of SHB [13–15], and all of those studies have a strong focus on the verification of mathematical models. Besides that, only few solutions to mitigate and control this effect have been proposed [16]. When considering the SDP effect, it has been demonstrated that even small pump wavelength variations around 980 nm lead to significant changes on the gain profile [17, 18]. Furthermore, it was verified that the SDP effect is large for 980 nm band pumping when compared with the 1480 nm band pumping, which is considered small or negligible [13, 19].

In the steady–state regime, the effect of very low temperatures on the hole width was investigated in [20]. Temperature variations can lead to severe performance degradation in cascades of EDFAs, mainly at shorter wavelengths [21]. Several investigations regarding the impact of temperature also indicate that using pump wavelengths around 1480 nm leads to larger variations of gain and noise figure, as opposite to pumping at around 980 nm [22, 23]. Furthermore, it has also been shown that the gain in the L–band is generally more sensitive to temperature changes of the erbium–doped fiber (EDF) coil than the gain in the C–band [24]. Available models for spectral hole burning [11, 25] still cannot provide answers to several questions related to the influence of different physical parameters, such as temperature. Thus, conducting experiments is often still the only way to characterize these effects.

This chapter is organized as follows. Section 5.2 describes the experimental assessment of the dependence of the dynamic response of an EDFA due to SHB and SDP on pump wavelength, pump power and temperature. Afterwards, in Section 5.3, we derive and propose a model which incorporates the SDP effect in a two–level model of an EDFA. With the proposed model, the dependence of the gain on the pump wavelength is taken into account, for pumps wavelengths around 1480 nm. Experimental measurements of the dependence of gain fluctuations on pump wavelength, pump power, and channel power are presented and discussed. In Section 5.4, we investigate the behavior of SHB and SDP in an EDFA with ideal gain control for different pump wavelengths around 980 nm and spectral allocation of input channels. The conclusions of this chapter are presented in Section 5.5.

5.2 Measurements of the Dynamic Response of an EDFA

Typically, the effect of SHB and SDP becomes clearly noticeable only in a cascade of amplifiers. Therefore, in order to obtain a measurement signal that can be measured with enough accuracy given the limitations of the experimental setup implemented, such as low signal power signals at the input of the EDFA, the single EDF used in our experiment is operated at a very low gain. This way, a high compression is achieved and the gain variations induced by SHB and SDP became more pronounced [11].

5.2.1 Dependence on the Pump Wavelength and Pump Power

A schematic diagram of the implemented experimental setup, which is based on [15], is shown in Fig. 5.1. We improve the switching device in order to decrease the probe fluctuations caused by switch imperfections. One probe channel at 1531.3 nm and one pump lightwave with variable wavelength co–propagate through an EDF of 10 m length. Ten additional polarization scrambled channels are launched into the EDF. Depending on the position of a fast 2x1 switch with transient time below 1 μs, the channels are located either on the blue side or on the red side of the C–band. At the output of the EDF, the pump and the additional channels are suppressed by an optical filter. Power fluctuations of the probe channel are detected by a photodiode and a digital oscilloscope.

The input powers of the probe and the ten additional channels in the blue subband equals -11 dBm per channel. The power of the ten channels in the red subband is adjusted in such a way that the probe channel experiences equal gain independently of the switch position on steady–state conditions. In case of a switching time significantly smaller than the time constant of the EDFA, power transients due to a change of the average population inversion can be completely eliminated. In the discussion of the results, the impact of imperfections of the switch on the measurement results is considered.

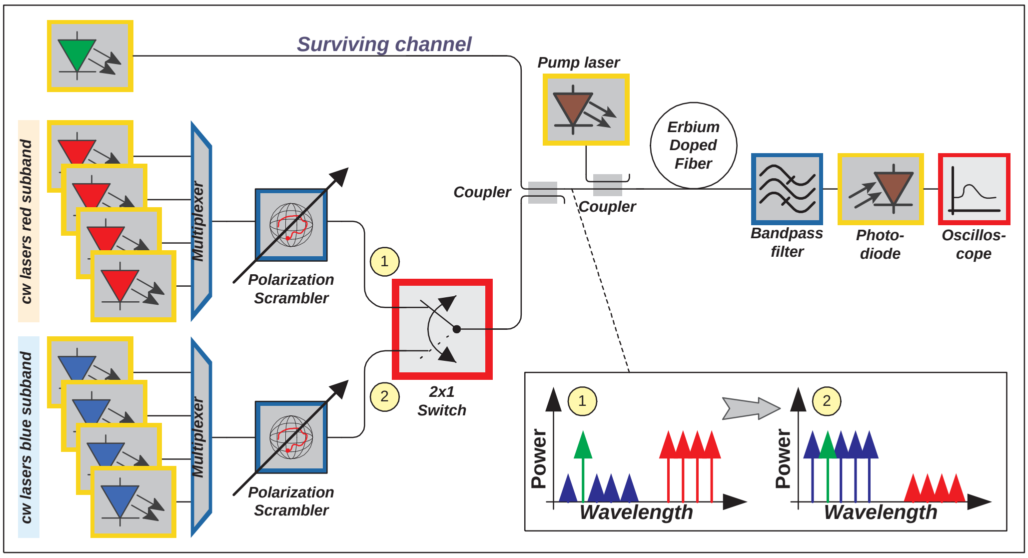

Figure 5.1: Experimental setup used for characterization of the dynamical properties of SHB and SDP.

Dependence on the Pump Wavelength

The dynamic response of the amplifier is measured when switching from the red subband channels to the blue subband. Since the goal is to assess the pump wavelength dependency, the gain of the probe channel remains unchanged during the series of measurements. This is achieved by adjusting the pump power at several pump wavelengths to yield the reference gain of the probe channel. The pump power launched into the EDF is in the order of magnitude of 10 mW. The pump wavelength dependency is determined by using different pumps. In addition to several pumps with emission wavelengths in the 1480 nm range, a pump at 980 nm is also taken into consideration. In the latter case, population of the third energy level comes into play, whereas a two level model is sufficient when pumping in the 1480 nm range.

Temporary gain variations induced by SHB and SDP are shown in Fig. 5.2 for different pump wavelengths. For pump wavelengths around 1465 nm and 1480 nm, there are small differences regarding the magnitude of these variations, with slightly larger variations for smaller pump wavelengths. In addition, the magnitude of the gain variations drops by approximately 20 % when using 1495 nm pumping instead of the 1480 nm pump wavelength. For comparison purposes, gain variations for a 980 nm pump are also shown. In contrast to the configuration with 1480 nm pumping, the magnitude almost doubles, which corresponds to an increase of 0.08 dB.

Additional measurements and investigations have been performed, in order to

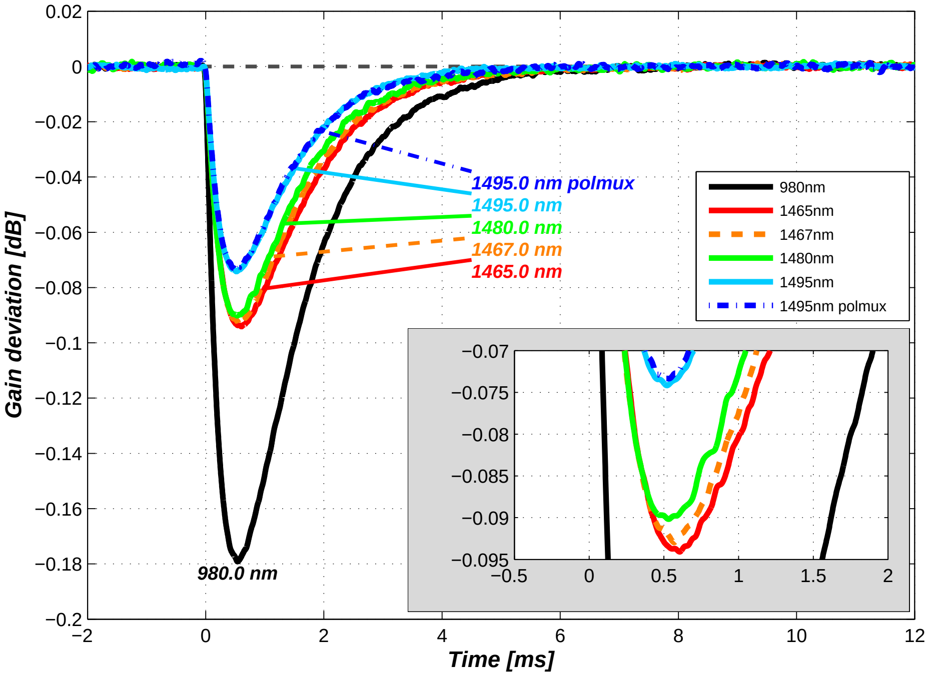

Figure 5.2: Measurement results showing gain variations induced by SHB and SDP for different pump wavelengths. Details of the curves within the first 2 ms are illustrated in the inset.

prove that the observed gain variations are, in fact, due to SHB and SDP. First, the single pump at 1495 nm is replaced by two polarization multiplexed pumps at the same wavelength. The corresponding curve in Fig. 5.2 labeled “1495 nm polmux” confirms that polarization effects such as polarization hole burning (PHB) play no role in our experiment.

Some fluctuations may also result from the redistribution of the population probability of the metastable level, called inversion in the following. Simulations are performed using the Giles model [7] introduced in Section 2.4.1 without considering the SHB and SDP effects, in order to investigate the possible impact of the redistribution of the inversion along the fiber. Fig. 5.3 shows the inversion along the fiber axis for several time instants of the transition. The two broader lines in the figure represent the two switch positions on steady–state conditions. In both cases the average value of the inversion is identical. Switching from the red to the blue subband channels will cause a redistribution of the population inversion of the amplifier, with the intermediate distributions displayed in light gray. Since the speed of the redistribution might be different at the different locations, some temporary variation of the average inversion, resulting in gain variations, might occur. Additionally, the switch from the red subband to the blue subband is not ideal. As illustrated in the inset of Fig. 5.4, there is a short term drop in the input power. These power drops can give rise to some overshoots. The quantification of the contribution of these two potentially disturbing effects can be performed by simulating the dynamic response of the two–level EDFA without considering the SHB and SDP effects. Simulation results displayed in Fig. 5.4 reveal that the contribution of the temporary input power drop, as well as the redistribution of the inversion to the overall gain variations, is in the order of 10^{-3} dB, and thus negligible.

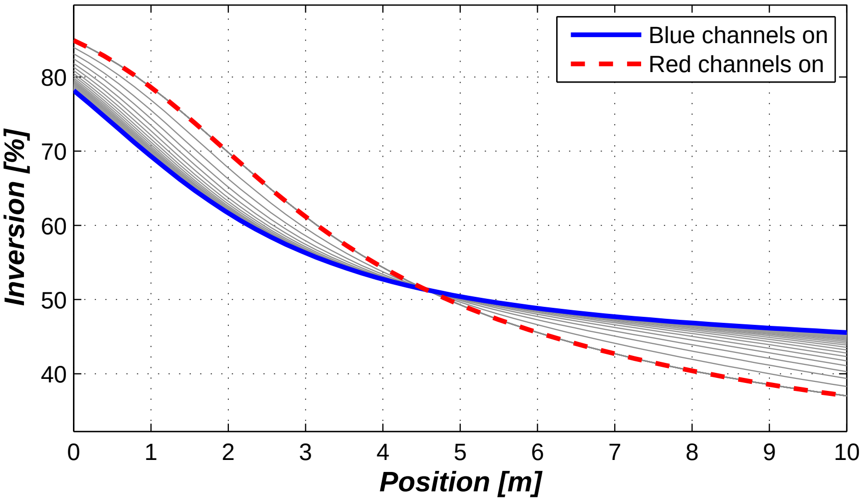

Figure 5.3: Distribution of the inversion along the EDF length for the two switch positions. Gray curves show intermediate distributions during the transient event.

In summary, the results clearly demonstrate that the measured gain variations have to be assigned to the SHB and SDP effects. The magnitude of gain variation for pumping at 980 nm is almost twice the value observed in the case of pumping in the 1480 nm range. Furthermore, the experiment revealed that there is also a pump wavelength dependency in the 1480 nm range.

Dependence on the Pump Power for 1480 nm Pumping

In order to investigate the influence of the pump power dependency on SHB and SDP dynamics, we maintain the powers of the signals and the probe channel at the input of the amplifiers at the same level. However, the pump power at 1480 nm has been varied from 7 mW to 57.2 mW. Results presented in Fig. 5.5 show a maximum gain variation of about 0.13 dB for the smallest considered pump power of 7 mW. With larger pump powers, the magnitude of the gain variations decreases and drops to slightly less than 0.04 dB, at a pump power of 57.2 mW. This is expected since it has already been shown

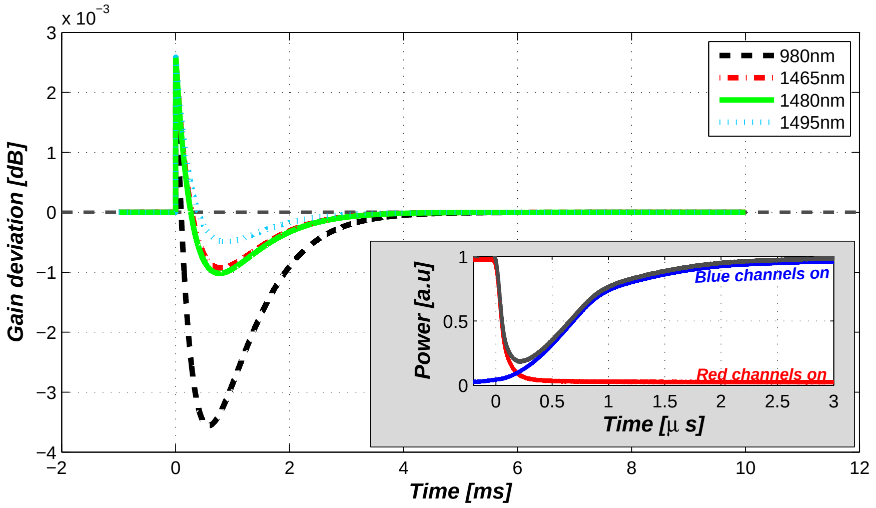

Figure 5.4: Gain variations originating from the redistribution of the inversion along the axis of the EDF and the intermediate total input power drop (simulation results without SHB and SDP). The inset shows the non–ideal switching from the red subband to the blue subband.

---

in steady–state experiments that the depth of SHB and SDP induced holes decreases with decreasing compression. However, this experiment shows that this rule is also applicable to SHB and SDP dynamics.

At zero, on the time axis, a narrow peak caused by the intermediate input power drop for higher pump powers can be observed. The magnitude of this peak increases with increasing pump power due to the fact that EDFA dynamics becomes faster at larger pump powers [26]. For verification purposes, simulations neglecting SHB and SDP are performed using the Giles model [7]. Dashed curves added to the aforementioned figure represent the obtained numerical results. The comparison of the experimental data (solid curves) and simulation results (dashed curves) reveals a good agreement, regarding the magnitude of the peak, and confirms the above drawn conclusions. With higher pump powers, the gain variations induced by SHB and SDP become narrower. Thus, similar to other transient effects in EDFs, dynamics of SHB and SDP becomes faster at higher pump powers.

5.2.2 Dependence on Temperature

A schematic diagram of the experimental setup implemented is shown in Fig. 5.6. In order to study the dependence of the dynamic response of SHB and SDP on temperature, the EDF coil is placed in a temperature chamber. The temperature ranges from -60°C to 100°C. A temperature sensor attached directly to the fiber provides accurate

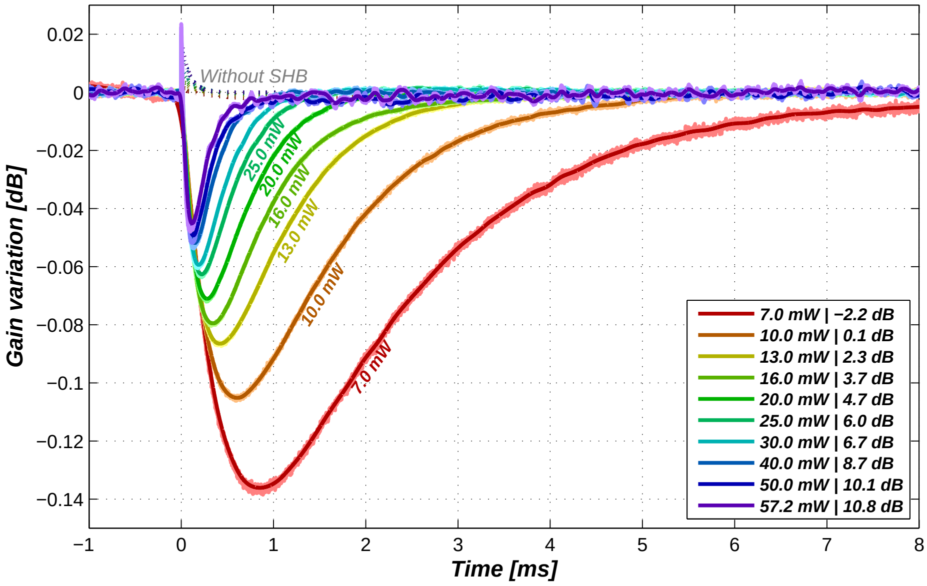

Figure 5.5: Gain variations for different pump powers at 1480 nm. Solid curves represent experimental data, whereas dashed curves show simulations results without SHB and SDP. In the legend, the used pump power, as well as the resulting amplifier gain, are indicated for each curve.

---

temperature measurements.

One probe channel centered at 1531.1 nm and one pump are co–propagating in a widely used commercial EDF with 10 m length. In addition, ten polarization scrambled signals are launched into the fiber. Depending on the switch position, they are either located on the blue side or on the red side of the C–band. The input power of the probe and of the other channels on the blue side of the C–band equals -8.0 dBm per channel, whereas the total power of the red band is adjusted to provide equal gain at the probe channel wavelength for both switch positions. Thus, the steady–state gain of the probe channel is identical for both switch positions. Throughout one run of the experiment the power levels of all involved laser diodes (all signals and pump) are constant. This way, any influence from control parameters is avoided. At the output of the EDF, the pump and the additional signals are suppressed by an optical filter (isolation >40 dB). The remaining power of the probe channel is detected by means of a photodiode. Using an oscilloscope, power variations of the probe channel at the output of the EDF are recorded.

Temperature variations lead to changes of the cross sections for emission and absorption. Thus, amplifier gain and pumping efficiency changes. Since gain compression will influence the impact of SHB and SDP [11], this effect has to be canceled out, in

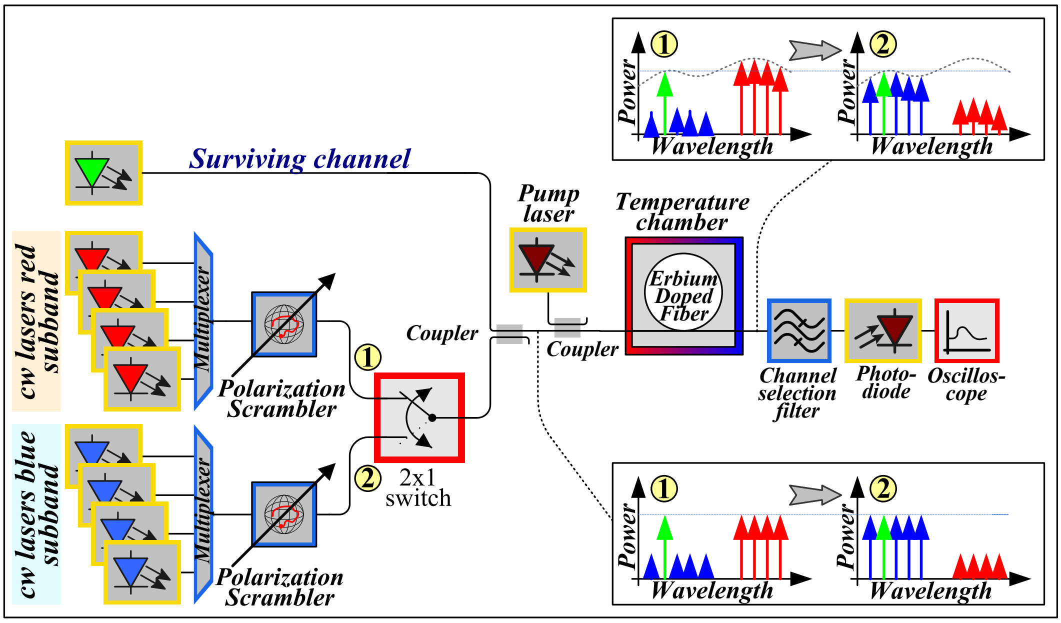

Figure 5.6: Experimental setup used for characterization of the dynamical response of SHB and SDP at different temperatures.

order to only analyze the effect of SHB and SDP. To keep the gain compression constant, the input pump power is readjusted for each trial, providing always the same gain for the probe channel.

Depending on the pump wavelength, different energy levels of the erbium ions are involved in the amplification mechanism. When using pump light around 1480 nm, only the lowest two energy levels (ground level $^4I_{15/2}$ and metastable level $^4I_{13/2}$) are relevant. However, a third energy level $^4I_{11/2}$ comes into play if the pump wavelength λ_{pump} is close to 980 nm. In the following, experimental data for both pump wavelengths are presented. Independently of the pump wavelength, the pump power is adjusted to provide almost zero gain (0.4 dB) for the probe channel.

The plot on the left side of Fig. 5.7 shows the temporary gain deviations due to SHB and SDP for different coil temperatures, ranging from -36 °C to 64 °C and for pumping at 1480 nm. These gain variations can be well fit by two exponential functions with time constants around 0.3 ms and 0.9 ms, respectively. When using a pump wavelength of 980 nm, the smaller time constant increases with increasing temperature and changes by up to ±15 % within the considered temperature range. In contrast, the larger time constant barely changes for temperatures below 24 °C, and decreases slightly at higher temperatures (maximum variation 6 %). When using a 1480 nm pump, the maximum variation of the time constants is smaller (maximum variation 8 %). Moreover, both time constants show a trend to larger values with increasing temperature.

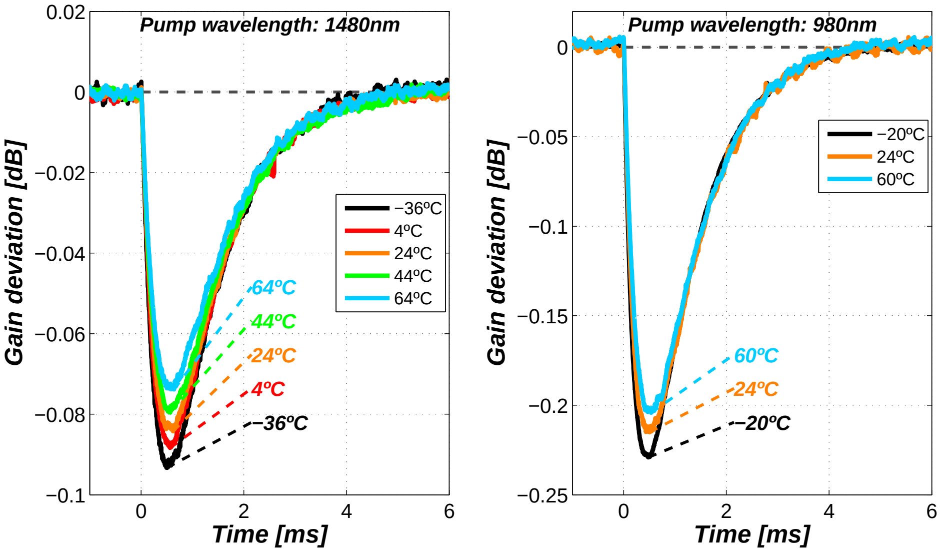

Figure 5.7: Measurement results showing gain deviations induced by SHB and SDP at different temperatures for an EDF pumped at 1480 nm (left side, two energy levels involved) and 980 nm (right side, three energy levels involved).

The magnitude of the peak value of the undershoot diminishes with increasing temperature. The transition time is only slightly dependent on temperature (maximum deviation from value at 24 °C: 5.2 %) with a trend to increased values for increasing temperature. It takes approximately 3.2 ms for the gain to return to the steady–sate value (deviation less than 10 % of peak value). The correspondent results for a pump wavelength of 980 nm are represented on the right side of Fig. 5.7. Again, the peak value of the undershoot decreases with increasing temperature and the transition time (≈3.0 ms) is similar to the time determined for 1480 nm pumping. The dependence of the transition time on temperature is very weak (maximum variation 3.5 %).

The maximum magnitude of the undershoots versus temperature is illustrated on the left side of Fig. 5.8 for both pump wavelengths. On the right side, the deviation of the maximum magnitude from the value at 24 °C is shown. For 980 nm pumping, the measurement data can be well fitted by a linear function with a slope of 3.1×10^{-4} dB/°C. Comparing to the linear fit function, a polynomial of degree three provides a better fitting for a pump wavelength of 1480 nm. The slope of the resulting curve equals 2.2×10^{-4} dB/°C at 24 °C. Thus, the temperature dependence is by a factor of 1.4 larger when using a 980 nm pump. Taking into account the fact that the absolute magnitude is larger by a factor of 2.7 for the three level system, the relative change of the peak value with temperature is smaller for pumping at 980 nm. It is determined a relative change of 0.145 %/°C, for a pump emitting light at 980 nm, whereas the relative change equals 0.26 %/°C for pumping around 1480 nm.

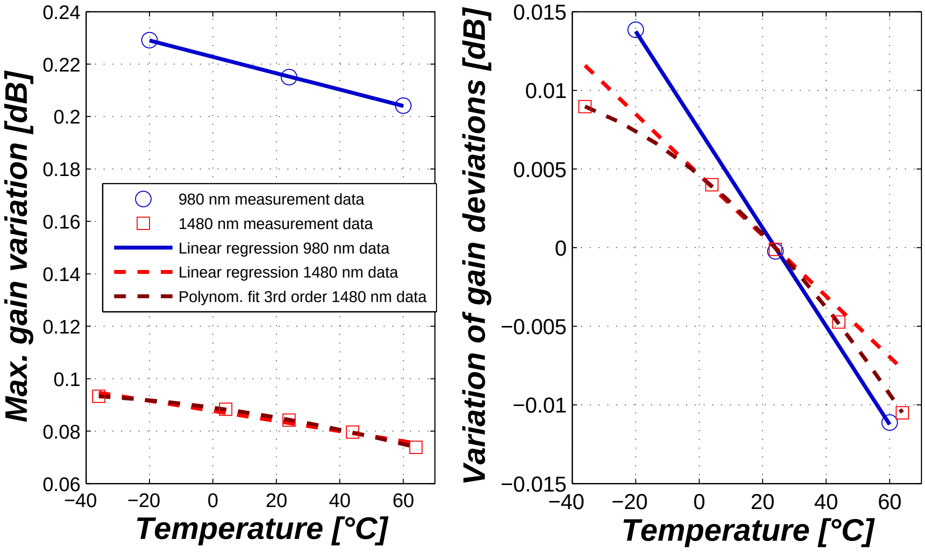

Figure 5.8: The left side plot indicates the maximum magnitude of gain deviations versus temperature for an EDF pumped at 980 nm and 1480 nm, respectively. The right side plot shows the deviation of the maximum magnitude of the gain deviation of each measurement regarding the maximum magnitude measured at 24°C.

Stabilizing the EDF coil temperature at around 25 °C is advantageous when considering the pumping efficiency [22]. However, this solution requires the implementation of heating and cooling capabilities. Therefore, the set point of the temperature quite often corresponds to the maximum temperature that might occur during operation. Typically, this temperature value is around 55 °C. In this way, a simple heater is sufficient. The presented investigation reveals that this solution is also advantageous when considering the magnitude of dynamic gain variations induced by SHB and SDP.

5.3 Site Dependent Pumping Effect on Two–level EDFA

In Section 5.2, the dependence of the dynamic response on the pump wavelengths around 1480 nm is measured. These results show that, in addition to SHB, there is another source of statistical variations in the amplifier related to the pump wavelength, even when pumping an EDF at wavelengths around 1480 nm. Experimental work presented in [19] suggests that this behavior is due to the effect of SDP induced by wavelengths in the 1480 nm range.

5.3.1 Two–level Model Considering SHB and SDP Effects

As presented in Section 2.4.1 when considering the statistical variations for the two–level model, we obtain

$$\frac{\partial \bar{I}_k}{\partial z} = u_k\Big\{ \left(\bar{\sigma^a}_k + \bar{\sigma^e}_k\right)\left(\bar{N}_2 + n_2^k\right) - \bar{\sigma^a}_k \Big\}\bar{I}_k + u_k m \bar{\sigma^e}_k (\bar{N}_2 + n_2^k)\Delta\nu_k/\zeta, \tag{5.1}$$

$$\tau_2 \frac{\partial \bar{N}_2}{\partial t} = -\bar{N}_2\Big(\sum_k^{N_{\text{tot}}} \bar{\sigma^e}_k \bar{I}_k + \sum_k^{N_{\text{tot}}} \bar{\sigma^a}_k \bar{I}_k + 1\Big) + \sum_k^{N_{\text{tot}}} \bar{\sigma^a}_k \bar{I}_k - \sum_k^{N_{\text{tot}}} \left(\bar{\sigma^a}_k + \bar{\sigma^e}_k\right) n_2^k \bar{I}_k, \tag{5.2}$$

where,

$$n_2^k = \langle \Delta N_{2,i} \xi_{k,i} \rangle_i, \tag{5.3}$$

and

$$\tau_2 \frac{\partial n_2^k}{\partial t} = -n_2^k\Big(\sum_{j=1}^{N_{\text{tot}}} \bar{\sigma^e}_j \bar{I}_j + \sum_{j=1}^{N_{\text{tot}}} \bar{\sigma^a}_j \bar{I}_j + 1\Big) - \bar{N}_2(A_k^* + B_k^*) - B_k^*), \tag{5.4}$$

where the following quantities were defined

$$A_k^* \equiv \sum_{j=1}^{N_{\text{tot}}} \bar{\sigma^e}_j I_j \Gamma(k,j), \tag{5.5}$$

$$B_k^* \equiv \sum_{j=1}^{N_{\text{tot}}} \bar{\sigma^a}_j I_j \Gamma(k,j), \tag{5.6}$$

$$\Gamma(k,j) = \left\langle \xi_{k,i} \xi_{j,i} \right\rangle_i . \tag{5.7}$$

In order to include the pump dependency verified in the experimental results presented in Section 5.2, we have to include the pump wavelengths in N_{tot}. Following, we can separate the total number of wavelengths, N_{tot}, in two subgroups: one related to the pump wavelengths, where N_{p} is the number of pump wavelengths, and the other related to the signal wavelengths or ASE noise, where $N_{\text{sig/ASE}}$ is the number of signal wavelengths or the ASE noise channels. By separating the pump and signal wavelengths we obtain

$$A_k^* \equiv \sum_{s=1}^{N_{\text{sig/ASE}}} \bar{\sigma^e}_s \bar{I}_s \Gamma_s(k,s) + \sum_{p=1}^{N_{\text{p}}} \bar{\sigma^e}_p \bar{I}_p \Gamma_{14xx}(k,p), \tag{5.8}$$

$$B_k^* \equiv \sum_{s=1}^{N_{\mathrm{sig/ASE}}} \bar{\sigma^a}_s \bar{I}_s \Gamma_s(k,s) + \sum_{p=1}^{N_{\mathrm{p}}} \bar{\sigma^a}_p \bar{I}_p \Gamma_{14xx}(k,p), \tag{5.9}$$

and

$$\Gamma_s(k,s) = \left\langle \xi_{k,i}\xi_{s,i} \right\rangle_i, \tag{5.10}$$

$$\Gamma_{14xx}(k,p) = \left\langle \xi_{k,i}\xi_{p,i} \right\rangle_i, \tag{5.11}$$

where s and p are signals or ASE noise wavelengths of the C–band and pump wavelengths around 1480 nm, respectively. In eqs. (5.8) and (5.9), the first term takes into account the effect of the signal wavelengths present in the amplifier on the signal wavelength indexed by k, whereas the second term determines the influence of the pump wavelengths on this signal wavelength. Physically, we can associate the first term of eq. (5.8) and eq. (5.9) with the SHB effect and the second term of both equations with the SDP effect. Following this derivation, we need to characterize two correlation matrices to describe the system, one correlation matrix between wavelength k and the signals, $\Gamma_s(k,s)$ (eq. (5.10)), and a second correlation matrix between the signal k and the pump wavelengths, $\Gamma_{14xx}(k,p)$ (eq. (5.11)). The impact of SHB on the pumps, i.e. the impact of the pumps on itself, is neglected. Methods to obtain these correlation matrices are presented in the Section 5.3.2.

Note that eq. (2.20) and eq. (2.21) are particular cases of eqs. (5.1) and (5.2), respectively, neglecting statistical variations of the optical characteristics of the ion sub–ensembles, i. e. $\sigma^e_{k,i} = \bar{\sigma^e}_k$, $\sigma^a_{k,i} = \bar{\sigma^a}_k$ and $N_{2,i} = \bar{N}_2$. Also, if we set $\Gamma_{14xx}(k,p)$ to zero in eqs. (5.8) and (5.9), meaning that we do not consider a dependence of the statistical variations on the pump wavelength, we obtain the model presented in Section 2.4.1, referred as the two–level model with SHB [11]. In Section 5.3.3, we will compare the predictions of the model without SHB and SDP [7], the prediction of the model with SHB [11], and the predictions of the proposed model with SHB and SDP, with experimental results.

5.3.2 Correlation Matrices $\Gamma_s(k,s)$ and $\Gamma_{14xx}(k,p)$

In order to implement the proposed model, we need to independently characterize two correlation matrices, one related to the SHB effect and another related to the SDP effect. This is performed by isolating the two effects.

In Section 2.4.1, we characterized the correlation matrix between the signals, $\Gamma_s(k,s)$, using the modified spectral subtraction technique presented in [11]. Since both spectra are measured using the same pump wavelength and power, they are similarly affected by the SDP effect. Therefore, when subtracting them we are minimizing the impact of the SDP effect on the final result. Because of this, it is possible to describe the spectral difference with $\Gamma_p(k,p) = 0$, i.e. using only the correlation matrix $\Gamma_s(k,s)$. With the knowledge of $\Gamma_s(k,s)$ we have a model capable of predicting the amplifier behavior considering the SHB effect. Of note, the results obtained so far only describe accurately the difference between spectra of an EDFA, when maintaining the same pump power and wavelength. When using different pump powers or pump wavelengths, deviations are observed, which means that the SDP effect needs to be taken into account.

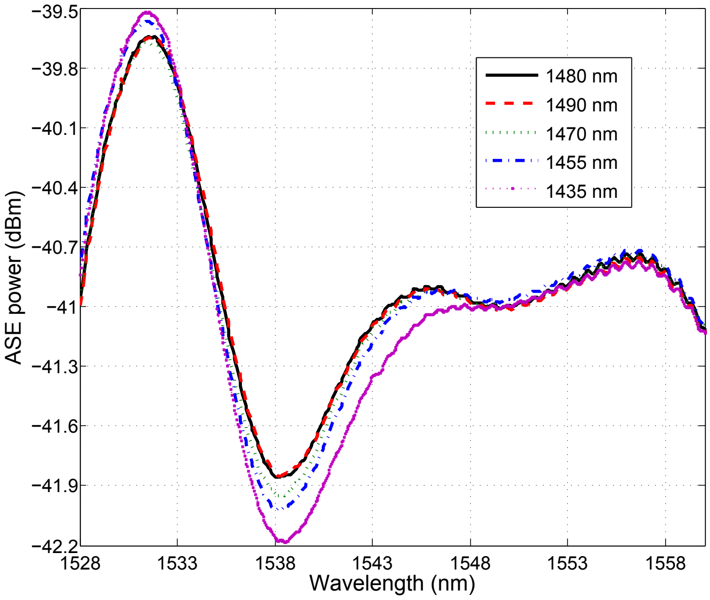

Figure 5.9: ASE noise spectra measured for pumps placed at 1435 nm, 1455 nm, 1470 nm, 1480 nm and 1490 nm, considering a spectral resolution of 0.05 nm.

The determination of the second correlation matrix is also based on ASE noise spectra. For this purpose, we use a low power signal co–propagating with a pump placed at 1480 nm with 10 mW of input power into a 10 m EDF. The low power signal is used to monitor the gain of the amplifier and is placed at 1564 nm, with -10 dBm of input power. We chose 1564 nm, because it is located on the spectral region where the SHB effect is negligible [11], and therefore the ASE noise is not affected by the SHB effect due to the presence of this signal. We measured the optical power of the ASE noise spectrum with an optical resolution bandwidth of 0.05 nm. We repeat the measurements for additional pump wavelengths (1435 nm, 1455 nm, 1470 nm, and

1490 nm). Due to the pump efficiency dependence on the pump wavelength, we need to adjust the pump power to keep the gain constant for the reference signal. In order make sure that the ASE noise spectrum closely follows the gain of the amplifier, the EDF is operated at high average inversion of the active fiber. Fig. 5.9 shows the ASE noise spectrum of the amplifier for all used pump wavelengths. We can observe that each pump wavelength produces a different ASE noise spectrum. Such variations reflect the presence of the SDP effect, but modifications of the inversion profile can also influence the ASE noise spectrum. In general, the inversion profile depends on the powers and wavelengths of all interacting lightwaves. Redistribution of the inversion level induced by changing the signal wavelength has been illustrated in [1]. Similarly, changing the pump wavelength also leads to a modified inversion profile, which finally results in a modified ASE noise spectrum, although the average inversion is stabilized at a constant level.

In order to characterize SDP, it is important to separate the contribution of this effect from other known effects. Therefore, we determine the difference between the measured ASE noise spectrum and the ASE noise spectrum obtained from simulations for each pump wavelength. The simulation results already include the dependence of the ASE noise spectrum on the distribution of the inversion along the active fiber and the SHB effect. The first effect is already taken into account by the basic equations provided in [7] and SHB has been implemented in the simulation tool following the technique described in [11]. Thus, these effects cancel out and deviations between experimental data and simulation results are in principle only due to the SDP effect. In the following, the correlation matrix $\Gamma_p(k,p)$ is adapted to match the simulation results with the experimental data.

Since the relationship between the ASE noise spectrum and the corresponding line of the correlation matrix is monotonous but not strictly linear, we apply an iterative procedure described in the following. In the beginning, we start with a correlation matrix with all elements initialized to zero. During one iteration, we simulate the resulting ASE noise spectrum for the current correlation matrix, determine the difference of measured and calculated ASE noise spectra for a pump with a given wavelength indexed by p, and add this difference multiplied by a scaling factor to the column p of $\Gamma_p(k,p)$. The value of the scaling factor is chosen to be smaller than the value required to eliminate the difference completely. Thus, convergence of the technique is guaranteed. This step is repeated iteratively until a stopping criterion is fulfilled. The stopping criterion has been chosen to ensure a maximum deviation of 10^{-5} dB between the spectra, for wavelengths from 1528 nm to 1566 nm. This process is repeated for all pump wavelengths.

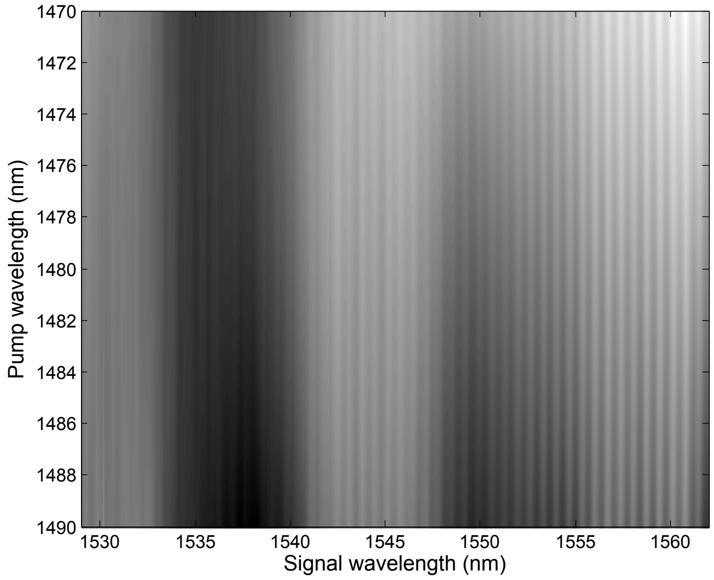

Figure 5.10: SDP correlation matrix, $\Gamma_p(k,p)$, between pump wavelengths p and signal wavelengths k. The $\Gamma_p(k,p)$ comprises values in between 0.0005 (white) and 0.0783 (black).

In Fig. 5.10, the SDP correlation matrix between the wavelengths of the pump and the signals, $\Gamma_p(k,p)$, is shown. Due to the fact that pump wavelengths shorter than 1470 nm and longer than 1490 nm have low efficiency and that the noise figure is significantly increased [27], we exclude this wavelength range from the characterization of the correlation matrix. Experimentally, we consider pumps at 1470 nm, 1480 nm, and 1490 nm. In order to increase the resolution of the correlation matrix, we perform a linear interpolation to the matrix values between the measured pump wavelengths.

5.3.3 Experimental Validation and Discussion

The schematic diagram of the implemented experimental setup is presented in Fig. 5.11. A surviving channel placed at 1531.2 nm is launched into a 10 m EDF. The signal is multiplexed with a co–propagating pump, placed either at 1470 nm, 1480 nm, or 1490 nm. An additional channel is added to the amplifier and, depending on the position of two synchronized fast switches, with switching times below 1 μs, this signal is located either on the blue side or on the red side of the C–band. By adjusting the power of the red channel, the surviving channel experiences the same gain, independently of the switching position, when reaching steady–state conditions. At the output of the amplifier, several filters are used to separate the surviving channel from the other channels and the pump (suppression > 40 dB). The time evolution of the surviving channel is recorded with a digital oscilloscope (OSC). The input power of the pump is set to provide a low gain for the surviving channel in order to obtain a large compression, which allows to measure SHB and SDP with high sensitivity [15]. With this setup, it is also possible to perform subband switching from 10 channels on the blue subband of the C–band, to 10 channels on the red subband of the C–band and vice–versa, as we will discuss later.

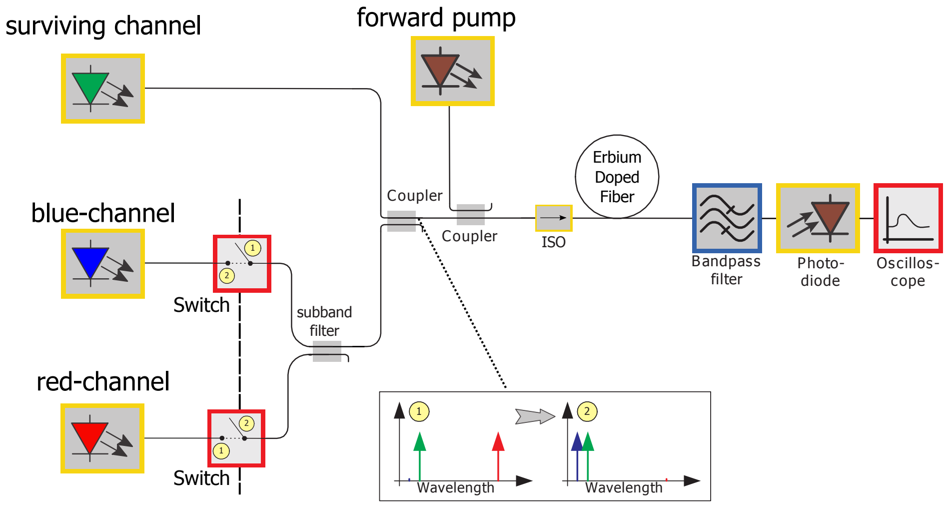

Figure 5.11: Experimental setup implemented to measure the power excursion of the surviving channel due to the variation of the input signal spectrum in a co–pumped EDFA.

We measure the power excursion of the surviving channel, defined as the difference between the transient and the steady–state responses, when switching between the blue and red channel and vice–versa. Since the gain of the surviving channel is constant, the power excursion of the surviving channel is attributable to SHB and SDP.

Subband Transitions With a Single Channel in Each Subband

In the first set of measurements, we measure the power excursion of the surviving channel at the output of the EDF for different pump wavelengths, blue channel powers and pump powers. We use a blue channel placed at 1530.1 nm and a red channel placed at 1564 nm. Note that the input signal power of the red channel is always adjusted, in order to keep the steady–state gain of the surviving channel equal to the gain of the surviving channel when the surviving channel is co–propagated with the blue channel.

Pump Wavelength Dependence

In this experiment, we measure the power excursion of the surviving channel when different pump wavelengths are used. The surviving channel, with -9 dBm of input optical power, is co–propagating with the blue channel, with 2 dBm of input optical power. We adjust the pump placed at 1480 nm to provide a gain of 1.5 dB for the surviving channel. Afterwards, we change the pump wavelength to 1490 nm and 1470 nm, and adjust the input pump power to provide the same gain for the surviving channel as before.

Figure 5.12 shows the power excursion of the surviving channel, when using a pump placed at 1480 nm, 1470 nm, and 1490 nm, for the transition from the red channel to the blue channel (on the left) and from the blue channel to the red channel (on the right). These results are obtained either experimentally or by means of simulations, taking into account different combinations of the relevant effects. First, neither SHB nor SDP (simulation without SHB+SDP) are considered. In a second step, only the SHB effect (simulation with SHB) is taken into account. Finally, SHB and SDP are both included in the numerical calculations (simulation with SHB+SDP). The experimental results presented in Fig. 5.12 show a clear dependence of the power excursion on the pump wavelength. When analyzing the transition from the red channel to the blue channel, the power excursion of the pump placed at 1470 nm is 14% higher than the power excursion induced at a pump wavelength of 1480 nm. On the other hand, the power excursion for the pump placed at 1490 nm is 10% smaller. When observing the simulated results without considering the SHB and SDP effects, no power excursion is predicted. This happens because, by keeping the gain of the surviving channel constant, the input power variation does not induce changes of the average inversion and, thus, no excursion is predicted. Considering only the SHB effect, the power excursion is clearly visible. However, the obtained curves do not describe accurately the maximum power excursion of the surviving channel or the dependence on the pump wavelength. Simulations including SHB and SDP reveal that the power excursion for the pump placed at 1480 nm is correctly described for both transitions. Furthermore, the increase of the power excursion of the pump placed at 1470 nm is also correctly estimated, and the same applies for the decrease of the power excursion due to the use of the pump placed at 1490 nm. Additionally, when analyzing at both transitions, the power excursions provided by the model are not symmetrical in terms of maximum deviation and transition time, which is also observed in the experimental results. By comparing with the experimental measurements, we confirm that the proposed model accurately describes the maximum power excursions and the transient times, as well as the pump wavelength dependency.

There is a significant difference between the experimental results and the results predicted in the model considering SHB only. These results confirm that the SDP effect significantly influences the dynamics of amplifiers and needs to be considered

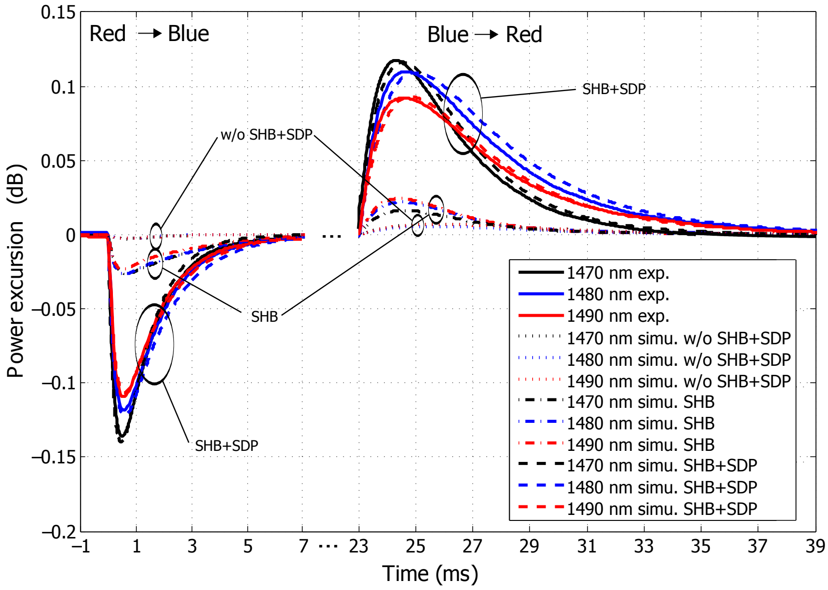

Figure 5.12: Power excursion of the surviving channel at the output of the EDF pumped at 1480 nm, 1470 nm and 1490 nm due to the transition from the red channel to the blue channel and vice–versa. Solid lines represent experimental data, whereas dotted lines illustrate simulation results without considering the SHB and SDP effects. Dash–dotted lines show simulation results when considering the SHB effect only, whereas dashed lines mark simulation results including SHB and SDP.

---

when pumping EDFs around 1480 nm.

Channel Power Dependence

In this experiment, we measure the impact of changing the input signal power of the blue channel on the power excursion of the surviving channel, for the transition from the red channel to the blue channel. We set the surviving channel input signal power to -5 dBm and the input signal power of the blue channel to 2 dBm. The pump placed at 1480 nm is adjusted to provide a gain of 1 dB to the surviving channel. For each measurement the blue signal input power is reduced by 2 dB and the pump power is adjusted to maintain the same gain.

In Fig. 5.13, the experimental and simulation results for different channel powers are presented. As we can observe, the experimental results show that as the blue channel power diminishes, the magnitude of power excursions also reduces. For a blue signal power of 2 dBm, the power excursion reaches -0.1 dB and for -2 dBm it reaches -0.06 dB. As the blue channel power is reduced, we can see that the transient time increases. This is due to the fact that we need to reduce the pump power to maintain the same gain for the surviving channel. Again, no power variations are predicted when neglecting SHB and SDP. When considering the simulation with SHB only, we can see that the general behavior is captured. However, the maximum power excursion and the transient times are not correctly described. On the other hand, when considering simulation results taking into account SHB and SDP, we can verify that they are accurately describing the experimental results in terms of maximum power excursion and transient times.

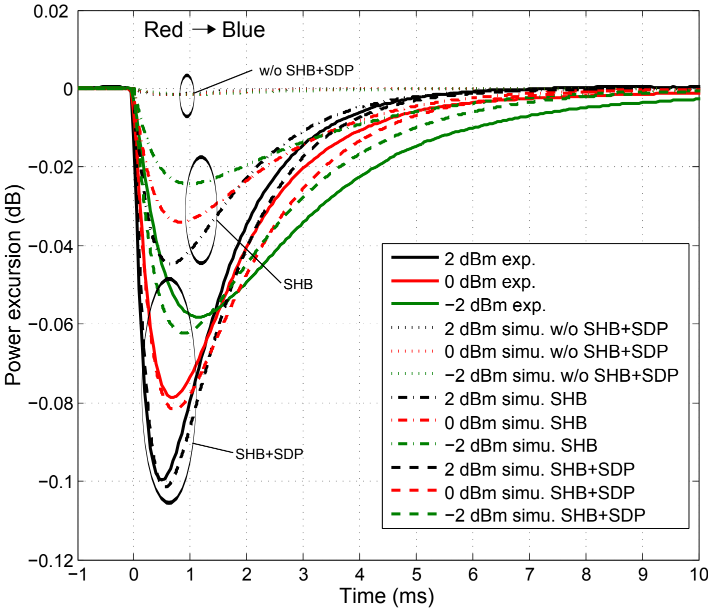

Figure 5.13: Power excursion of the surviving channel at the output of the EDF pumped at 1480 nm, due to the transition from the red channel to the blue channel, for blue channel powers of 2 dBm, 0 dBm, and -2 dBm. Solid lines represent experimental data; dotted lines illustrate simulation results without considering the SHB and SDP effects; dash–dotted lines show simulation results when considering the SHB effect; dashed lines visualize simulation results considering the SHB and SDP effects.

Pump Power Dependence in Configurations with Counter–Propagating Pumps

In this experiment, we investigate the behavior of EDFAs with counter–propagating pumps. The setup is similar to the one presented in Fig. 5.11, with the exception that the pump is launched into the EDF at the output and propagates within the EDF in opposite direction to the signals (see Fig. 5.14). The surviving channel has -9 dBm and the blue channel power has 2 dBm of input signal power. The pump wavelength is placed at 1480 nm and its power is increased in order to provide different gains for the surviving channel. The gain variations for the transition from the blue channel to the red channel are considered.

Figure 5.15 shows the maximum magnitude of the power excursion for the tran-

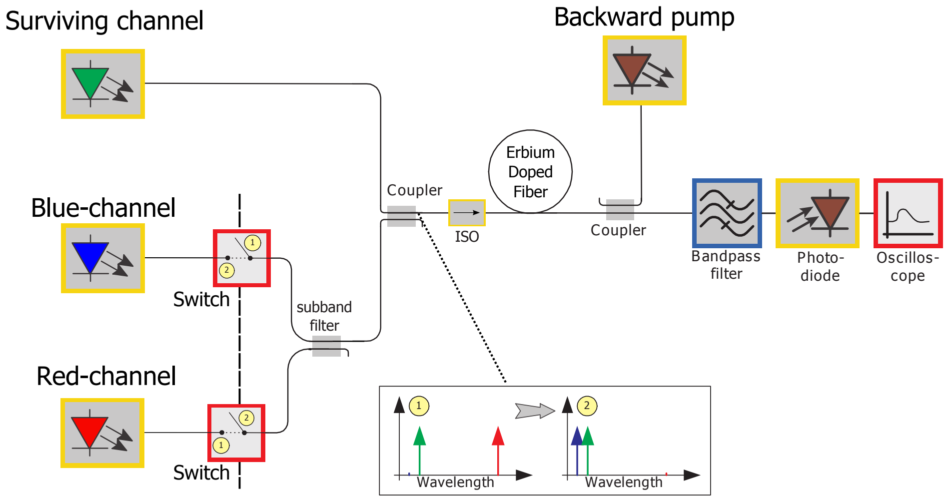

Figure 5.14: Experimental setup used to measure the power excursion of the surviving channel due to the variation of the input signal spectrum in an EDFA configuration with counter–propagating pump.

sition from the blue channel to the red channel, as the gain of the surviving channel increases. The maximum power excursion is the peak value of the power excursion curve, independently of the time point at which it is reached. The results are derived from experimental measurements (limited to 8 dB of gain due to experimental constrains), simulations neglecting SHB and SDP, simulations with the SHB effect, and simulations with the SHB and SDP effects. The experimental measurements show that, as the surviving channel gain increases, the power excursion decreases down to a certain gain where the overshoot becomes an undershoot. In contrast to the experimental data, simulation results neglecting SHB and SDP show almost no gain variations. When considering the SHB effect only, the maximum power excursions at lower gains are not correctly described. On the other hand, when comparing the experimental results with the proposed model including both SHB and SDP we can see that the model accurately describes the measurement results. As the gain increases, we verify that both models tend to vanishing power excursions. This happens because, as the pump power increases, the compression of the amplifier becomes smaller and thus the impact of SHB and SDP decreases. This is also the reason why the differences between both models decrease as the gain increases. This behavior is confirmed for other pump wavelengths and powers by repeating the experiment.

Subband transitions with 10 channels

In this subsection, instead of transmitting single high power channels in the blue and the red subband, we place 10 low power channels in each of the subbands. The first

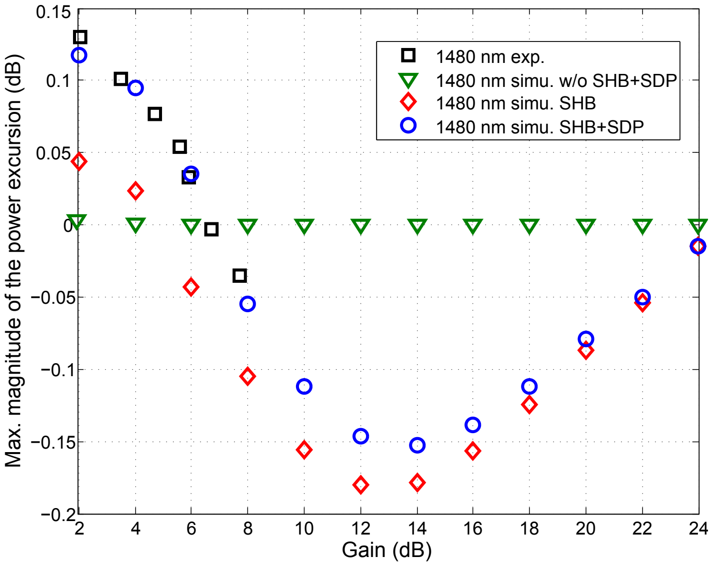

Figure 5.15: Maximum power excursion of the surviving channel at the output of the EDF pumped at 1480 nm, for the transition from the blue channel to the red channel for different gains. Squares are used for experimental data; inverted triangles indicate simulation results neglecting SHB and SDP; rhombuses stand for simulation results when considering the SHB effect only; circles illustrate simulation results when considering the SHB and SDP effects.

---

channel in the blue subband starts at 1529.1 nm and all channels have a uniform spacing of 50 GHz to their respective neighbors. The first channel of the red subband is located at 1554 nm and the same uniform channel spacing is applied. The signal power of the blue subband is around -11 dBm/channel and the surviving channel has -10 dBm of input signal power. The pump is co–propagating with the signal and it is placed at 1480 nm. The input pump power is adjusted to provide a gain of 1.5 dB.

Figure 5.16 shows the power excursion for the transition from the red subband to the blue subband (on the left) and from the blue subband to the red subband (on the right) obtained from experimental measurements, simulations without the SHB and SDP effects, simulations with the SHB effect only, and simulations including SHB and SDP. Simulation results without SHB and SDP reveal a small power excursion due to the adjustment of the inversion inside the EDF. Regarding the simulation with the SHB effect, we can see that the calculated power excursion deviates significantly from the experimental results. In particular, the transition from the blue to the red subband shows larger discrepancies. When the simulation is done considering the SHB and SDP effects, we can see that the model describes with good accuracy the red subband to the blue subband transition in terms of maximum power excursion and transient time. When observing the transition from the blue subband to the red subband we confirm that the measured results are accurately estimated by the model considering the SHB and SDP effects. Thus, with the above results, we show that the SDP effect needs to be included in order to accurately simulate both transitions. Also, we confirm that the proposed model is suitable for simulating a high number of channels in each subband.

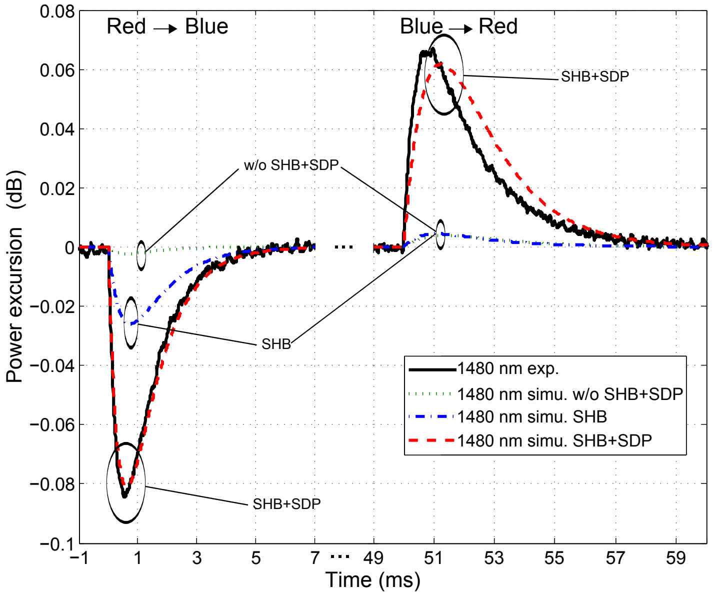

Figure 5.16: Power excursion of the surviving channel at the output of the EDF pumped at 1480 nm, due to the transition from the red channel to the blue channel and vice–versa. Solid lines represent experimental data, dotted lines stand for simulation results neglecting SHB and SDP, the dash–dotted lines represent simulation results when considering the SHB effect only, and, finally, dashed lines illustrate simulation results taking into account SHB and SDP.

5.4 Dynamic Response of EDFAs Pumped Around 980 nm

In this section we are interested in investigating the behavior of SHB and SDP in gain controlled EDFAs, in case of subband switch (see Fig. 5.17 (a)), and channels drop (see Fig. 5.17 (b)) by means of simulations using the model presented in Section 2.4.2. In all scenarios, it is assumed that the power add/drop happens within an infinitesimal short period of time. To control the transient effects resulting from input power variations, we implement an ideal feedforward control, which adjusts the pump power immediately after the event, to provide to the surviving channel on the steady–state conditions exactly the same amount of gain as before. In all scenarios we consider an EDFA stage with a single fiber with 10 m of length, pumped around 980 nm and with the described ideal feedforward control loop. The surviving channel is centered at 1531.3 nm, and the input power of the surviving channel and the other channels is -12 dBm/channel.

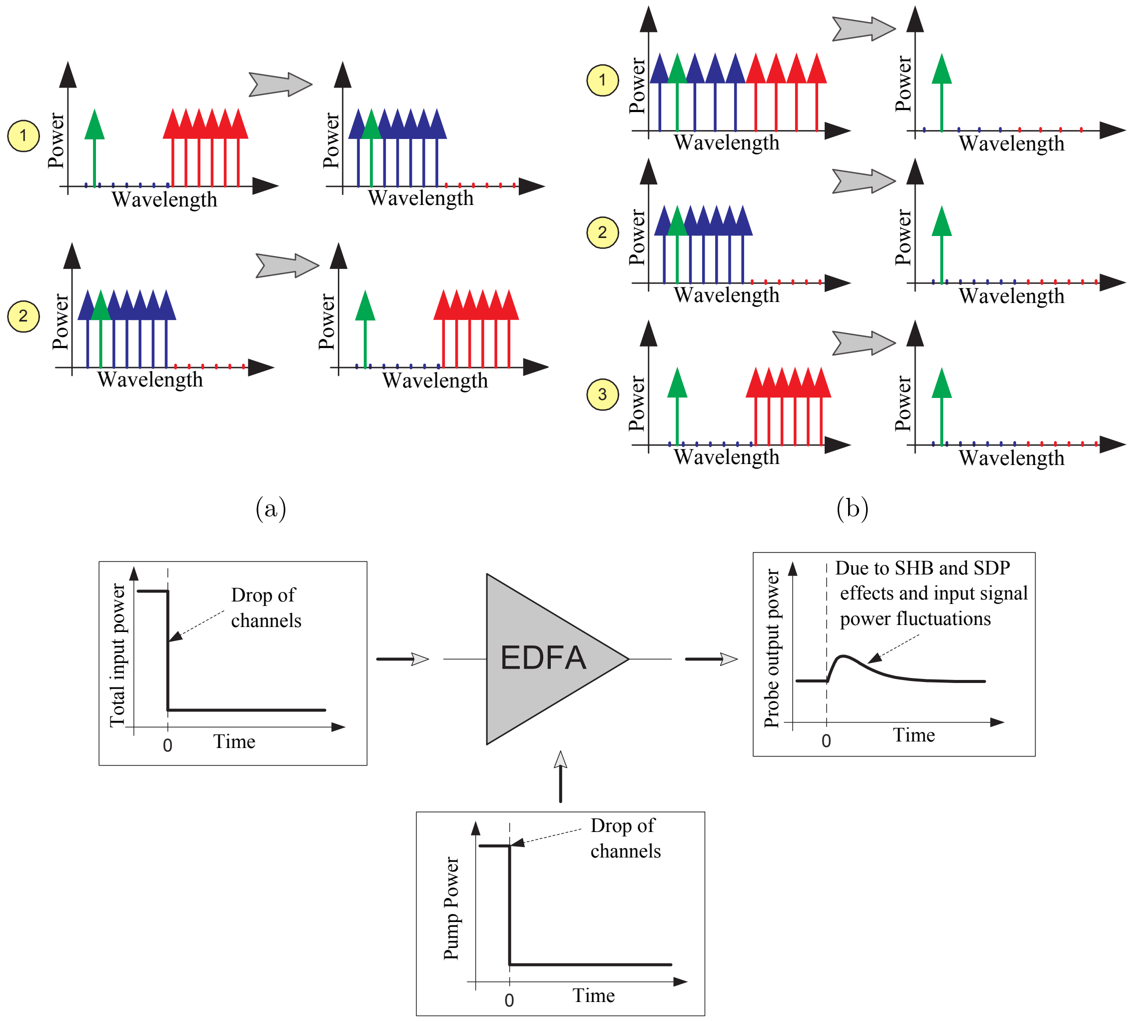

(a) (b)

(c)

Figure 5.17: a) Schematic diagram of the input channel profiles before and after the event for scenario 1) and scenario 2); b) Schematic diagram of the input channel profiles before and after the channel drop. c)Schematic diagram for an ideal power transient control system. At the add/drop event the pump power is instantly adjusted to maintain the gain of the surviving channels.

Figure 5.17 (c) shows a schematic diagram of an ideal feedforward gain control system. At the instant of the channel drop or add, the pump power is adjusted in order to maintain the same gain for the surviving channel. By doing so, we are mitigating the power transients due to input power variation in an ideal manner. However, some gain deviations can occur due to the re–arrangement of the local population inversion in the active fiber. Therefore, in order to extract the SHB and SDP behavior, we perform each simulation twice, one considering the SHB and SDP effects and the other without the effects. The power excursions of the surviving channel due to SHB and SDP are obtained when subtracting both simulations.

5.4.1 Behavior of the SHB and SPD Effects on Gain Controlled EDFAs

We start by investigating a subband switch from the red subband to the blue subband (scenario 1), and from the blue subband to the red subband (scenario 2), see Fig. 5.17 (a). We consider that 23 channels with a spacing of 100 GHz will be dropped from one subband and other 23 channels will be added in the other subband, at the same time instant.

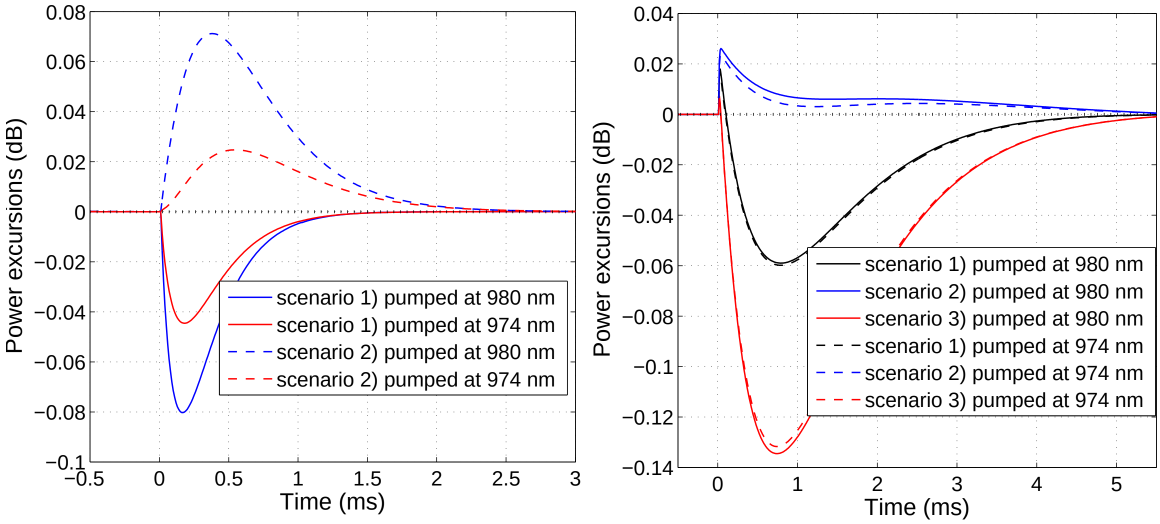

(a) (b)

Figure 5.18: a) Power excursions for the surviving channel at the output of the EDFA for scenario 1) pumped at 980 nm and 974 nm; and scenario 2) pumped at 980 nm and 974 nm; b) Power excursions for the surviving channel at the output of the EDFA pumped at 980 nm and 974 nm for the different channel profiles: scenario 1); scenario 2); scenario 3).

Figure 5.18 (a) shows the power excursions for the surviving channel when considering scenario 1) and scenario 2), see Fig. 5.17 (a), for a gain close to 3 dB for the surviving channel, when pumping at 980 nm and 974 nm. As shown, the power excursions induced by the pump centered at 980 nm are higher than for the pump centered at 974 nm. Also, when changing from the red subband to the blue subband, we have a higher deviation when compared with switching from the blue subband to the red subband.

After investigating the subband switch, we simulate a total channel drop and investigate how the spectral allocation of the input channels influences the dynamic response. Before the drop, 23 channels are co–propagated with the surviving channel, in different spectral regions of the C–band: scenario 1) uniformly distributed over all C–band; scenario 2) distributed on the blue subband with a channel spacing of 100 GHz; scenario 3) distributed on the red subband with a channel spacing of 100 GHz (see Fig. 5.17 (b)). After the drop, only the surviving channel is present. These scenarios are tested for a pump centered at 980 nm and 974 nm.

Figure 5.18 (b) shows the power excursion of the surviving channel, when changing the spectral location of the input channels, where the pump power is adjusted to provide a gain of about 15 dB for the surviving channel. The results clearly show that the spectral allocation influences the dynamic behavior of the amplifier. Therefore, depending on channels position before the drop, the dynamic response can have different behaviors. This is clearly seen when comparing scenario 2 and 3, where for the same gain we can have an overshoot or an undershoot. On the other hand, there is not a significant difference between pump wavelengths in the scenarios investigated.

In Fig. 5.19 we show the maximum overshoot and minimum undershoot for the scenarios 2) and 3) pumped at 980 nm, as function of the surviving channel gain. We can see that, for small gains, both scenarios only have overshoots, where scenario 2) has higher deviations. However, as the gain increases, the overshoot of scenario 2) decreases and higher undershoots appear on scenario 3).

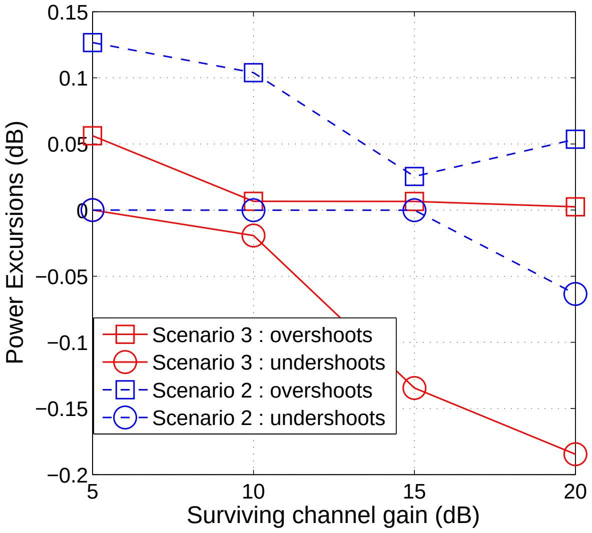

Figure 5.19: Maximum overshoot and minimum undershoot for the scenarios 2) and 3) pumped at 980 nm as function of the surviving channel gain.

5.5 Conclusions

In this chapter the dependency of the dynamics of EDFAs governed by SHB and SDP on pump wavelength and pump power was experimentally investigated. The magnitude of gain variations when pumping at 980 nm was almost twice the value observed in the case of pumping in the 1480 nm range. Furthermore, a small difference between 1465 nm and 1480 nm pumping was observed, whereas moving the pump wavelength to 1495 nm led to a decrease of the gain variations of approximately 20 %. In addition, it was shown that the magnitude of gain variations induced by SHB scales with gain compression, similarly to the depth of the spectral holes observed in steady–state experiments. Furthermore, data for different pump powers showed that dynamics of SHB becomes faster at higher pump powers.

Temperature dependency of the effect of SHB and SDP on the dynamics of EDFAs was investigated. It was shown that gain variations induced by SHB and SDP decrease with increasing temperature, independently of the number of involved energy levels of the erbium ions. The measurements results hereby presented reveal that an EDFA pumped at 980 nm is more sensitive to temperature variations than an EDFA using only two energy levels for signal amplification. However, the relative change is smaller for the EDFA using a pump wavelength of 980 nm. For a temperature variation of ±10 °C, the relative change of the maximum gain deviations equals ±2.6 % and ±1.45 % for the two and three–levels EDFA, respectively. We also verified that no significant difference with respect to transition time was observed. Furthermore, the transition time is only slightly dependent on temperature. This investigation showed that when operating the EDFA at a temperature value around 55 °C is also advantageous when considering the magnitude of dynamic gain variations induced by SHB and SDP.

Furthermore, we derived and presented a model that incorporates the SDP effect for the two–level system EDFA. The proposed model is based on a correlation matrix between the pump wavelength and the signals wavelengths, which takes into account the dependence of the gain spectrum on pump wavelength. Experimental measurements of the surviving channel power excursion were performed for several pump wavelengths, channel input powers and pump powers, and number of signals considered. By comparing the simulations results with the experimental measurements, we confirmed that the proposed model describes the measured power excursions with good accuracy. Moreover, the differences between simulation results and experimental data were significantly reduced when compared to simulations taking into account SHB only. Additionally, it was shown that obtaining accurate results for various operating conditions requires taking this effect into account, even if only two power levels of the erbium ions are involved.

Further simulations were performed to investigate the behavior of SHB and SDP in an EDFA with ideal gain control. We verified that in a subband switch, changing from the red subband to the blue subband causes higher deviations than when changing from the blue subband to the red subband of the C–band. Also, in a drop scenario, the overshoots and undershoots of the surviving channel depend higher on the input channels spectral allocation and on the gain of the amplifier than the pump wavelength.

References

[1] L. Rapp and J. Ferreira, "Dynamics of spectral hole burning in EDFAs: dependency on pump wavelength and pump power," *IEEE Photonics Technology Letters*, vol. 22, no. 16, pp. 1256–1258, Aug. 2010.

[2] J. Ferreira and L. Rapp, "Dynamics of spectral hole burning in EDFAs: dependence on temperature," *IEEE Photonics Technology Letters*, vol. 1, no. 24, pp. 67 – 69, Jan. 2011.

[3] J. Ferreira, D. Fonseca, P. Monteiro, A. Pinto, and L. Rapp, "Site Dependent Pumping Effect on Two-level EDFAs," *IEEE/OSA Journal of Lightwave Technology*, vol. 33, no. 2, pp. 285–292, Jan. 2015.

[4] J. Ferreira, D. Fonseca, P. Monteiro, and L. Rapp, "Dynamics of SHB and SDP on 9XX EDFAs: dependence on spectral allocation of input channels," in *Proc. International Conference on Transparent Optical Networks (ICTON)*, Jun. 2013, p. Th.A2.3.

[5] K. Ennser, T. Rogowski, G. Sacchi, M. Ibsen, O. Quargnolo, J. Shmulovich, G. Della Valle, and S. Taccheo, "Power transients control in transparent WDM networks," in *Proc. International Conference on Transparent Optical Networks (ICTON)*, Jul. 2005, p. Tu.B2.5.

[6] K. Ennser and S. Taccheo, "Investigation of transient response in cascaded gain-clamped erbium-doped fibre amplifiers," *IET Electronics Letters*, vol. 39, no. 24, pp. 1716–1717, Nov. 2003.

[7] C. Giles and E. Desurvire, "Modeling erbium-doped fiber amplifiers," *IEEE/OSA Journal of Lightwave Technology*, vol. 9, no. 2, pp. 271–283, Feb. 1991.

[8] L. Rapp, "Transient behavior of EDFA stages using pump power splitting or pump bypass technique," *IEEE/OSA Journal of Lightwave Technology*, vol. 25, no. 3, pp. 726–732, Mar. 2007.

[9] H. Nakaji and M. Shigematsu, “Wavelength dependence of dynamic gain fluctuation in a high-speed automatic gain controlled erbium-doped fiber amplifier,” *IEEE Photonics Technology Letters*, vol. 15, no. 2, pp. 203–205, Feb. 2003.

[10] D. Kovsh, S. Abbott, E. Golovchenko, and A. Pilipetskii, “Gain reshaping caused by spectral hole burning in long EDFA-based transmission links,” in *Proc. Optical Fiber Communication Conference (OFC)*, Mar. 2006, p. OTuK7.

[11] M. Bolshtyansky, “Spectral hole burning in erbium-doped fiber amplifiers,” *IEEE/OSA Journal of Lightwave Technology*, vol. 21, no. 4, pp. 1032–1038, Apr. 2003.

[12] J. Sulhoff, A. Srivastava, C. Wolf, Y. Sun, and J. Zyskind, “Spectral hole burning in erbium-doped silica and fluoride fibers,” *IEEE Photonics Technology Letters*, vol. 9, no. 12, pp. 1578–1579, Dec. 1997.

[13] M. Bolshtyansky, N. King, and G. Cowle, “Dynamic behavior of spectral hole burning in EDFA,” in *Proc. Optical Amplifiers and Their Applications (OAA)*, Jun. 2006, p. OTuB2.

[14] M. Bolshtyansky, N. King, and G. Cowle, “Dynamic behavior of spectral hole burning in EDFA with 980 nm pumping,” in *Proc. Optical Fiber Communication Conference (OFC)*, Mar. 2007, p. OMN2.

[15] L. Rapp, “Effect of spectral hole burning on the feedforward control of erbium-doped fiber amplifiers,” in *Proc. Optical Fiber Communication Conference (OFC)*, Mar. 2010, p. OThI5.

[16] M. Bolshtyansky and G. Cowle, “Spectral hole burning compensation in Raman/EDF hybrid amplifier,” in *Proc. Optical Fiber Communication Conference (OFC)*, Feb. 2008, p. JWA15.

[17] M. Yadlowsky, “Pump wavelength dependent spectral hole burning in EDFAs,” *IEEE/OSA Journal of Lightwave Technology*, vol. 17, no. 9, pp. 1643–1648, Sep. 1999.

[18] M. Bolshtyansky, N. King, and G. Cowle, “Characterization of site dependent pumping in EDFA,” in *Proc. Optical Amplifiers and Their Applications (OAA)*, Aug. 2005, p. WB5.

[19] P. Kean, S. Wilson, and M. Healy, “Pump induced inhomogeneity of gain spectra in conventional and extended-band EDFAs,” in *Proc. Optical Fiber Communication Conference (OFC)*, Feb. 1999, pp. 978–980.

[20] E. Desurvire, J. Sulhoff, J. Zyskind, and J. Simpson, “Study of spectral dependence of gain saturation and effect of inhomogeneous broadening in erbium-doped aluminosilicate

fiber amplifiers," *IEEE Photonics Technology Letters*, vol. 2, no. 9, pp. 653–655, Sep. 1990.

[21] W. Lee, B. Min, S. Ahn, and N. Park, "Simulation for the effect of cascaded gain-temperature dependence on 40 channel - 50 EDFA WDM link under temperature fluctuations," in *Proc. Lasers and Electro-Optics (CLEO)*, Aug. 1999, pp. 646–647.

[22] J. Lee, W. Lee, and N. Park, "Comparative study on temperature-dependent multichannel gain and noise figure distortion for 1.48- and 0.98-μm pumped EDFAs," *IEEE Photonics Technology Letters*, vol. 10, no. 12, pp. 1721–1723, Dec. 1998.

[23] M. Yamada and M. Shimizu, "Temperature dependence of signal gain in Er3+ -doped optical fiber amplifiers," *IEEE Journal of Quantum Electronics*, vol. 28, no. 3, pp. 640 – 649, Mar. 1992.

[24] F. Flood, "Comparison of temperature dependence in C-band and L-band EDFAs," *IEEE/OSA Journal of Lightwave Technology*, vol. 19, no. 4, pp. 527–535, Apr. 2001.

[25] M. Nishihara, Y. Sugaya, and E. Ishikawa, "Impact of spectral hole burning in multi-channel amplification of EDFA," in *Proc. Optical Fiber Communication Conference (OFC)*, Feb. 2004, pp. 4–6.

[26] E. Desurvire, *Erbium-doped fiber amplifiers: principles and applications.* Wiley, 1994.

[27] R. Muro and P. Kean, "Dependence of L-band amplifier efficiency on pump wavelength and amplifier design," in *Proc. Optical Fiber Communication Conference (OFC)*, Mar. 2000, pp. 120–122.

Chapter 6

Conclusions and Future Work

In this thesis, we analyzed the steady–state regime and the dynamic response of optical fiber amplifiers in the context of transparent and dynamical optical networks.

In this chapter, we overview the developed work, and summarize the main conclusions of this thesis. Finally, in Section 6.2 some topics for future studies are presented.

6.1 Conclusions

Chapter 2 introduces the fundamentals regarding Raman fiber amplifiers (RFAs) and erbium–doped fiber amplifiers (EDFAs), which were used in this work. The state of the art, configurations, and use cases for RFAs and EDFAs were highlighted and discussed in the beginning of the Chapter. Following, the physical principle of RFA was introduced, as well as the propagation equations of signals, amplified spontaneous emission (ASE) noise and pumps in the amplifier. Furthermore, we presented and implemented the average power analysis (APA) for the steady–state and for the dynamic regime. We experimentally validated the numerical models in the steady–state and in the dynamic regimes and a good accuracy was obtained for both. Regarding the EDFA, we presented the physical principle of two– and three–levels system amplification. Moreover, the inhomogeneous gain broadening, which manifests as the spectral hole burning (SHB) and site dependent pumping (SDP) effects was discussed. Following, we derived and implemented the model when considering inhomogeneous broadening of the amplifier gain for the two- and three–level EDFA. Using an experimental setup specifically designed to isolate and assess the SHB and SDP behaviors, we were able to validate, with good accuracy, the model derived and implemented for the three–level amplifier. Also, the dependence of the dynamics of SHB and SDP on spectral allocation of input channels was investigated experimentally for three–level EDFAs. We concluded that, by selecting a pump wavelength centered at 974 nm instead of 980 nm, we can reduce the power excursions by 23 %, and that by increasing the channel spacing from 100 GHz to 150 GHz the power excursions decrease by more than 20 %.

The development and implementation of a simplified model to estimate the gain and ASE noise of a broadband counter–pumped RFA suitable for use with multiple pumps and with a large number of signals was described in Chapter 3. The proposed model was based on the customization of the undepleted pump model (UPM), with the introduction of two new parameters. These parameters were used to account for pump–to–pump interactions, and could be adjusted either based on the comparison with experimental data or detailed numerical simulations, weighted–by comparison (WBC) model, or based on analytical expressions, weighted–by analytic expression (WAE) model. The second method was simpler to implement, because it could be used without comparison with experimental or numerical simulations. When comparing the WAE with experimental measurements and detailed numerical simulations, we found that this model provides accurate results for a total input pump power up to 900 mW, a wavelength separation up to 60 nm between pumps, and a transmission distance up to 180 km. The proposed model showed an improved computational performance without losing significant accuracy for the most common pump configurations. In fact, it was verified that the model can be more than 70 times faster than the detailed numerical model, APA, introduced on Chapter 2. We used the proposed WAE model to estimate the OSNR of WDM signals at the transmission link with a counter–pumped RFA, when considering different fiber types, fiber lengths and input signals powers. The obtained results were compared with the results obtained from a reference numerical model. From the comparison between both, we verified that the On/Off gain was properly estimated. However, the accuracy of the ASE noise power estimation was not enough. To overcome this, an extra parameter α_{adj} was introduced to adjust the estimation of the ASE noise output power. With the introduction of this parameter, we verified that the proposed model estimates the OSNR of the WDM signals at the end of the transmission link with a good accuracy. Thus, the proposed simplified model can be implemented in planning tools, providing an accurate estimation of the OSNR, without increasing the computational requirements of the tool. Afterwards, in the end of Chapter 3, we presented an efficient algorithm to design RFAs on the fly with low computational requirements. In the proposed algorithm, instead of solving the propagation equations with a detailed numerical model, we used a simplified model, the WAE, allowing to obtain the results in a time efficient manner. We implemented a genetic algorithm (GA) to search for the quasi–optimum solution that minimizes the gain ripple. Results showed that the simplified model takes less time, below fifty times less that the APA model, to achieve an optimized solution with good accuracy.

An efficient counter–pumped RFA suitable for dynamic networks was proposed and validated in Chapter 4. This amplifier was based on the reflection of the unused pump power back into the amplifier fiber, called pump–reflecting RFA. We experimentally verified that the pump–reflecting RFA presents an increased On/Off gain, when compared to the conventional counter–pumped RFA of about 1 dB. However, we also observed experimentally that the transient response due to channels add/drop was higher for this configuration, an increase of more than 20 %, making this amplifier unsuitable for dynamic networks. In order to better understand the impact of reflecting the unused pump power on the amplifier behavior, several scenarios were investigated in the steady–state and in the dynamic regimes. Results showed that the impact of reflecting the pump power on the transient effect was higher in a co–pumped RFA with a fiber–Bragg grating (FBG) than in a counter–pumped RFA with a FBG. Also, the impact of reflecting the pump power in the transient response of the counter–pumped RFA with an FBG decreased with the increase of the input pump power and with increased fiber length. In order to mitigate and control the transient response of the amplifier, we implemented a pump–controlled gain–clamping mitigation technique. The technique was based on the monitorization of the reflected pump power and on the use of that information to adjust the input pump power, in order to control the power fluctuation of the surviving channel. A theoretical analysis showed that in the considered setup, the power fluctuations of the surviving channel were about 0.7 dB when transient response was not controlled. On the other hand, when transient control was applied, these fluctuations were maintained bellow 0.2 dB. As a proof of concept, we also performed an experimental implementation of this technique. Despite the low response time of the implemented setup as well as the low length of the dispersion compensating fiber (DCF), we were able to reduce the transient effect before it reached its higher value. With this control system we demonstrated that this new proposal was effective, allowing the development of an efficient low cost RFA suitable to dynamic optical networks.

The EDFA dynamic response due to SHB and SDP caused by the variation of spectral allocation of input signals was analyzed in Chapter 5. The dependency of the dynamic response of EDFA pumped around 1480 nm and 980 nm governed by SHB and SDP on pump wavelength, pump power, and temperature was investigated experimentally. Experimental results showed that the magnitude of gain variations with pumping at 980 nm was almost twice the value observed in the case of pumping in the 1480 nm range. In addition, the dependency of SHB and SDP dynamics on pump power was demonstrated, and we verified that the dynamics of SHB and SDP become faster at higher pump powers. Moreover, it was also observed that the magnitude of gain variations induced by SHB and SDP scales with gain compression, similarly to the depth of the spectral holes observed in steady–state experiments. Furthermore, we showed for the first time that the dynamic response for EDFAs pumped around 1480 nm range presented a dependence on pump wavelength. Regarding the dependency on temperature, it was shown that gain variations induced by SHB decreased with increasing temperature, independently of the number of involved energy levels of the erbium ions. Presented measurement results revealed that an EDFA pumped at 980 nm was more sensitive to temperature variations than an EDFA using only two energy levels for signal amplification. However, the relative change was smaller for the EDFA using a pump wavelength of 980 nm. For a temperature variation of ±10 °C, the relative change of the maximum gain deviations was equal to ±2.6 % and ±1.45 % for the two and three–level EDFA, respectively. Afterwards, we derived and presented a model that incorporates the SDP effect for the two–level system EDFA. The proposed model was based on a correlation matrix between the pump wavelength and the signals wavelengths, which took into account the dependency of the gain spectrum on pump wavelength. Experimental measurements of the surviving channel power excursion were done for several pump wavelengths, channel input powers and pump powers, configurations and number of signals considered. By comparing the simulations results with the experimental measurements, we confirmed that the proposed model describes the measured power excursions with good accuracy. Moreover, differences between simulation results and experimental data were reduced significantly when compared to simulations taking into account SHB only. Furthermore, it was shown that obtaining accurate results for various operating conditions requires taking the SDP effect into account, even if only two power levels of the erbium ions are involved. Further simulations were done to investigate the behavior of the SHB and SDP in an ideal gain controlled EDFA pumped at 980 nm. Preliminary results showed that, in a subband switch, commuting from the red subband to the blue subband causes higher deviations than changing from the blue subband to the red subband of the C–band. Also, in a drop scenario, the overshoots and undershoots of the surviving channel depended on the input channels spectral allocation and on the gain of the amplifier.

6.2 Future Work

From the work presented in this thesis and considering the related developments published recently in the literature, the following topics are suggested as future work:

- Development of simplified models to estimate the gain and ASE noise of EDFAs. Nowadays, the estimation of the gain deviations from the target gain in EDFAs is based on look–up tables. In principle, this estimation should be improved by developing a model that predicts the gain deviations from the targeted operating gain.

- Implementation of the mitigation technique proposed in Chapter 4 in a higher–order counter–pumped RFAs. By doing so it might be possible to improve the efficiency of the amplifier without compromising the dynamic response. As an extra feature, it might be possible to use the information retrieved from the reflecting pump power and use it as a fail safe mechanism. If the fiber is damaged or broken, the control mechanism detects the power variation and immediately turn off the pumps.

- Investigation of an improved physical description of the SHB and SDP effects. Despite the investigations performed, a physical meaning and a description of these effects are still unclear. Therefore, it would be interesting to study the SHB and the SDP effects from a physical point of view. An outcome of this study might be the derivation of the correlation matrix from theoretical results.

- Investigation of the impact of the SHB and SDP effects on the transmission link with Monte Carlo simulations. Using the models derived for the two and three–levels EDFA, it is possible to evaluate the impact of the SHB and SDP on the transmission link. The identification of the worst case scenario can be used to reduce the impact of those effects on the signal quality.

- Investigation of a mitigation technique for the SHB and SDP effects. Some literature already points out the fact that the impact of the SHB and SDP in the transmission link is important. For this reason, it is interesting to find and propose a solution to control and mitigate these effects.